# DEVELOPMENT OF NOVEL HEAT EXCHANGERS

# WITH HIGH THERMAL CONDUCTIVITY AND DEFORMABLE WALLS

A Thesis

by

JINHYEUN KIM

Submitted to the Office of Graduate and Professional Studies of
Texas A&M University
in partial fulfillment of the requirements for the degree of

MASTER OF SCIENCE

| | |
|---|---|
| Chair of Committee, | Mustafa Akbulut |
| Committee Members, | Sreeram Vaddiraju |
| | Terry S. Creasy |
| | Rodney Bowersox |
| Intercollegiate Faculty Chair, | Efstratios Pistikopoulos |

August 2017

Major Subject: Energy

# ABSTRACT

Heat exchangers prove its utmost importance in various fields ranging from heat recovery units to power plants and process industries. Considering the enormity of the total energy involved and used in all heat exchanger operations, enhancements in heat exchanger performance are increasingly needed to push the limits of the global energy efficiency to higher levels.

Four common problems that all heat exchangers suffer from one way or another - pressure drop, fouling, clogging, and corrosion - limit the reliability and performance of heat exchangers. This research involves the development of a micro heat exchanger with a new class of Thermal Interface Materials (TIMs). TIMs can address the problems of the conventional heat exchanger by acting as a thermally conductive deformable wall because these hybrid nanocomposites have a very high bulk thermal conductivity with relatively low elastic modulus.

The aim of this paper is to investigate the performances of the heat exchanger with deformable walls while putting particular emphasis on the change of pressure drop and the enhancement of 3heat transfer characteristics. This analysis was investigated via simulation tools, COMSOL 5.3 Multiphysics and ANSYS 18.0.

This study can contribute to the investigation of TIMs' potential as a promising material for microchannel heat exchanger and the comprehensive understanding of the interaction between fluid flow, deformable structure, and the heat transfer.

# ACKNOWLEDGEMENTS

I would like to thank my thesis advisor Professor Mustafa Akbulut of Texas A&M University, for his guidance and support throughout the course of this research. The door to Prof. Akbulut's office was always open whenever I ran into trouble or had a question about my research or writing. I am gratefully indebted to his very valuable comments on this thesis. Thanks also go to lab colleagues for their assistance with my research. Finally, thanks to my mother and father for their encouragement. A portion of this research was conducted with the advanced computing resources provided by Texas A&M High Performance Research Computing.

# CONTRIBUTORS AND FUNDING SOURCES

## CONTRIBUTORS

This work was supervised by a thesis committee consisting of Professor Mustafa Akbulut of the Department of Chemical Engineering, Professor Terry Creasy of the Department of Materials Science and Engineering, Professor Sreeram Vaddiraju of the Department of Chemical Engineering, and Professor Rodney Bowersox of the Department of Aerospace Engineering.

All work for the thesis was completed by the student, under the advisement of Professor Mustafa Akbulut of the Department of Chemical Engineering.

## FUNDING SOURCES

Graduate study was supported by a fellowship from Engineering Development Research Center (EDRC) of Seoul National University, and this work was made possible in part by the research grant by Professor Mustafa Akbulut

# NOMENCLATURE

| | |
|---|---|
| $A_c$ | Cross-sectional area, $m^2$ |
| Al | Aluminum |
| BLT | Bond line thickness |
| BNNS | Boron nitride nanosheets |
| Cu | Copper |
| $D_h$ | Hydraulic diameter, m |
| f | Friction factor |
| f-BNNS | Functionalized boron nitride nanosheets |
| GPa | Gigapascal |
| k | Overall heat transfer coefficient, $W/(m^2K)$ |
| K | Kelvin temperature |
| $\dot{m}$ | Mass flow rate, kg/s |
| NMP | N-methyl-2-pyrrolidone |
| NTU | Number of Transfer Unit |
| p | Pressure, Pa |
| P | Wetted perimeter, m |
| PCMs | Phase change materials |
| Q | Heat transfer rate, W |
| $Q_{loss}$ | Measurement error of Q, % |
| q | Heat flux, $W/m^2$ |
| R | Thermal resistance, $m^2K/W$ |
| $R_{bulk}$ | Bulk thermal resistance, $m^2K/W$ |
| $R_c$ | Contact resistance of TIM, $m^2K/W$ |
| Re | Reynolds number |
| $R_{TIM}$ | Thermal resistance of TIM, $m^2K/W$ |
| SMA | Shape Memory Alloy |
| TIM(s) | Thermal Interface Material(s) |

| | |
|---|---|
| TSC | (1S)-1-amino-2-(1H-indol-3-yl)ethanol |
| $\Delta T_{LMTD}$ | Log mean temperature difference |
| UA | Heat transfer performance |
| V | Volt |
| W | Watt |

*Subscripts*

| | |
|---|---|
| c | Cold |
| h | Hot |
| i | Inlet |
| o | Outlet |
| m | Mean |

*Greek symbols*

| | |
|---|---|
| Ø | Volume fraction of particles in TIMs |
| ε | Effectiveness |
| ω | Velocity, m/s |
| $\mu$ | Dynamic viscosity, $Ns/m^2$ |
| $\rho$ | Density, $kg/m^3$ |
| $\delta$ | Performance index, W/kPa |

TABLE OF CONTENTS

LIST OF FIGURES

Page

Page

Page

Page

Page

LIST OF TABLES

Page

# 1. INTRODUCTION

In the last few decades, microfluidic systems such as micro-coolers, micro-reactors, and micro heat exchangers have been developed at a tremendous pace for its convenient geometry for heating and cooling fluids. Microchannel has been identified as one of the most critical elements in microfluidic devices, to transport fluid within a micro-scale area. However, the high pressure drop along the microchannel remains as the essential problem in microfluidic devices.

Many researches have been focused on enhancing the performance of microchannel by introducing high-efficient materials and various flow geometries to microchannels. Although a significant improvement on heat transfer mechanism is made by suggesting more geometrically complex microchannels in a micro heat exchanger, most works still have the high-pressure drop problem, which significantly hinders the advancement in microfluidic systems.

In the meanwhile, Thermal Interface Materials (TIMs) have been developed to overcome inefficient heat dissipation problems. These TIMs have both the high thermal conductivity and the mechanically compliant properties, which are the essential parts to reduce pressure drop while transporting heat efficiently. Recently, a new class of TIMs is reported that has lowest thermal resistance with sufficiently low elastic modulus to date for a TIM with a typical bond line thickness of 30-50 μm (Yegin et al., 2017).

This work seeks to overcome heat exchanger problems – specifically the pressure drop problem in a micro heat exchanger – by introducing this new type of TIMs to a micro heat exchanger. Since TIM has excellent mechanically compliant characteristics as well as high thermal conductive properties, it may give a potential application about the pressure drop problem in a micro heat exchanger. This research incorporates state of the art TIMs into micro heat exchanger and investigates the pressure drop and heat transfer performance on various conditions to determine the effect of ‘deformable’ walls.

# 2. BACKGROUND

## 2.1 Micro Heat Exchangers

Micro heat exchanger is the core elements for diverse engineering process devices for the purpose of heat exchange, with structural dimensions of micron scale. Micro heat exchanger significantly enhances the heat transfer performance by increasing the amount of heat exchange per unit volume. With the aim of process intensification, the attention for micro heat exchanger has been continuously increasing.

When we classify the heat exchanger as 'micro', surface area density ($m^2/m^3$) is often used. Surface area density is the ratio of the heat exchange surface area to the useful volume for one fluid, and is also called as 'compactness'. It is stated (Shah, 1991) that a heat exchanger is classified as micro heat exchanger when the surface area density is above 10,000 ($m^2/m^3$).

In the last few decades, owing to the progress of fabricating and measuring precisions, most of the researches has been focused on heat transfer and the fluid flow characteristics of individual microchannels, not the whole combined units (Fan & Luo, 2008). Therefore, the classification of heat exchanger based on the channel dimension is worth discussing, and the classification proposed is introduced in Table 1 (Mehendale et al, 2000).

**Table 1.** Channel classification based on channel dimension

| Definition | The range of channel dimension |
|---|---|
| **Micro-scale** | 1 – 100 μm |
| **Meso-scale** | 100 μm – 1 mm |
| **Macro-scale** | 1 – 6 mm |
| **Conventional scale** | > 6 mm |

The channel dimension and the surface area density is interrelated, and it is noted (Mehendale, 2000) that the characteristic channel dimensions of 100 μm is achieves the

surface area density over 10,000 ($m^2/m^3$). The division line between the micro and the meso-scale is arbitrary, and this paper deals with the heat exchanger with the scale of 1 – 1000 μm for convenience.

### 2.2 Advantages and Limitations of Micro Heat Exchangers

The main advantage of the micro heat exchanger is that enormous volumetric heat transfer can be achieved with a micro heat exchanger, because the heat exchange surface per unit volume increases. Micro heat exchanger proves its performance mainly with heat transfer characteristics, and the advantages of it can be listed as follows (Fan & Luo, 2008).

1. Compactness: High surface area density substantially decreases the heat exchanger volume needed. The cost and the space needed to install and construct heat exchanger is significantly decreased. When toxic, explosive, or expensive fluids are considered, small fluid holdup also be a great advantage of micro heat exchangers.

2. Effectiveness: Large overall heat transfer coefficient can be achieved with micro heat exchanger, which makes the heat transfer performance more effective. Recently, with the development of micro-fabricating technologies, more effective design configuration of micro heat exchanger can be achieved to reduce the major problems of micro heat exchangers.

3. Dynamic: Better temperature control between fluid flows is possible for micro heat exchanger because of its quick response time. In microchannels, the temperature change of one fluid can induce the distinct response of other fluid, and enable "two temperature-change waves". However, in conventional channels, two responses can be blurred into one.

With these advantages, exact process control is possible for a micro heat exchanger, which can lead to better outputs or yields while consuming the fewer resources. However, micro heat exchanger faces major bottlenecks that hinder the progress and industrial application of it.

1. High pressure drop and a small temperature jump: Excellent thermal performance is achieved, however, high pressure drop and a small temperature jump due

to the extremely short residence time is the limitation. Karlsruhe Research Center reported (Bier, Keller, Linder, Seidel, & Schubert, 1990), (Bier et al., 1993) typical data of micro heat exchanger for industrial applications, and it shows that high pressure drop (>4bar) and a weak temperature jump (≈10℃) with short residence time (≈2ms). High pressure drop triggers high mechanical power needed as well as the rigorous demands for concomitant devices such as pumping devices or connections.

2. Fouling, clogging, and corrosion: Fine channels of the micro heat exchanger is very sensitive to fouling, clogging, corrosion. Eroded channel walls due to the chemical etching and physical wearing increase the roughness, which is the major problem inducing high pressure drop especially in microchannels. Moreover, in general, maintenance and the mechanical cleaning is not possible. Therefore, very clean fluids can only be employed within the microchannels (Fan & Luo, 2008).

This research is conducted mainly to solve the high pressure drop problem in micro heat exchangers, but also aims to solve the fouling, clogging, and corrosion problem by preventing the erosion of the wall.

### 2.3 Efforts to Overcome the Major Bottlenecks of Micro Heat Exchangers

The four major problems of a heat exchanger are pressure drop, corrosion, clogging, and fouling. There are thousands of papers related to the enhancement of the efficiency and the reliability of a heat exchanger, and the enhancement techniques that incorporate high efficient materials into a heat exchanger has been actively studied. One of the most promising materials used in a heat exchanger is ceramic. Ceramic materials have high-temperature capabilities and corrosion resistance, which guarantee the advanced heat transfer performance. The summary of heat exchanger designs and materials are described in Table 2. In Table 2, effectiveness refers to the ratio of ‘Actual heat transfer rate’ to ‘Maximum possible heat transfer rate’.

**Table 2.** Comparison of calculated performance for heat exchanger designs and materials. Reprinted from "High-efficiency, ceramic microchannel heat exchangers," by Charles Lewinsohn, *American Ceramic Society Bulletin, 94, No. 5*, 26-31. Copyright 2015 American Ceramic Society.

| Technology | Status | Upper use temperature(℃) | Effectiveness | Lifetime(years) |
|---|---|---|---|---|
| **Superalloy, conventional designs** | Existing | 700 | 0.6-0.9 | 5 |
| **Metallic microchannel** | Existing/emerging | 700 | 0.8-0.9 | 5 |
| **Ceramic microchannel** | Target | 800 - 1300 | >0.9 | 5 to 10 |

In addition to incorporate diverse material to heat exchanger, diverse techniques have been employed to enhance the heat transfer performance. Three methods are usually thought as typical to enhance convective heat transfer: 1) Decreasing the thermal boundary layer thickness, 2) Increasing the interruption of the flow, 3) Increasing the velocity gradient near a heat transfer surface (Kandlikar, Joshi, & Tian, 2003) (Steinke & Kandlikar, 2004). Previous works of heat transfer enhancement techniques are the manipulation of these three methods.

Heat exchanger performance based on three micro heat exchanger designs (long offset strip, short offset strip, and chevron flow path) is investigated, and the research shows that the chevron channel heat exchanger demonstrates the lowest thermal resistance, while its pressure drop is five times higher than other two heat exchangers (Yang, Yeh, Liu, & Yang, 2007). Likewise, more complex and detailed geometric features can increase the heat transfer, but they significantly increase the pressure drop. If we can enhance heat transfer performance without jumping the pressure drop, progressive advancement can be made in the area of microfluidic devices.

Characteristics of heat transfer surface are one of the main factors that affect the heat transfer. Increasing the surface roughness can enhance heat transfer by reducing the thermal boundary layer thickness and stirring up the flow enough to transit into turbulent flow. Since the roughness ratio can be very large in a microchannel, active works have been conducted to this factor with the information on the microfluidic physics. The effect of surface roughness in a mini channel flow with a diameter between 3 mm and 200 μm

is conducted (Tao, He, Wang, Qu, & Song, 2002). They observed that the effective roughness ε/D ratio plays more significant role in smaller diameter channel than in a conventional channel. One of the interesting works related to this roughness structure to increase heat transfer is Shape Memory Alloy (SMA). The Nickel Titanium, which is one of the SMA, is employed for an insert of a heat exchanger (Champagne & Bergles, 2001). In their work, the insert expands as the change in temperature increased, and finally, enhance the heat transfer.

Flow disruption technique is the most interesting factor that enhances heat transfer. In a heat exchanger, flow interruptions increase mixing of the fluid and cause the flow transition, which leads the increased heat transfer. In conventional heat exchangers, flow inserts, flow disruptions along the surface and offset strip fins are a typical method to provoke flow disruption (Steinke & Kandlikar, 2004). Although it is hard to use flow inserts in a microchannel heat exchangers, carefully designed flow geometry trigger the flow disruption. Flow obstacles stimulate flow interruptions as well.

Curved channel and the entrance region of channels can also enhance heat transfer (Sturgis & Mudawar, 1999) (Gui & Scaringe, 1995). Sudden expansions and contractions produce entrance effect or re-entrant obstructions and bring about a perpetual state of development in a flow, which leads to the increased heat transfer. In this case, optimum results in a heat exchanger performance can be achieved by carefully designing a geometric structure that provides the maximum entrance effect with the minimum pressure drop (Steinke & Kandlikar, 2004).

Secondary flows are also proved to be one of the effective ways to enhance heat transfer. Using offset strip fins, chevron plates, and further detailed design of microchannel would induce secondary flows. Also, the flow-induced vibration would cause the enhanced heat transfer.

### 2.4 Microscale Heat Transfer

In conventional heat exchangers, heat transfer is governed by the thermal conductivity of the transfer layer. In microchannel heat exchangers, however, flow rates

and geometries - not thermal conductivity of the heat transfer layer - govern resistance. (Lewinsohn, 2015). The geometry features of microchannels are the first factor that significantly affects the fluid flow and heat transfer characteristics in microchannels. Diverse experimental results were obtained for microchannels according to a trapezoidal, rectangular, and hexagonal cross-section (Morini, 2004). In addition to the geometric consideration, it is crucial to study the variation of the flow structure in a heat exchanger and analyze the performance of a heat exchanger according to the flow regime. Fluid flow and forced convection heat transfer were investigated in microchannel heat exchanger (Jiang, Fan, Si, & Ren, 2001), and they found that the transition from laminar to turbulent occurs around Re ≈ 600. For laminar flow, the friction factor depends on the material of the microchannel walls, on the test fluid (polar fluid or not), and on the relative roughness of the walls (Morini, 2004).

### 2.5 Thermal Interface Materials (TIMs)

When two solid surfaces are in contact, the actual contact between the two solids is hindered by asperities on each of the surfaces, as shown in Figure 1 (a). Consequently, the heat transfer across an interface occurs in two ways: 1. Solid-to-solid conduction in the area of actual contact, 2. Conduction through the fluid in the non-contact area of the interface (R. Prasher, 2006).

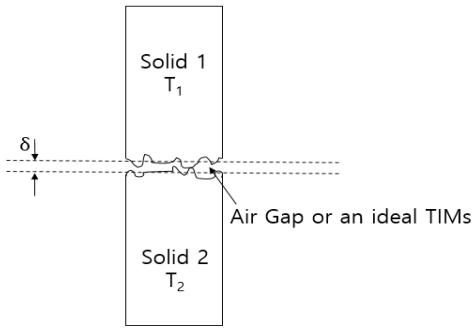


**Figure 1 (a).** Real area of contact and the apparent area of contact for ideal TIMs

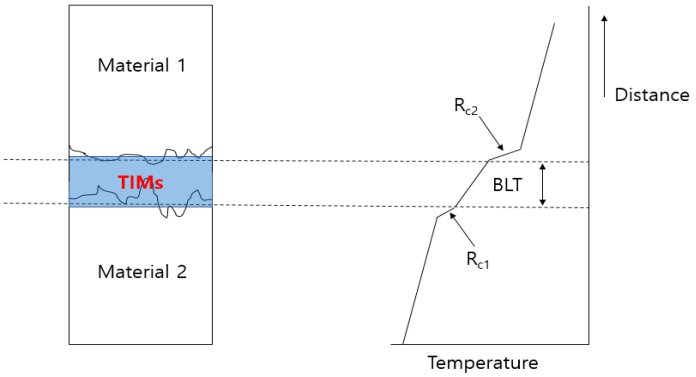


**Figure 1 (b).** Real area of contact and the apparent area of contact for real TIMs, and the schematic showing the thermal resistance

From Figure 1 (b), the total thermal resistance $R_{TIM}$ of real TIM is (R. S. Prasher, 2001):

$$R_{TIMs} = \frac{BLT}{k_{TIM}} + R_{c1} + R_{c2} \qquad eq.(1)$$

Here, $R_{c1}$ and $R_{c2}$ represent the contact resistances of the TIMs with the joined materials 1 and 2, respectively. TIMs are developed to reduce $R_{TIMs}$. That is, highly conducting material – Thermal Interface Materials (TIMs) – fill this interfacial gap between the asperities to increase heat flow through the interfaces as shown in Figure 1 (b). However, Figure 1 (b) indicates that real TIMs has a limit to fill the gap or wet the surface completely (R. Prasher, 2006). In general, an ideal TIMs should have both the high thermal conductivity and the mechanically compliant properties for guaranteeing them to transport heat across an interface efficiently and to be reliable.

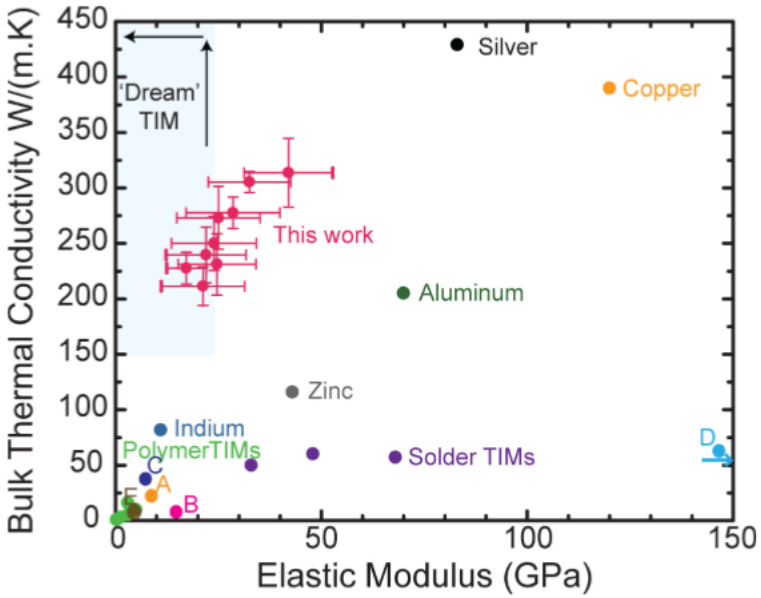


**Figure 2.** Comparison of bulk thermal conductivity versus elastic modulus values for various types of TIMs, engineering thermal management materials, and the new class of TIMs. Reprinted with permission from "Metal-Organic-Inorganic Nanocomposite Thermal Interface Materials with Ultralow Thermal Resistances," by Cengiz Yegin, Nirup Nagabandi, Xuhui Feng, Charles King, Massimo Catalano, Jun Kyun Oh, Ansam J. Talib, Ethan A. Scholar, Stanislav V. Verkhoturov, Tahir Cagin, Alexei V. Sokolov, Moon J. Kim, Kaiser Matin, Sreekant Narumanchi, and Mustafa Akbulut, *ACS Applied Materials & Interfaces* 2017 *9*(11), 10120-10127. Copyright 2017 American Chemical Society.

As shown in Figure 2, the newly developed TIMs has very high bulk thermal conductivity with relatively low elastic modulus. This performance means that this new TIM can not only efficiently transport heat between the interfaces but also has excellent reliability. This newly developed hybrid nanocomposite demonstrates high thermal conductivity values on the order of 211 to 277 W/(m·K)), which is exceptionally high with their relatively low elastic modulus ranging from 21.2 to 28.5 GPa. Thanks to this cooperative combination of TIMs' highly thermally conductive and mechanically compliant characteristics, these hybrid nanocomposites achieve the lowest measured total thermal resistivity (0.38 to 0.56 $mm^2 \cdot K/W$) to date for a TIMs with a typical BLT of 30-50 μm (Yegin et al., 2017). In the eq. (1), the bulk thermal resistance of the TIMs is given by:

$$R_{bulk} = \frac{BLT}{k_{TIM}} \qquad eq.(2)$$

$R_{bulk}$ depends on particle volume fraction (Ø). Several experiments were conducted on the thermal resistance for various parameters involving Ø, filler shape, and the applied pressure (R. S. Prasher, Shipley, Prstic, Koning, & Wang, 2003), and they concluded that there is an optimal volume fraction that minimizes the thermal resistance. Therefore, the synthesis of TIMs will be an important factor in determining the heat transfer performance, and the further investigation of the relationship between the various parameters and the thermal resistance should be conducted. The geometry feature of electrodeposited TIMs can be observed via SEM micrographs as shown in Figure 3.

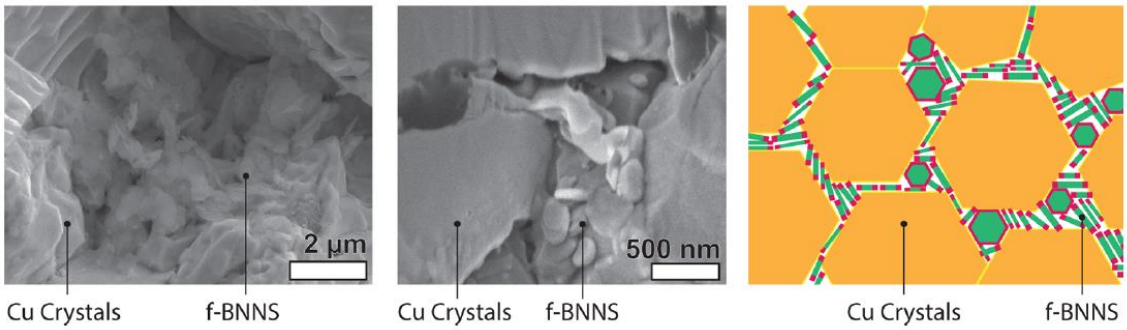


**Figure 3.** SEM micrographs and the schematic illustration showing the distribution of f-BNNS across the copper matrix. Reprinted with permission from "Metal-Organic-Inorganic Nanocomposite Thermal Interface Materials with Ultralow Thermal Resistances," by Cengiz Yegin, Nirup Nagabandi, Xuhui Feng, Charles King, Massimo Catalano, Jun Kyun Oh, Ansam J. Talib, Ethan A. Scholar, Stanislav V. Verkhoturov, Tahir Cagin, Alexei V. Sokolov, Moon J. Kim, Kaiser Matin, Sreekant Narumanchi, and Mustafa Akbulut, *ACS Applied Materials & Interfaces* 2017 *9*(11), 10120-10127. Copyright 2017 American Chemical Society.

A new class of TIMs is developed through the covalent integration of BNNS, a copper matrix, and a soft organic linkers or ligand (TSC) as shown in Figure 4, via chemisorption coupled electrodeposition approach (Yegin et al., 2017). The BNNS and

Cu are linked through ligand because BNNS is ceramic while Cu is metallic, which means that they are not mixable.

First, BNNS is linked to the ligand (TSC) to make f-BNNS through the chemisorption process with the solvent (NMP) at 170 °C for 30 hours, followed by the extraction process by dialysis and centrifuge. The chemical reaction schemes are illustrated in Figure 5.

Then, f-BNNS is mixed with the solution of $H_2O$, $CuSO_4 \cdot 5H_2O$, $H_2SO_4$, and $CuCl_2$, and sonicated for 30 minutes. After that, the new TIMs is developed through the chemisorption coupled electrodeposition process with a copper matrix. The chemisorption coupled electrodeposition approach is described below in Figure 6.

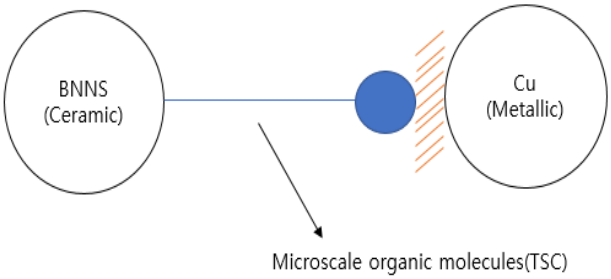


**Figure 4.** Schematic illustration showing the covalent integration of BNNS and Cu through TSC

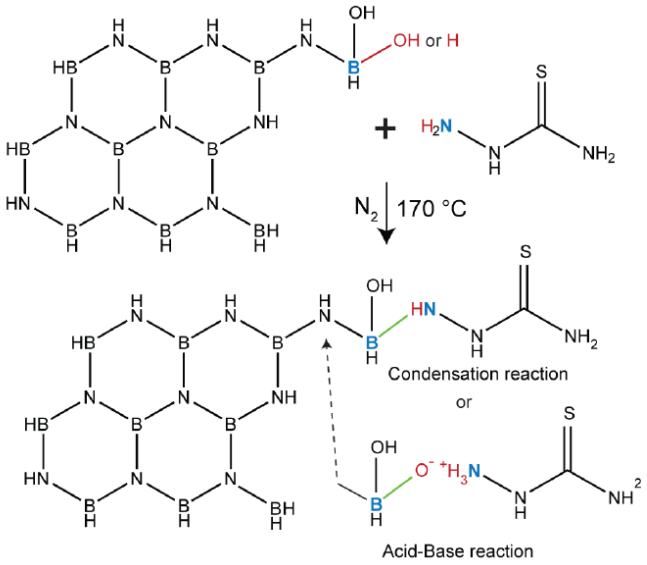


**Figure 5.** Proposed reaction schemes before and after the functionalization reaction. Reprinted with permission from "Metal-Organic-Inorganic Nanocomposite Thermal Interface Materials with Ultralow Thermal Resistances," by Cengiz Yegin, Nirup Nagabandi, Xuhui Feng, Charles King, Massimo Catalano, Jun Kyun Oh, Ansam J. Talib, Ethan A. Scholar, Stanislav V. Verkhoturov, Tahir Cagin, Alexei V. Sokolov, Moon J. Kim, Kaiser Matin, Sreekant Narumanchi, and Mustafa Akbulut, *ACS Applied Materials & Interfaces* 2017 *9*(11), 10120-10127. Copyright 2017 American Chemical Society.

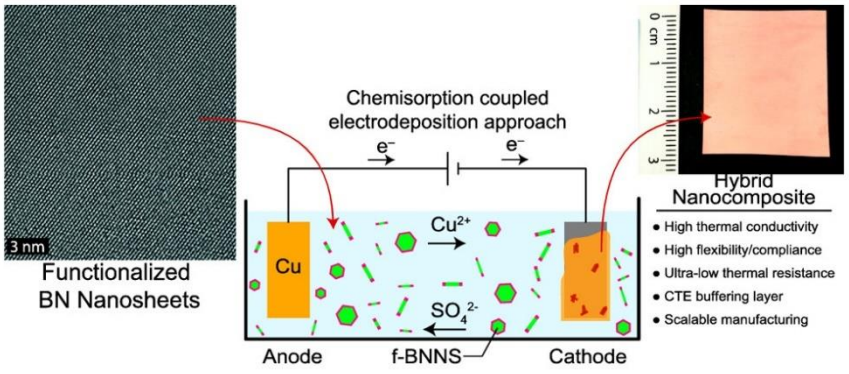


**Figure 6.** Chemisorption coupled electrodeposition process. Reprinted with permission from "Metal-Organic-Inorganic Nanocomposite Thermal Interface Materials with Ultralow Thermal Resistances," by Cengiz Yegin, Nirup Nagabandi, Xuhui Feng, Charles King, Massimo Catalano, Jun Kyun Oh, Ansam J. Talib, Ethan A. Scholar, Stanislav V. Verkhoturov, Tahir Cagin, Alexei V. Sokolov, Moon J. Kim, Kaiser Matin, Sreekant Narumanchi, and Mustafa Akbulut, *ACS Applied Materials & Interfaces* 2017 *9*(11), 10120-10127. Copyright 2017 American Chemical Society.

## 2.6 Arbitrary Lagrangian-Eulerian Method and Fluid-Structure Interaction

Arbitrary Lagrangian-Eulerian (ALE) method is a numerical technique to obtain solutions for time-dependent multidimensional fluid dynamics problems. ALE technique considers the finite difference mesh with vertices that involve the fluid movement (Lagrangian), be fixed (Eulerian), or the combination of these two conditions in any other prescribed manner. Navier-Stokes equations present a solution with the equation that is both Lagrangian and Eulerian, and the ALE technique can be applied to solve these equations numerically(Hirt, Amsden, & Cook, 1974). The differential equations for mass balance, momentum balance, and the energy balance is used:

$$\frac{\partial \rho}{\partial t} + \nabla \cdot \rho u = 0 \qquad eq.(3)$$

$$\frac{\partial \rho u}{\partial t} + \nabla \cdot \rho u u = -\nabla p + \rho g \qquad eq.(4)$$

$$\frac{\partial \rho E}{\partial t} + \nabla \cdot \rho E u = -\nabla \cdot p u + \rho g \cdot u \qquad eq.(5)$$

Where E = $\frac{1}{2} u \cdot u + I$, $g$ is a body acceleration, p is the fluid pressure, and $I$ is the specific internal energy of the material discussed. ALE method involves three steps and the iteration process of three steps.

Initialization: Mesh volumes, mesh total energies, and the masses assigned to vertices are calculated based on given modeling.

Step 1: Velocities are updated in time using pressure gradients and body forces. Pressure gradients and body forces are computed from the pressures and mesh coordinates that can be obtained at the previous step.

Step 2-1: Moved vertices with new velocities update the densities and energies, and these updated densities and energies recalculate pressures by iteration.

Step 2-2: Cell energies is adjusted for the pressure work terms, and complete the Lagrangian portion of a cycle.
Step 3: Reasonable mesh structure is obtained by controlling the mesh vertices on the fluid.

Fluid flow deforms the structures and the deformed structures affect the fluid flow. The interactive relationship between continuously deforming geometry and the fluid flows is solved by ALE technique. Freely moving deformed mesh on the fluid domain is the place that Navier-Stokes equations are solved, and the Smoothing method is used to consider the deformation of this mesh relative to the initial shape of the domain.

**2.7 Two-way Boundary Coupling Method**

Two-way boundary coupling is the method that COMSOL 5.3 Multiphysics use to consider the interaction between the fluid and the solid. In this paper, brief explanation of two-way boundary coupling is introduced (Elabbasi & Segui, 2014).

Step 1. Set up FSI equations:
A. Fluid flow

$$\rho\frac{\partial u_{fluid}}{\partial t} + \rho(u_{fluid}\cdot\nabla)u_{fluid}$$
$$= \nabla\cdot\left[-pI + \mu\left(\nabla u_{fluid} + (\nabla u_{fluid})^{T}\right) - \frac{2}{3}\mu(\nabla\cdot u_{fluid})I\right] + F$$

$$\rho\nabla\cdot u_{fluid} = 0$$

B. Solid deformation

$$\rho\frac{\partial^2 u_{solid}}{\partial t^2} - \nabla\cdot\sigma = Fv$$

C. Moving mesh

$$x = x(X, Y, t)$$

$$y = y(X, Y, t)$$

Step 2. Apply the conditions at the Fluid-structure interaction boundary

A. Apply fluid forces on fluid-solid boundary

$$\Gamma = \left[-pI + \mu\left(\nabla u_{fluid} + \left(\nabla u_{fluid}\right)^{T}\right) - \frac{2}{3}\mu\left(\nabla \cdot u_{fluid}\right)I\right]$$

$$\sigma \cdot n = \Gamma \cdot n$$

B. Impose fluid velocities based on velocity of solid on boundary

$$u_{fluid} = u_{wall}$$

$$u_{wall} = \frac{\partial u_{solid}}{\partial t}$$

Step 3. Solve system of equations

Step 4. Iterate until solution converges

With the iteration, the solution is obtained for fluid flow and the solid deformation. Brief illustration for two-way boundary coupling iteration method is shown in Figure 7.

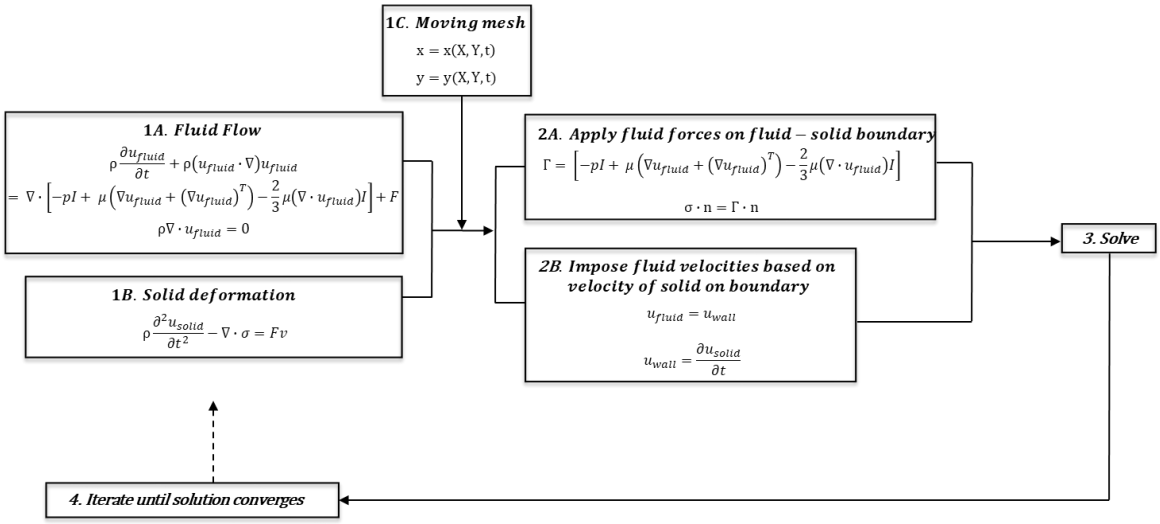


**Figure 7.** Two-way boundary coupling method

# 3. DIRECTIONS

This research focuses on solving the high pressure drop problem in a micro heat exchanger. We know from Table 2 that the ceramic is the target material that researchers try to incorporate into the heat exchanger, and the metal is the widely used material for heat exchanger these days. This research uses the TIMs, the metal-organic-inorganic(Ceramic) nanocomposite material, to overcome the major problems of a micro heat exchanger. Since TIMs is the synthesized material with the combination of metal and ceramic, the author expects that the TIMs heat exchanger may have the advantages of ceramic and metal (e.g., effectiveness, lifetime). Furthermore, by applying the TIMs coating with electrodeposition method onto the inner wall of the microchannel, TIMs coating can be acted as the deformable wall. The deformable wall can reduce the pressure drop by reducing the shear stress between the fluid and the wall.

First, the experiment is conducted to determine TIMs' viability of applying it to the microchannel. After, the roughness generated by the electrodeposition and the relatively fragile perspective of TIMs lead the author to consider the second coating process (Electroless Nickel Boron Nitride coating (EN-BN coating)) on the TIMs coating. The second coating (EN-BN coating) upon the first coating (TIMs coating) can improve wear resistance and impart lubricity properties. The author expects that second coating upon deformable coating mitigate the fouling, clogging, and corrosion problem by preventing the erosion of the wall.

After determining the industrial viability of applying TIMs coating on the microchannel, this paper shows simulation results of the deformable wall to determine the performance of the deformable coating in microchannel, with particular emphasis on pressure drop and heat transfer.

# 4. METHODOLOGY

## 4.1 Electrodeposit TIMs in Heat Exchanger

Electrodeposition should be conducted on the inside of the microchannel to make a novel heat exchanger with TIMs coating. Electrodeposition on a circular channel with diameter 1cm and length 10cm is conducted via experiment to see the viability of electrodeposition in the 'micro' channel. It is crucial to uniformly deposit TIMs, as irregular shape contributes to large pressure drop. The electrodeposition is conducted on a conventional channel with a diameter of 10mm. Here, Al is used for the substrate of heat exchangers, with a thermal conductivity of 237 W/(m·K), the density of 2,700 kg/$m^3$, and specific heat at constant pressure of 904 J/(kg·K). TIMs is electrodeposited in this channel. The coating thickness of 30-50 μm is preferred for high heat transfer because TIMs achieves the lowest measured total thermal resistivity (0.38 to 0.56 $mm^{2}$·K/W) with a typical BLT of 30-50 μm (Yegin et al., 2017).

The primary consideration to achieve uniform deposited feature is the current distribution. The uniform feature can be achieved by applying uniform current distribution. Uniform current distribution is obtained by using a copper rod (fixed it by passing the center of the aluminum hole with pipe fittings), instead of using a copper plate during electrodeposition. Besides, f-BNNS solutions are not mixed well, so the solutions are mixed continuously by using the peristaltic pump and the stir bar as shown in Figure 8.

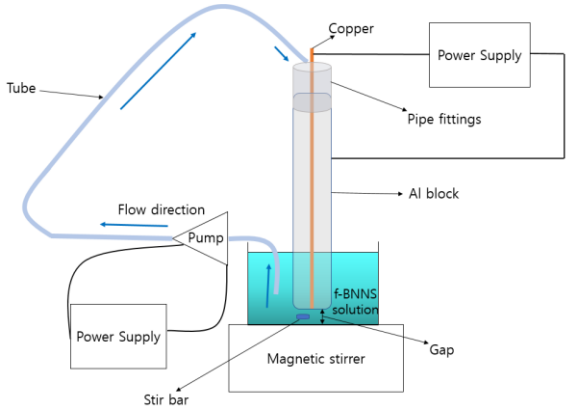


**Figure 8.** Experimental setup for electrodeposition of TIMs

In Figure 8, the gap between the Al block and the bottom of the solution tank is necessary to prevent the lump from hindering the flow. The Al block is set up vertically because high flow rate that is fit for the current peristaltic pump (Specification: DC 12V) makes the electrodeposition with low current - that is required for uniform electrodeposition - difficult. During the experiment, current interruption cycles are also used to achieve the uniform deposited feature (Dini et al, 2010). TIMs is electrodeposited while interrupting the current for 1 second at every 10 seconds. Figure 9 shows the deposited feature of TIMs when electrodeposition is applied on a flat Aluminum plate, and Figure 10 shows the electrodeposited feature of TIMs when electrodeposition is applied on the Aluminum channel with a diameter of 10mm.

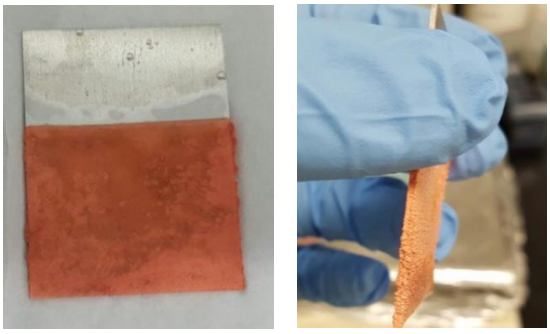

**Figure 9.** Deposited feature of TIMs on flat Aluminum plate

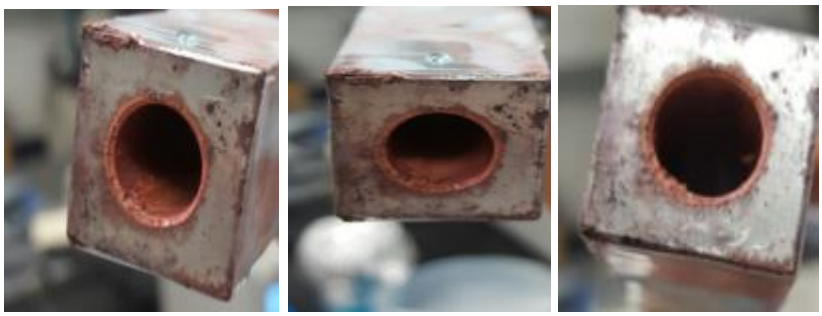

**Figure 10.** Deposited feature of TIMs on circular channel

From the experiment, electrodeposition can be conducted with low roughness. With much smaller diameter, the electrodeposition can be conducted:

1. Submerge the microchannel into the solution and forced the flow through the channel.
2. Epoxy glue can be applied to prevent electrodeposition for the other part.

### 4.2 Coating with Boron Nitride Electroless Plating Kit

Electrodeposited TIMs has roughness and fragile when high pressure or velocity is induced. To solve this problem, Electroless Nickel Boron Nitride (EN-BN) coating is considered onto the deposited TIMs. EN-BN coating is selected for the advantages discussed below.

1. Uniform thickness
2. Wear resistance
3. Abrasion resistant
4. High lubricity coating
5. Extremely slick thickness around 5um
6. High corrosion resistance.
7. Low coefficient of friction numbers under higher loads, which gives a way to solve the roughness problem of TIMs coating (Ploof, 2008).

Electroplating kit was purchased from CASWELL plating company, and the performance of second coating is verified to solve the limitations of TIMs coating – Fragile and roughness – by the author.

### 4.3 Simulation

COMSOL 5.3 Multiphysics and the ANSYS 18.0 is used for simulation with fully coupled stationary and time-dependent solver. Fluid-structure interaction module is employed to consider the interaction between the fluid and the wall in COMSOL. For ANSYS, the System Coupling Method for Fluid Transient and the Structure Transient is used. The model used in each simulation tool is described in Table 3 and Table 4. Intel CORE i7 vPro PC is used for the simulation.

**Table 3.** Simulation tools for pressure drop observation

| **Objective: Pressure drop observation** | | |
|---|---|---|
| **Consideration: Interaction of fluid and deformable coating** | | |
| **Simulation tool** | COMSOL 5.3 Multiphysics | Fluid-structure interaction (fsi) module |
| | ANSYS 18.0 | Fluent Flow + Transient Structural (System Coupling) |

**Table 4.** Simulation tools for heat transfer observation

| **Objective: Heat transfer observation** | | |
|---|---|---|
| **Consideration: Interaction of fluid and deformable coating** | | |
| **Simulation tool** | COMSOL 5.3 Multiphysics | Fluid-structure interaction (fsi) module + Conjugated heat transfer module |

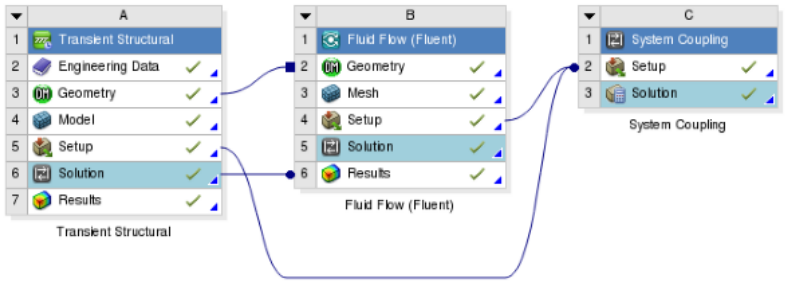


**Figure 11.** ANSYS 18.0 setup for pressure drop observation

Figure 11 shows the coupling method that considers the interaction between fluid flow and the deformable structure. However, it is currently not possible to couple more than two components with ANSYS. Therefore, three coupled observation (heat transfer + fluid characteristics + wall deformation) is investigated with COMSOL 5.3 Multiphysics.

# 5. RESULTS AND DISCUSSION

## 5.1 Setup

### 5.1.1 Geometric Setup

One circular microchannel is introduced with a 2D asymmetric model to observe the displacement of the deformable wall. 2D asymmetric model is used for simplicity and to reduce the computed time as shown in Figure 12. The computed model can be shown both in 2D and 3D, as shown in Figure 13. The substrate channel where the coating is applied (e.g., for Aluminum heat exchanger, substrate channel is Aluminum) is omitted for the simplicity.

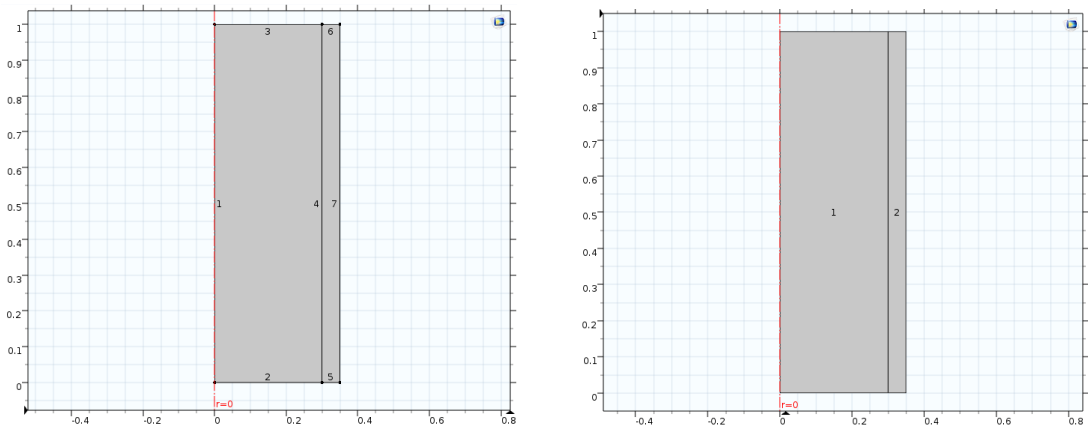


**Figure 12.** Geometry setup with 2D axisymmetric model with boundary and domain numbering

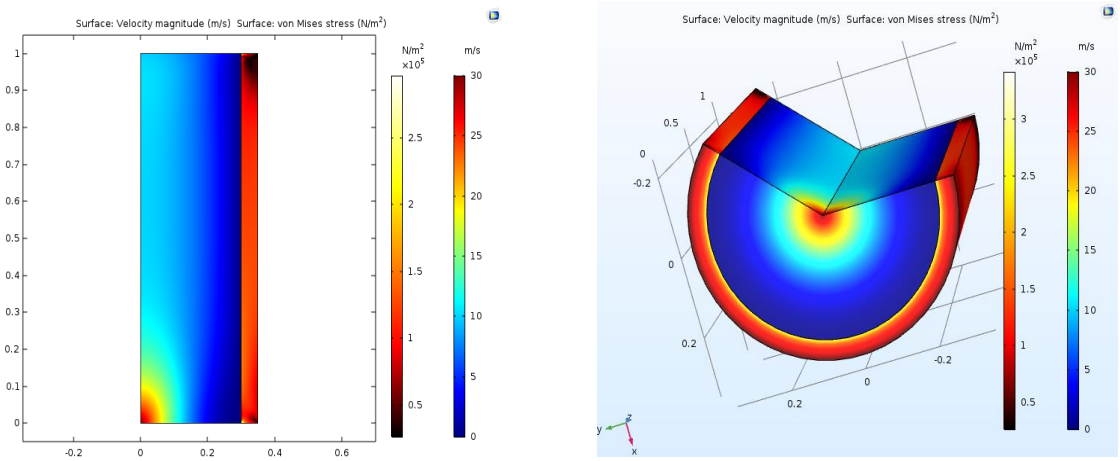


**Figure 13.** Simulation model with 2D axisymmetric

### 5.1.2 Boundary Setup and Governing Equation

This paper involves the pressure drop and heat transfer observation based on the types of coating, with particular emphasis on the elastic modulus of it. Table 5 shows the geometric setup with the 2D asymmetric model, and each number represents the domain and the boundary of the model. Since the coating is applied to the inner wall of the channel with electrodeposition, the outer boundary of the coating must be fixed because the channel is assumed to be a rigid wall, and do not move as the fluid flows. Table 6 shows this boundary condition. It must be noted that boundary setup is crucial to identify the effect of the deformable coating; if the outer boundary of the coating is not fixed, the entire coating is moved both in the radial and axial direction. Table 7 is introduced to observe the wall deformation where the boundary of the coating is set to free deformation in the radial direction. For the boundary and domain, the governing equation is shown in Table 8 and Table 9.

**Table 5.** Explanation for domain setup

| Domain numbering | Explanation |
|---|---|
| **1** | Fluid |
| **2** | Coating |

**Table 6.** Explanation for boundary setup 1

| Boundary numbering | Explanation | Notes |
|---|---|---|
| **1** | Axial Symmetry | - |
| **2** | Fluid inlet | - |
| **3** | Fluid outlet | - |
| **4** | Fluid-solid boundary | - |
| **5, 6** | Coating thickness | Fixed constraint |
| **7** | Outer boundary | Fixed constraint |

**Table 7.** Explanation for boundary setup 2

| Boundary numbering | Explanation | Notes |
|---|---|---|
| **1** | Axial Symmetry | - |
| **2** | Fluid inlet | - |
| **3** | Fluid outlet | - |
| **4** | Fluid-solid boundary | - |
| **5, 6** | Coating thickness | Prescribed Displacement |
| **7** | Outer boundary | Free deformation |

**Table 8.** Governing equation and condition at domain

| Position | | Equation |
|---|---|---|
| **Domain** | Water | $\rho\frac{\partial u_{fluid}}{\partial t}+\rho(u_{fluid}\cdot\nabla)u_{fluid}=$ $\nabla\cdot\left[-pI+\mu\left(\nabla u_{fluid}+(\nabla u_{fluid})^{T}\right)-\frac{2}{3}\mu(\nabla\cdot u_{fluid})I\right]+F$ $\frac{\partial\rho}{\partial t}+\nabla\cdot(\rho u_{fluid})=0$ |
| | TIMs | $\rho\frac{\partial^2 u_{solid}}{\partial t^2}-\nabla\cdot\sigma=Fv$ $\sigma=J^{-1}FSF^{T}$ $F=(I+\nabla u_{solid})$ $\mathrm{J}=\det(\mathrm{F})$ $\mathrm{S}-S_0=C:(\epsilon-\epsilon_0-\epsilon_{inel})$ $\epsilon=\frac{1}{2}[(\nabla u_{solid})^{T}+\nabla u_{solid}+(\nabla u_{solid})^{T}\nabla u_{solid}]$ |

**Table 9.** Governing equation and condition at boundary

| Position | | Equation | Condition |
|---|---|---|---|
| **Boundary** | Axial Symmetry | - | - |
| | Fixed Constraint | $u_{solid} = 0$ | - |
| | Free deformation | ALE | Initial mesh displacement = 0 |
| | Fluid-Solid boundary | $u_{fluid} = u_{wall}$<br>$u_{wall} = \frac{\partial u_{solid}}{\partial t}$<br>$\sigma \cdot n = \Gamma \cdot n$<br>$\Gamma = \left[-pI + \mu\left(\nabla u_{fluid} + (\nabla u_{fluid})^T\right) - \frac{2}{3}\mu(\nabla \cdot u_{fluid})I\right]$ | - |
| | Inlet | $u_{fluid} = -U_0 n$ | Boundary condition: v(t) = a + bsin(ct), or constant inlet velocity |
| | Outlet | $\left[-pI + \mu\left(\nabla u_{fluid} + (\nabla u_{fluid})^T\right) - \frac{2}{3}\mu(\nabla \cdot u_{fluid})I\right] n = -\hat{p}_0 n$<br>$\hat{p}_0 \leq p_0$ | Boundary condition: 1atm |
| | Prescribed Displacement | $w_{solid} = w_{solid0} = 0$ | - |

For ANSYS 18.0, fluid-structure interaction is considered by setting the fluid-solid interface, as shown in Figure 14.

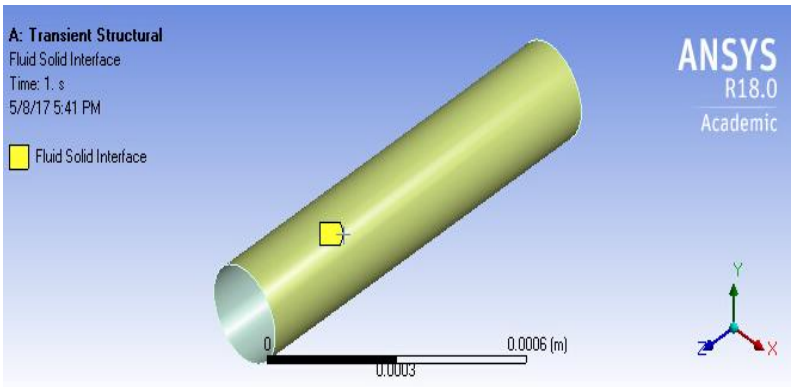


**Figure 14.** Fluid-Solid Interface setup with ANSYS 18.0

### 5.1.3 Grid Setup

In COMSOL 5.3 Multiphysics, triangular shape mesh is employed with coarse element size as described in Figure 15. Mesh smoothing type is set to Hyperelastic. In ANSYS 18.0, inflation meshing method is used at the fluid-solid intersection as shown in Figure 17, to consider the interaction of fluid and solid precisely.

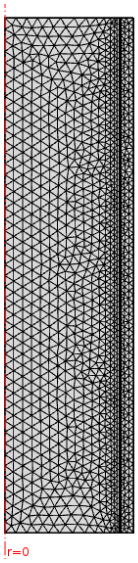


**Figure 15.** Mesh setting with COMSOL 5.3 Multiphysics

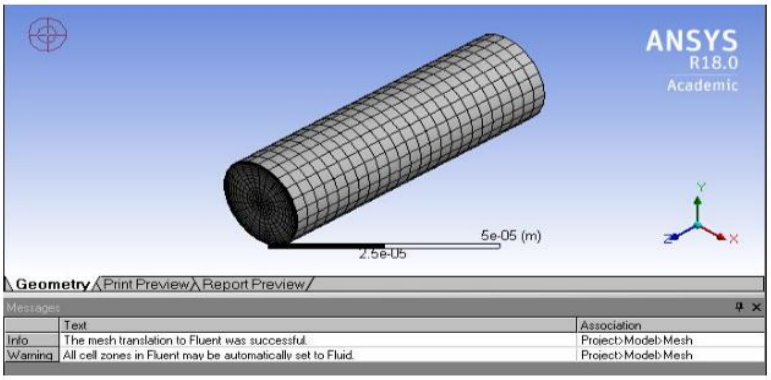


**Figure 16.** Meshing setting with ANSYS 18.0

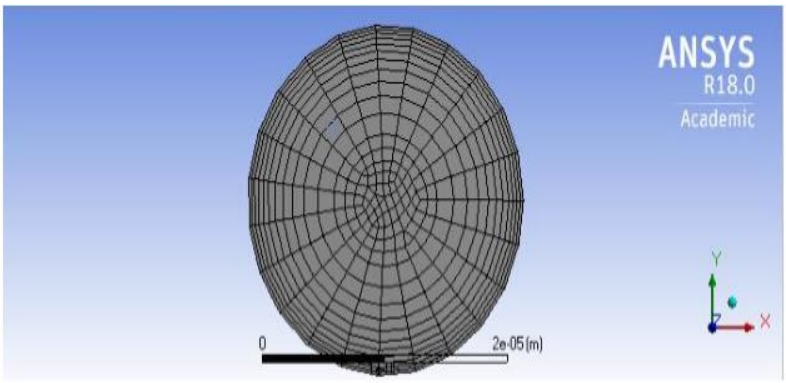


**Figure 17.** Inflation meshing method from z-axis with ANSYS 18.0

### 5.1.4 Material Setup

The author introduces two imaginary materials - one of which has ten times low elastic modulus than TIMs, and the other has a very large elastic modulus that we can assume this material as rigid – to compare the pressure drop and heat transfer characteristics by focusing on the 'deformable' aspects of the coating. The simulation is taken under four kinds of coating as indicated below:

1. TIMs (deformable wall)
2. Rigid material (almost rigid)
3. Imaginary material (more deformable than TIMs)
4. Aluminum

The author uses the property data of TIMs from the paper (Yegin et al., 2017) and sets the properties of the rigid and imaginary material, with particular emphasis on the 'deformable' properties. TIMs, Rigid material, and the Imaginary material are different in properties of - Elastic modulus and the Poisson's ratio - to see the effect of 'deformable' feature on pressure drop and the heat transfer. The term 'Rigid wall', 'IMG' are used for rigid material and the imaginary material, respectively. Aluminum is also introduced to compare the performance of TIMs coating, and the COMSOL 5.3 data is used for Aluminum properties. Liquid water is used for the fluids, and the properties of materials are specified in Table 10, Table 11, Table 12, and Table 13.

**Table 10.** Properties of TIMs

| Property | Value | Unit |
|---|---|---|
| **Density** | 7332 | $kg/m^3$ |
| **Young's modulus** | 24.85 | GPa |
| **Poisson's ratio** | 0.337 | 1 |
| **Thermal conductivity** | 244 | W/(m·K) |
| **Heat capacity at constant pressure** | 440 | J/(kg·K) |

**Table 11.** Properties of Rigid wall

| Property | Value | Unit |
|---|---|---|
| **Density** | 7332 | $kg/m^3$ |
| **Young's modulus** | $24.85\times10^5$ | GPa |
| **Poisson's ratio** | 0.2 | 1 |
| **Thermal conductivity** | 244 | W/(m·K) |
| **Heat capacity at constant pressure** | 440 | J/(kg·K) |

**Table 12.** Properties of Imaginary material (IMG)

| Property | Value | Unit |
|---|---|---|
| **Density** | 7332 | $kg/m^3$ |
| **Young's modulus** | 2.485 | GPa |
| **Poisson's ratio** | 0.44 | 1 |
| **Thermal conductivity** | 244 | W/(m·K) |
| **Heat capacity at constant pressure** | 440 | J/(kg·K) |

**Table 13.** Properties of Aluminum

| Property | Value | Unit |
|---|---|---|
| **Density** | 2700 | $kg/m^3$ |
| **Young's modulus** | 70 | GPa |
| **Poisson's ratio** | 0.33 | 1 |
| **Thermal conductivity** | 238 | W/(m·K) |
| **Heat capacity at constant pressure** | 900 | J/(kg·K) |

### 5.1.5 Assumption

In this paper, the following assumptions are introduced to describe the relationship between the fluid flows and the deformable coating.

1. The fluid flow is laminar, incompressible and continuum
2. Steady heat transfer
3. Roughness of microchannels in all models is of the same order
4. The materials used for coating are linear elastic
5. A parabolic velocity profile is prescribed at the inlet as follows:

$$\mathrm{v}(0, y) = 1.5U_{mean}\frac{y(H-y)}{\left(\frac{H}{2}\right)^2} \qquad eq.(20)$$

This equation is transformed to symmetric form:

$$\mathrm{v}(\mathrm{r}, 0) = 6U_{mean}\frac{(D_h - r)^2}{(D_h)^2} \qquad eq.(21)$$

6. Entrance length is considered to remove the entrance effect.

At the entrance and the exit of the microchannel, it usually involves the contraction and expansion effect. These abrupt changes of the flow area induce additional pressure drops.

$$\Delta\mathrm{P} = \Delta P_1 + \Delta P_2 + \Delta P_3 \qquad eq.(22)$$

Where $\Delta P_1 = P_1 - P_2$ : pressure loss due to contraction at the entrance, $\Delta P_2 = P_2 - P_3$ : pressure loss in the microchannel, $\Delta P_3 = P_3 - P_4$ : pressure loss due to expansion at the exit.

In this paper, the pressure loss at the entrance ($\Delta P_1$) and the exit ($\Delta P_3$) is not considered, and the entrance length is introduced to consider the pressure loss only in the microchannel ($\Delta P_2$). For laminar flow, this length is given by:

$$L_{entrance} = 0.05 R_e D_h \qquad eq.(23)$$

With the COMSOL Multiphysics 5.3., the entrance effect is considered by setting up the point that is away from the inlet by $L_{entrance}$, as shown in Figure 18. Pressure drop and the heat transfer performance is considered from this point, and fully developed laminar flow is assumed by considering the entrance length.

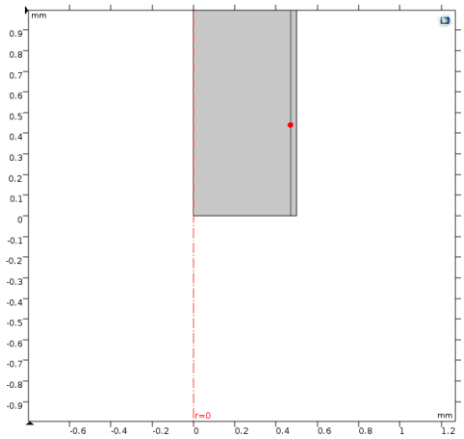


**Figure 18.** Brief illustration showing the point with heights $\boldsymbol{L_{entrance}}$

## 5.2 Pressure Drop Observation

To reiterate the main focus: Constant density is used for the material of the coating; if all the boundary of the wall is fixed, the boundary except the fluid-solid intersection does not move.

First, this paper observe pressure drop when deformable wall is applied to see how the deformable wall works when the fluid flow when the outer boundary of the wall is not fixed (Boundary setup 2). Model Setup 1 is described in Table 14, and the computed result about the pressure drop is shown in Figure 19.

**Table 14.** Model setup with TIMs coating

| Model dimension | Value | Unit |
|---|---|---|
| **Channel radius** | 100 | um |
| **TIMs thickness** | 50 | um |
| **Channel length** | 1 | mm |
| **Inlet velocity** | 3.33 | cm/s |
| **Outlet pressure** | 0 | Pa |
| **Reynolds number** | 7.9 | - |

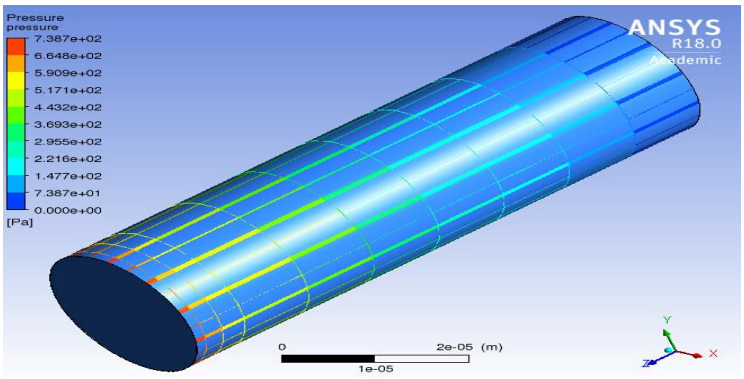


**Figure 19.** Pressure drop according to the wall with TIMs coating

In Figure 19, the pressure drop is 738.7 Pa. The simulation results with the same experimental setup besides the coating material (changed from TIMs to Aluminum) are also conducted.

**Table 15.** Model Setup with Aluminum

| Model dimension | Value | Unit |
|---|---|---|
| **Channel radius** | 100 | um |
| **Al thickness** | 50 | um |
| **Channel length** | 1 | mm |
| **Inlet velocity** | 3.33 | cm/s |
| **Outlet pressure** | 0 | Pa |
| **Reynolds number** | 7.9 | - |

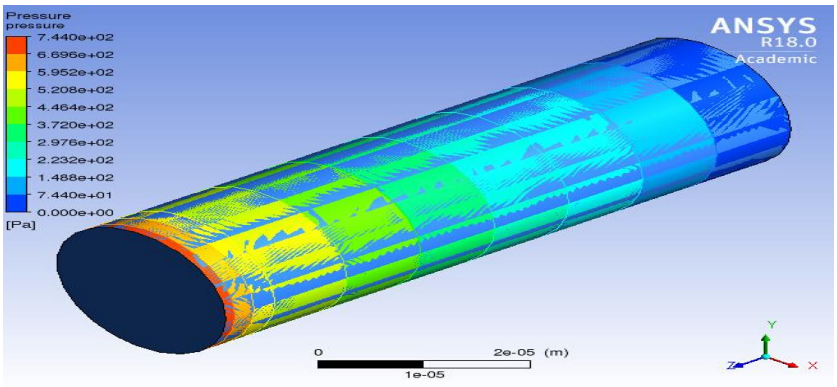


**Figure 20.** Pressure drop according to the wall with Aluminum

The pressure drop is 744Pa as shown in Figure 20, which is higher than the case of TIMs coating (738.7Pa). Now we know that the pressure drop can be reduced when we apply the deformable coating. We can reduce the pressure drop by 5300 Pa/m with TIMs coating compared to the Conventional Aluminum wall when the outer boundary of the wall is not fixed (Boundary setup 2).

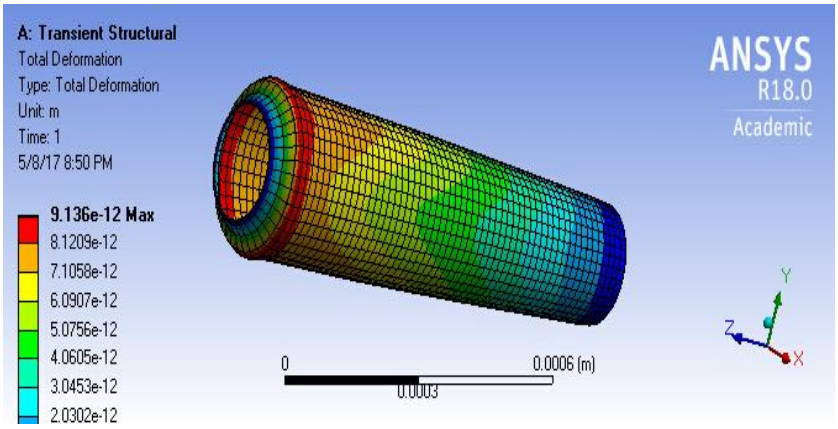


**Figure 21.** Free deformation of the deformable wall

With the COMSOL 5.3 Multiphysics, the pressure drop is observed depending on the types of the coating, when the boundary setup 2 is applied.

**Table 16.** Pressure drop observation with TIMs coating and the rigid wall

| Model | Hydraulic diameter (mm) | Coating thickness (um) | Inlet velocity (m/s) | Channel length (cm) | ΔP/L (Pa/m) |
|---|---|---|---|---|---|
| **TIMs coating** | 0.94 | 30 | 0.1 | 1 | 3876.2 |
| **TIMs coating** | 0.74 | 30 | 0.1 | 1 | 6752.3 |
| **TIMs coating** | 0.54 | 30 | 0.1 | 1 | 13642.8 |
| **TIMs coating** | 0.34 | 30 | 0.1 | 1 | 38533.3 |
| **TIMs coating** | 0.14 | 30 | 0.1 | 1 | 310227.4 |
| **Rigid wall** | 0.94 | 30 | 0.1 | 1 | 3940.7 |
| **Rigid wall** | 0.74 | 30 | 0.1 | 1 | 6820.6 |
| **Rigid wall** | 0.54 | 30 | 0.1 | 1 | 13771.5 |
| **Rigid wall** | 0.34 | 30 | 0.1 | 1 | 39050.6 |
| **Rigid wall** | 0.14 | 30 | 0.1 | 1 | 312199.3 |

Table 16 shows the models developed to see the pressure drop effect according to the hydraulic diameter of the channel and the elastic modulus of the wall. The computed data shows that the TIMs coating reduces the pressure drop. Figure 22 shows the reduction of ‘pressure drop’ between the rigid wall and the TIMs coating.

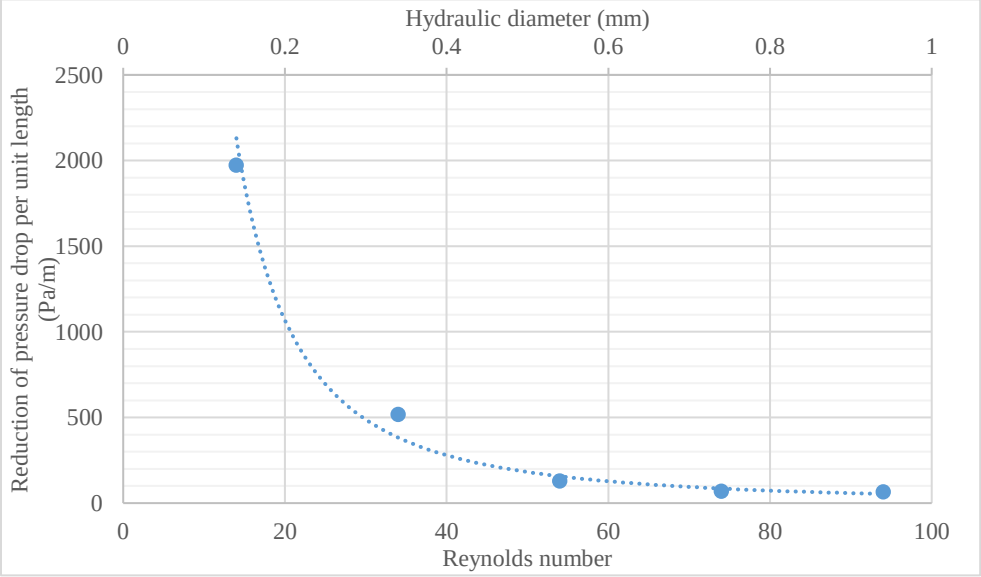


**Figure 22.** Reduction of pressure drop per unit length

It should be noted that the pressure drop difference between the TIMs coating and the rigid wall becomes higher when the channel diameter is decreased. Small hydraulic diameter enhances the performance of the deformable coating.

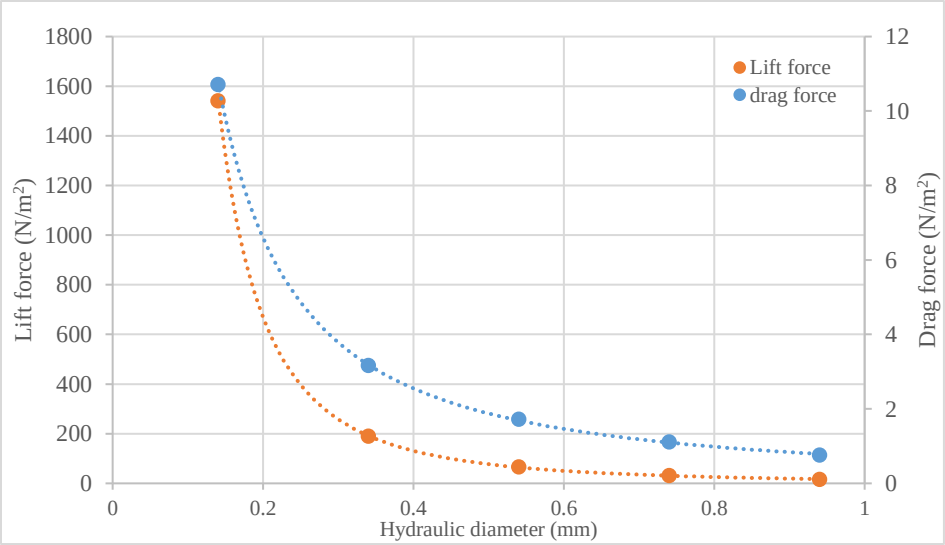


**Figure 23.** Lift and drag force with TIMs coating

Figure 23 shows the lift and drag force when TIMs coating is applied. It shows that both lift and drag force is increased when the hydraulic diameter is small. The lift and drag force is observed for various hydraulic diameter, and the data is shown in Table 17.

**Table 17.** Lift and drag force with TIMs coating and the rigid wall

| Model | Hydraulic diameter (mm) | Coating thickness (um) | Inlet velocity (m/s) | Channel length (cm) | Lift force ($N/m^2$) | Drag force ($N/m^2$) |
|---|---|---|---|---|---|---|
| **TIMs coating** | 0.94 | 30 | 0.1 | 1 | 16.697 | 0.76839 |
| **TIMs coating** | 0.74 | 30 | 0.1 | 1 | 18.665 | 0.84024 |
| **TIMs coating** | 0.54 | 30 | 0.1 | 1 | 20.842 | 0.91835 |
| **TIMs coating** | 0.34 | 30 | 0.1 | 1 | 31.852 | 1.1128 |
| **TIMs coating** | 0.14 | 30 | 0.1 | 1 | 35.885 | 1.2286 |
| **Rigid wall** | 0.94 | 30 | 0.1 | 1 | 16.929 | 0.77639 |
| **Rigid wall** | 0.74 | 30 | 0.1 | 1 | 32.176 | 1.1195 |
| **Rigid wall** | 0.54 | 30 | 0.1 | 1 | 67.326 | 1.7287 |
| **Rigid wall** | 0.34 | 30 | 0.1 | 1 | 192.11 | 3.1778 |
| **Rigid wall** | 0.14 | 30 | 0.1 | 1 | 1551.2 | 10.666 |

From Table 17, it has been noticed that both the lift force and the drag force are reduced when the deformable coating is applied. From Table 17, the difference of drag force with different coatings is plotted in Figure 24.

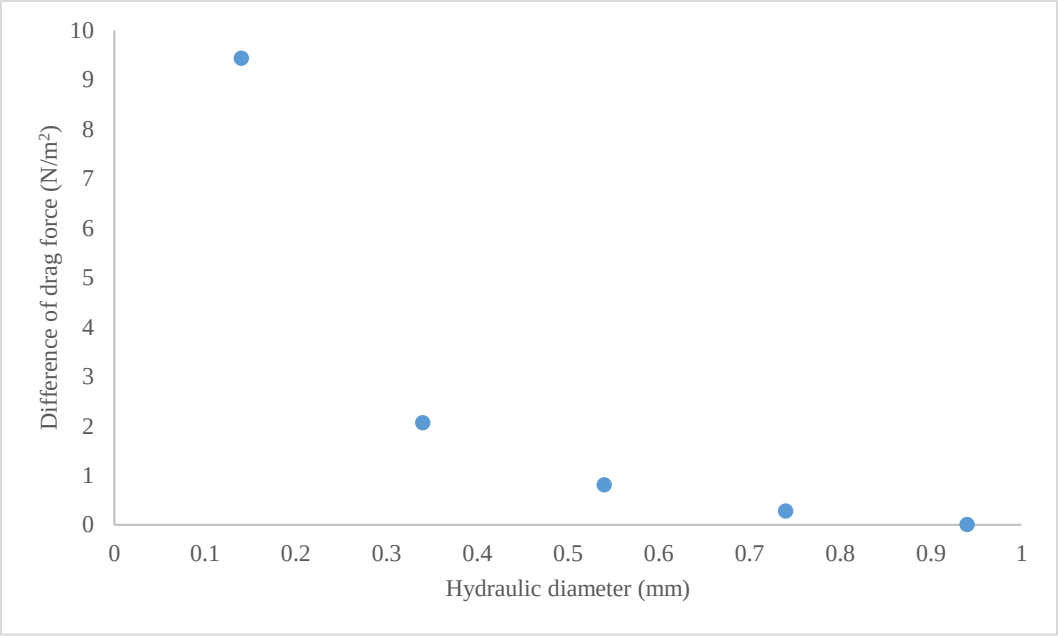


**Figure 24.** Difference of lift and drag force between rigid wall and the TIMs

In general, the pressure drop reduction can be explained by the drag force. Pressure and shear forces that act on the surface of the object – here, the inner boundary of the coating – is the drag force. The tangential shear stresses produce the friction drag, and the pressure drop is influenced by the friction drag. The drag force along the channel is small when the deformable coating is applied, which results in the reduction of pressure drop.

Figure 25 shows the pressure drop with various thickness of the coating. It indicates that lower thickness shows better performance on the pressure drop reduction. This is because the wall deformation is large (with free boundary) when the coating thickness is small, as shown in Figure 26. Large wall deformation leads to more flow area, which allows the fluid to lose less energy.

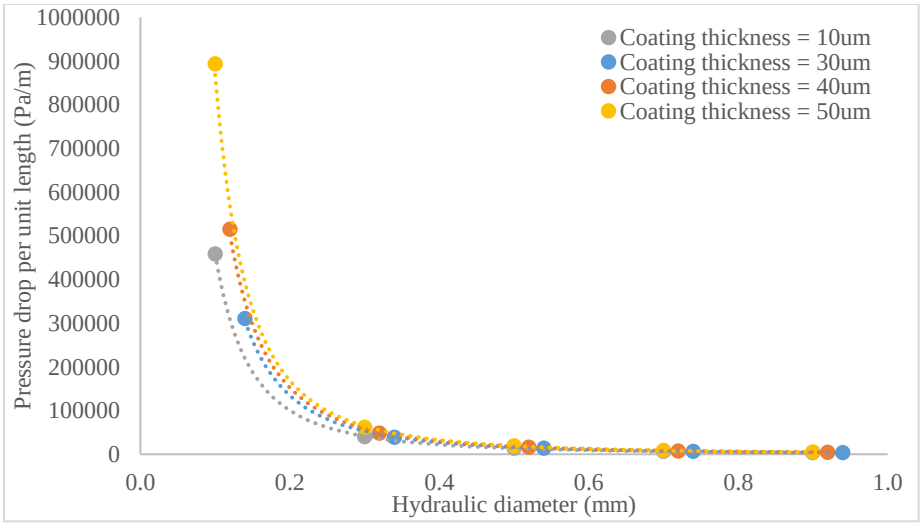


**Figure 25.** Pressure drop per unit length according to the coating thickness of TIMs

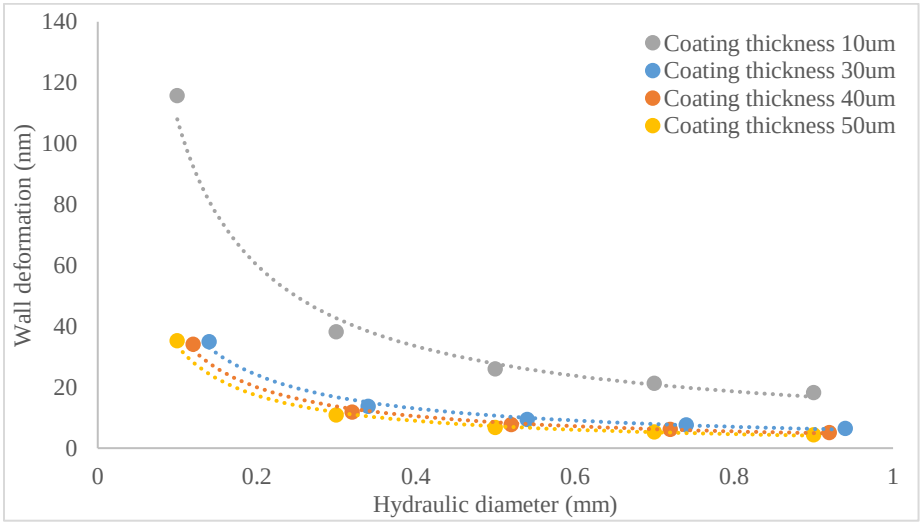


**Figure 26.** Wall deformation according to the coating thickness of TIMs

With non-fixed boundary setup for coating domain, pressure drop performance on various types of the coating is investigated so far. For the rest part, COMSOL 5.3 is used for the simulation, and only the boundary Setup 1 (Fixed boundary) is employed because the outer boundary of the wall does not move in reality as fluid flows.

### 5.2.1 Wall Deformation

The wall behavior is observed when the periodic flow is induced at the entrance. The linear projection method is used to simulate it. Details about linear projection method are shown in Figure 27 and Equation 24.

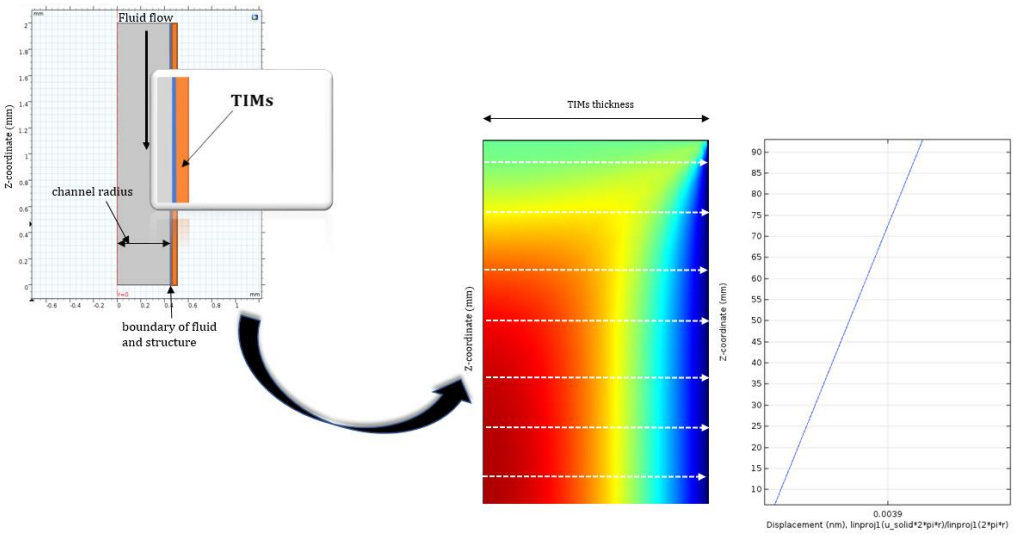


**Figure 27.** Displacement field with arrows representing the line integrals and the resulting average displacement field

Figure 27 shows the wall displacement regarding r-direction and total wall direction (r-direction + z-direction) according to the z-direction, respectively. Average wall displacement can be evaluated by the linear integral operator, which uses the following equation 24.

$$u_{solid}(z) = \frac{1}{A(z)} \int_{R}^{r} u_{solid}(z, r) \cdot 2\pi \cdot r dr = \frac{linproj1(u_{solid} \cdot 2\pi \cdot r)}{linproj1(2\pi \cdot r)} \qquad \text{eq. (24)}$$

Where $u_{solid}(z)$ is displacement field, $r - component$.

In the same manner, $z-$component displacement field ($w_{solid}$) and the total displacement field ($disp_{solid}$) can be obtained. Here, the relationship between the displacement field of the wall is,

$$disp_{solid} = u_{solid} + w_{solid} \qquad \text{eq. (25)}$$

The wall displacement field which is parallel to the flow direction ($w_{solid}$) is shown in Figure 29 (Left). The total wall displacement field ($disp_{solid}$) is shown in Figure 29 (Right). The scale of wall displacement field that is parallel to the flow direction ($w_{solid}$) is $10^{-8}nm$ while $disp_{solid}$ is around $10^{-3}nm$. From the equation (25), we can know that:

$$w_{solid} \approx disp_{solid}$$

Therefore,

$$u_{solid} \times 10^{-5} \approx w_{solid}$$

$$w_{solid} \ll u_{solid}$$

The amount of $w_{solid}$ is negligible compared to $u_{solid}$. The scale difference between the $w_{solid}$ and the $u_{solid}$ can be explained by the scale difference between lift and drag force (drag force << lift force), as described in Figure 23. Drag force may induce the wall deformation in z-direction, while the lift force the wall deformation in r-direction.

Noticing that Figure 23 describes the drag and lift force with different boundary setup (Boundary setup 2), and also noticing the scale difference between them (lift force $\approx 100 \times$ drag force), we can reason that the difference 'magnitude' of the drag and lift force becomes larger when the outer boundary of the wall is fixed (Boundary setup 1) (Here, $u_{solid} \times 10^{-5} \approx w_{solid}$, and may have similar scale difference between the drag and lift force).

We know that the pressure drop is generally explained by the drag force. However, the lift force and the following r-direction movement ($u_{solid}$) is also related to the energy loss when fluid flows through the channel (which can be converted to the pressure drop

term). If we can reduce the lift force – In this research, with deformable coating –, it can significantly reduce the pressure drop across the channel by saving the energy loss when fluid flows through the channel.

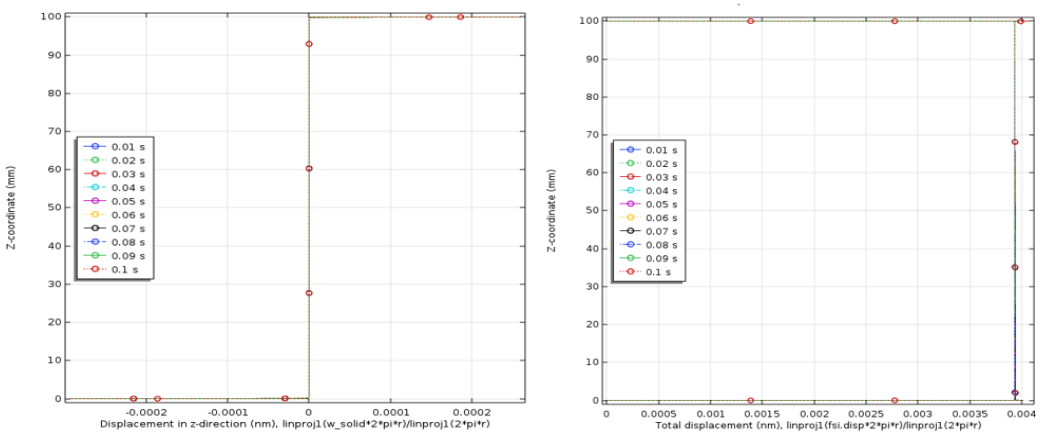


**Figure 28.** Displacement of the wall along the axial direction with linear projection method (Left: $\mathbf{w_{solid}}$, Right: $\mathbf{disp_{solid}}$)

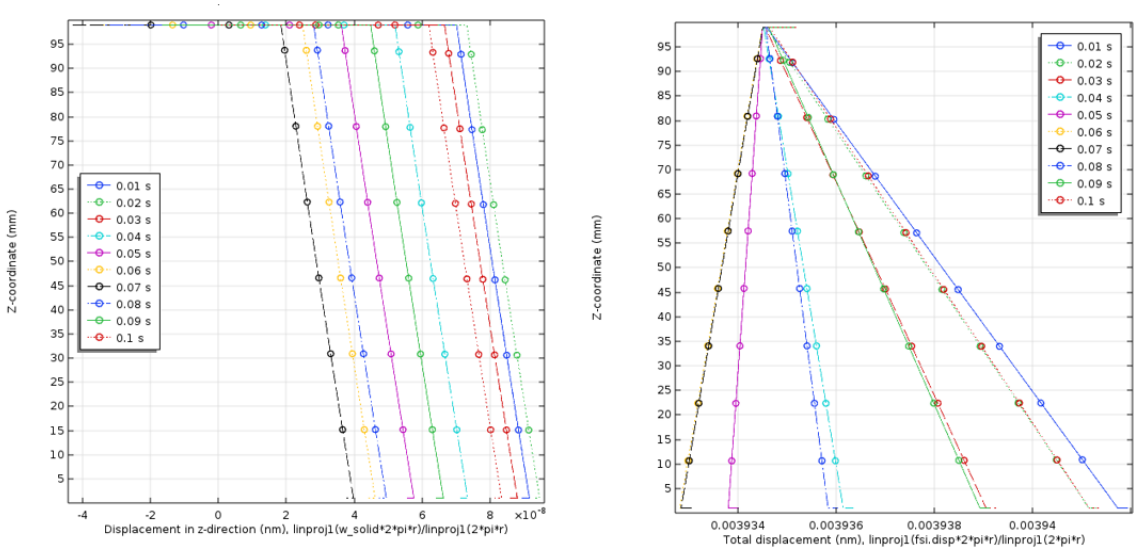


**Figure 29.** Wall deformation when pulsed flow is induced (Left: $\mathbf{w_{solid}}$, Right: $\mathbf{disp_{solid}}$)

In this case, Inlet velocity function $v(t) = 0.01\times(1 + \sin ct)\ m/s$ is used when D/λ= 1, λ is 0.94mm, T (period) is 0.09. From Figure 29, it can be noticed that the wall displacement changes with response to the inlet velocity function, and the period of 'wall displacement' is almost same as the period of inlet velocity function.

With this scale, however, it turns out that the pressure drop is same regardless of the types of the wall, while the deformation of the wall is different as shown in Figure 30 and Figure 31.

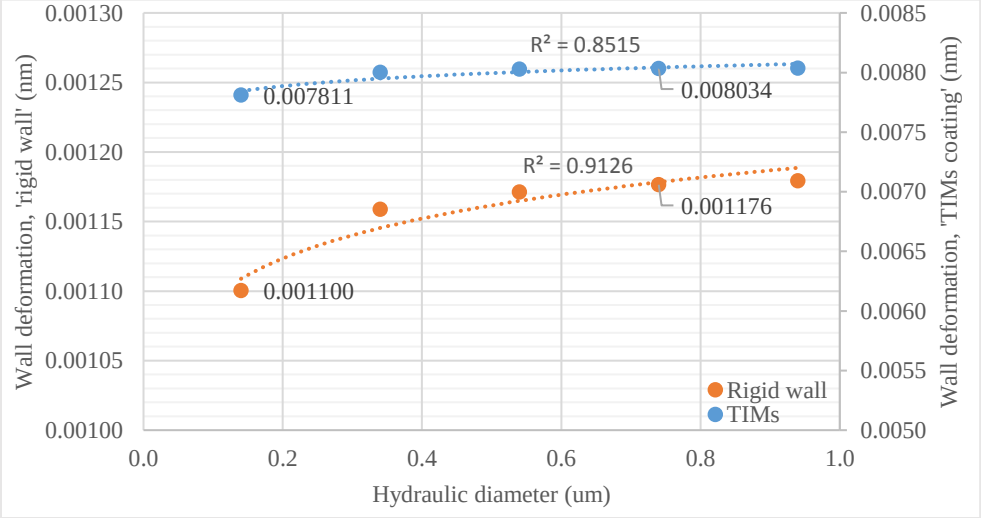


**Figure 30.** Wall deformation according to types of coating

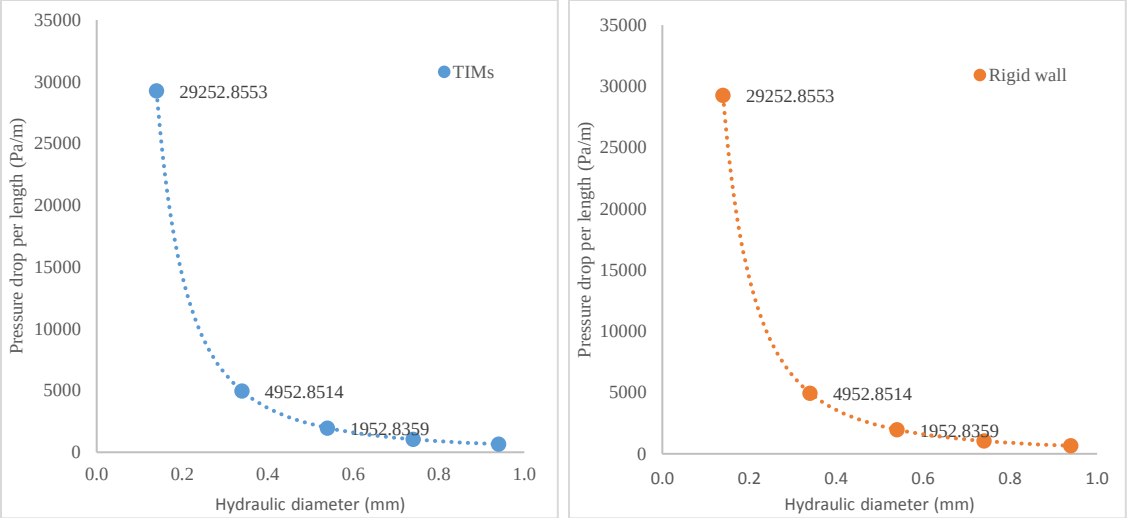


**Figure 31.** Pressure drop per unit length with different types of coating

The difference of pressure drop according to the types of the coating is not detected as well when constant inlet velocity is induced. In the beginning, the author started the investigation with the scale around $D_{hydraulic} \approx 0.1\sim1mm$, Inlet velocity $\approx 0.01m/s$, length $\approx 0.1m$, Reynolds number $\approx 1\sim10$, and changes the inlet velocity as high as possible, but the difference of pressure drop is not seen in this scale.

From Section 5.2, we can see the difference of pressure drop according to the types of coating around this scale ($D_{hydraulic} \approx 0.2mm$). This is because the outer boundary of the wall is not fixed (Boundary setup 2), and it is quite sure that the wall deformation is much larger in this boundary setup. We also know from Figure 25 and Figure 26 that the large wall deformation induces less pressure drop. Therefore, we can think that the wall deformation is the most critical part that determines the pressure drop.

It leads to the conclusion that the pressure drop is not affected by the deformable coating in this scale when the outer boundary of the wall is fixed (Boundary setup 1). This is because the amount of 'deformation of the coating' is negligible relative to the hydraulic diameter of the channel. Therefore, the fluid flow is not changed by the wall deformation.

$$\frac{Wall\ deformation}{D_{hydraulic}} = \frac{0.003936nm}{0.94mm} \approx 4.187\times10^{-9}$$

The ratio of wall deformation to hydraulic diameter is around $10^{-9}$, and the difference of pressure drop is not observed in this scale.

### 5.2.2 Pressure Drop with Constant Inlet Velocity

We know from Figure 22 that pressure drop difference between the TIMs coating and the rigid wall becomes higher when the channel diameter is decreased. That is, small hydraulic diameter enhances the performance of the deformable coating. Therefore, with boundary setup 1, models with significantly smaller hydraulic diameter are introduced to observe the pressure drop according to the types of coating (Increase the ratio of the wall deformation to hydraulic diameter).

$$\frac{Wall\ deformation}{D_{hydraulic}} \approx 10^{-5}$$

**Table 18.** Fixed and control variable

| Fixed variable | | Control variable | |
|---|---|---|---|
| **Length (um)** | **Coating thickness (um)** | **Hydraulic diameter (um)** | **U_mean (m/s)** |
| 100 | 1 | 2 | 5 |
| | | 3 | 6.5 |
| | | 4 | 8 |
| | | 5 | 9 |
| | | 6 | 10 |

With the model described in Table 18, the pressure drop is investigated according to the types of coating. To see the difference of 'pressure drop' clearly, the subtracted value is used.

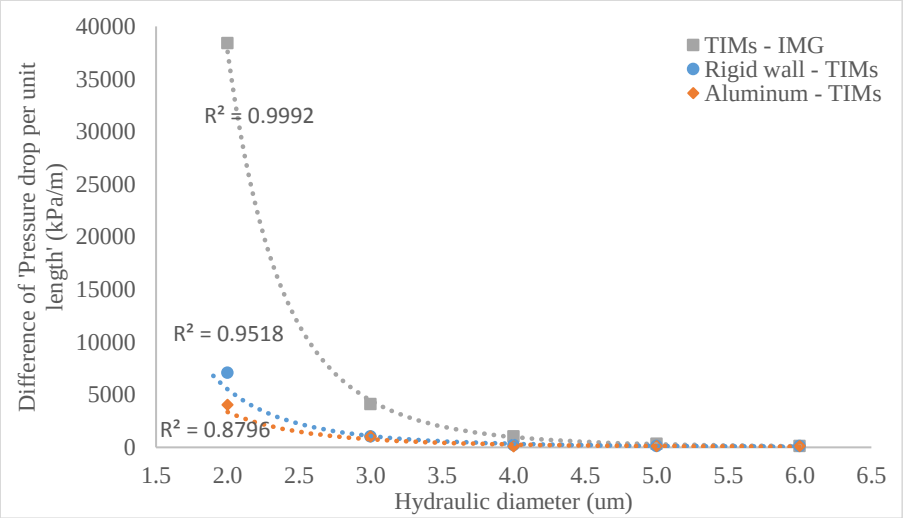


**Figure 32.** Difference of pressure drop according to the types of coating when $U_{mean}$ = 5m/s

Figure 32 shows the difference of 'pressure drop' across the channel with different types of coating. TIMs shows better performance on reducing the pressure drop than rigid wall and Aluminum. IMG, which has ten times low elastic modulus than the TIMs, reduce the pressure drop significantly than TIMs. Therefore, the 'deformable' rate of coating is the criterion to reduce the pressure drop. It has to be noted that the 'performance' of the deformable wall in terms of reducing pressure drop is high when the hydraulic diameter is small. For this model, the 'difference' of pressure drop per types of the coating is reduced, which indicate that the performance of deformable coating becomes small when the hydraulic diameter becomes large. In addition to the hydraulic diameter, inlet velocity is one of the factors that induces the large pressure drop. Therefore, pressure drop performance based on the inlet velocity is investigated.

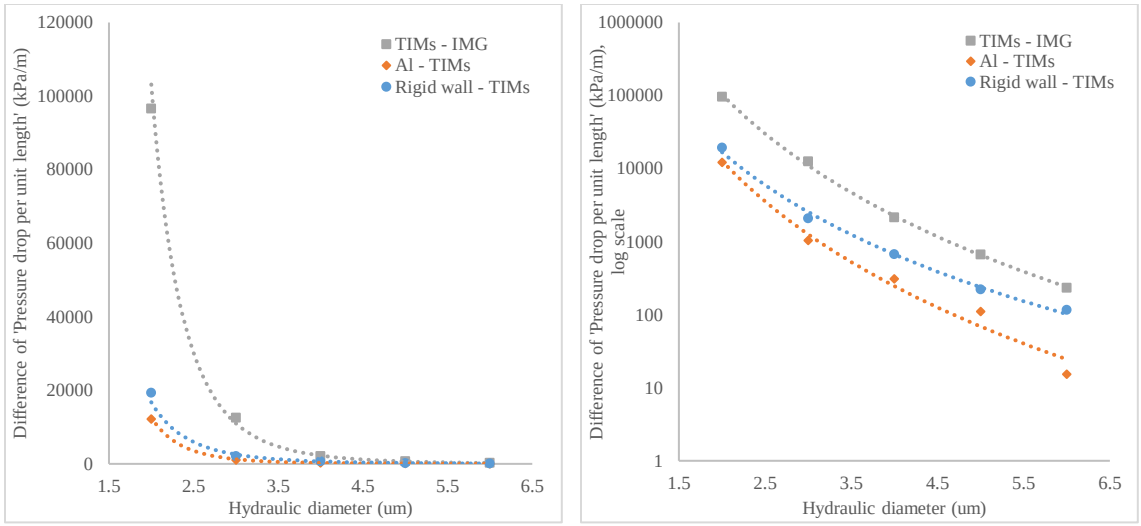


**Figure 33.** Difference of pressure drop according to the types of coating when $U_{mean}$ = 8m/s

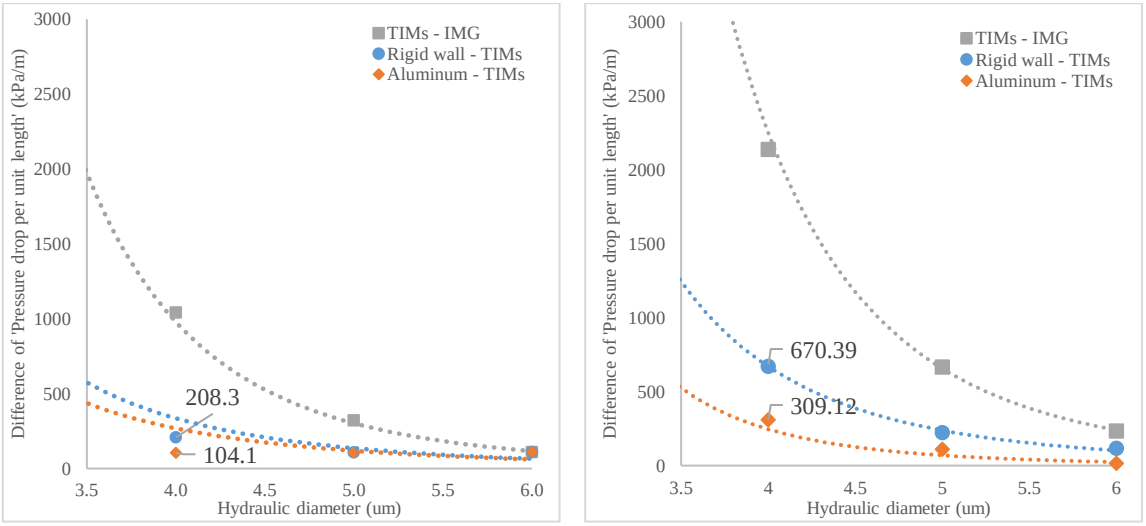


**Figure 34.** Magnified graph for Figure 32 and Figure 33 (Left: $U_{mean}$ = 5m/s, right: $U_{mean}$ = 8m/s)

From Figure 33 and Figure 34, we can know that the pressure drop becomes large when inlet velocity is increased. With high inlet velocity, the performance of deformable wall can increase.

Performance of deformable coating $\propto$ inlet velocity

Considering that Aluminum is widely used for a heat exchanger, TIMs coating can be applied to reduce the pressure drop for the scale discussed. This paper is intended to show the potential of deformable and high thermally conductive coating which can be applied to the inside of the metal channel and proves the potential in the nanoscale channel.

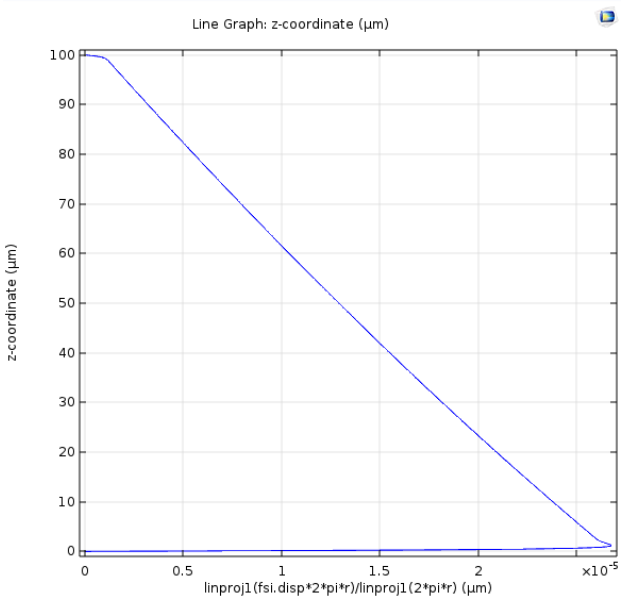


**Figure 35.** Wall deformation when the constant inlet velocity is applied

Figure 35 shows the wall deformation when $D_h$ = 2um, Channel length is 100um, thickness of coating is 1um, and the $U_{mean}$ is 5m/s. The graph shows that the wall deformation is high at the point near the inlet and reduces as linear shape to the outlet. Because the fixed constraints is set at the inlet and the outlet of the coating, the wall deformation is zero at the inlet at the outlet. It can be observed from the Figure 35 that the deformable wall try to make a cone shape to reduce the pressure drop.

With the model setting conducted in Figure 35, velocity at the inlet reaches the maximum value and decreases because of the friction, and the pressure drop is large when

the velocity is high. Therefore, the wall deformation reaches a maximum at the inlet, followed by the cone shape of the wall deformation. The wall deformation decreases according to the axial direction because of the constant density of the coating.

Figure 36 shows the image of total displacement and the fluid velocity when $D_h$ = 200nm, Channel length is 70um, the thickness of coating is 75nm, and $U_{mean}$ is 5m/s. Careful observation on the fluid-wall boundary reveals that the wall deforms slightly to the radial direction at the inlet, as Figure 35 describes before.

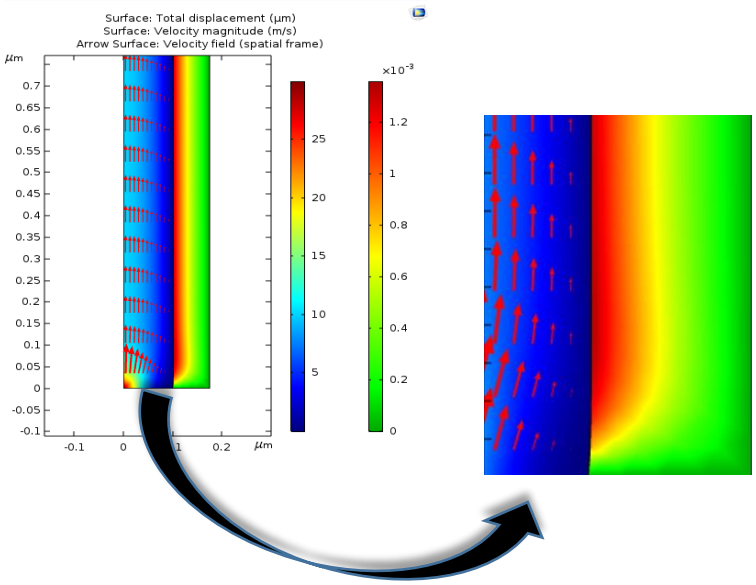


**Figure 36.** Brief illustration showing total displacement and the fluid velocity

### 5.2.3 Roughness and the Pressure Drop

Surface roughness is one of the major problems that induces the large pressure drop. In reality, well-fabricated surfaces of a microchannel that appear smooth to the naked eye turn out to quite rough at the micro levels. The performance of deformable wall can be more clearly proved when the roughness is introduced. Two different rough-wall cases (Root mean square roughness (RMS) heights is $0.0125D_h$ and $0.025D_h$) are investigated.

Here, RMS roughness is calculated as

$$R_q = \left( \frac{1}{mn} \sum_{k=0}^{m-1} \sum_{l=0}^{n-1} (Z(x_k, y_l) - \mu)^2 \right)^{0.5} \qquad eq.(26)$$

Where, $\mu = \frac{1}{mn} \sum_{k=0}^{m-1} \sum_{l=0}^{n-1} Z(x_k, y_l)$

Figure 37, Figure 38, and Figure 39 shows the surface profiles according to the channel axis. These roughness heights are generated using the random function in excel.

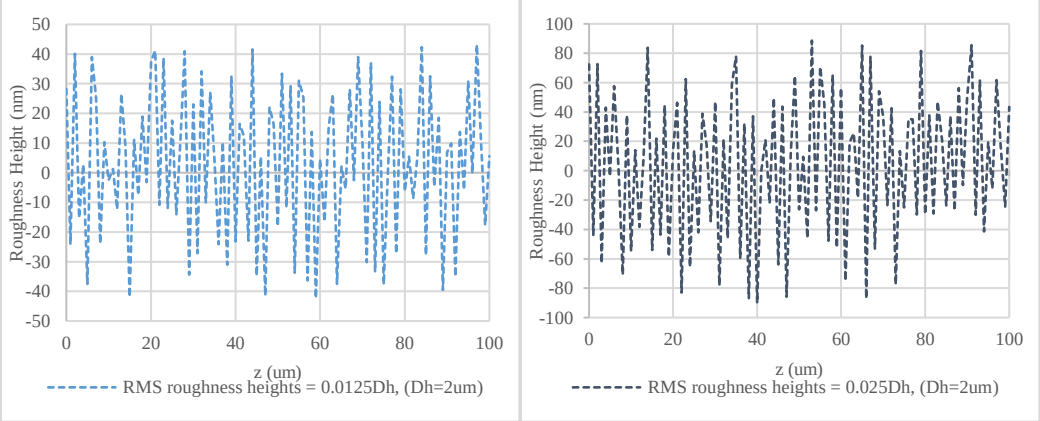


**Figure 37.** Line traces of roughness heights when $D_h$ = 2um

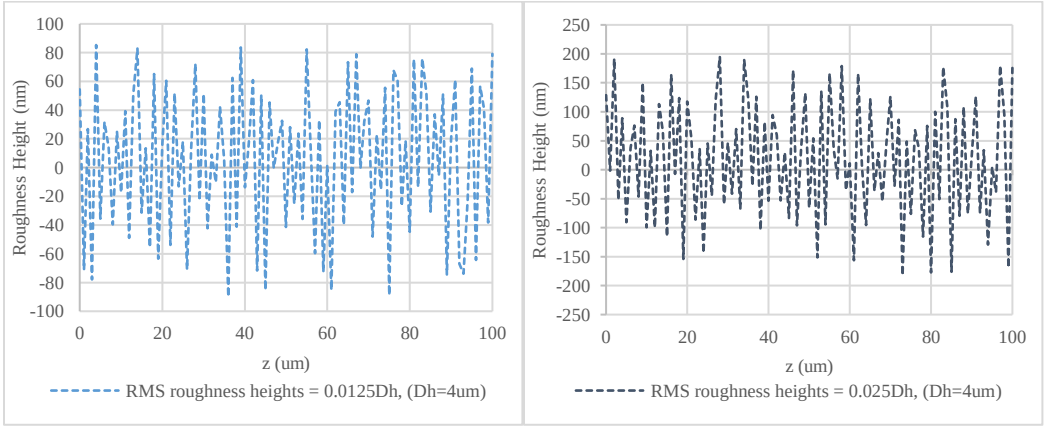


**Figure 38.** Line traces of roughness heights when $D_h$ = 4um

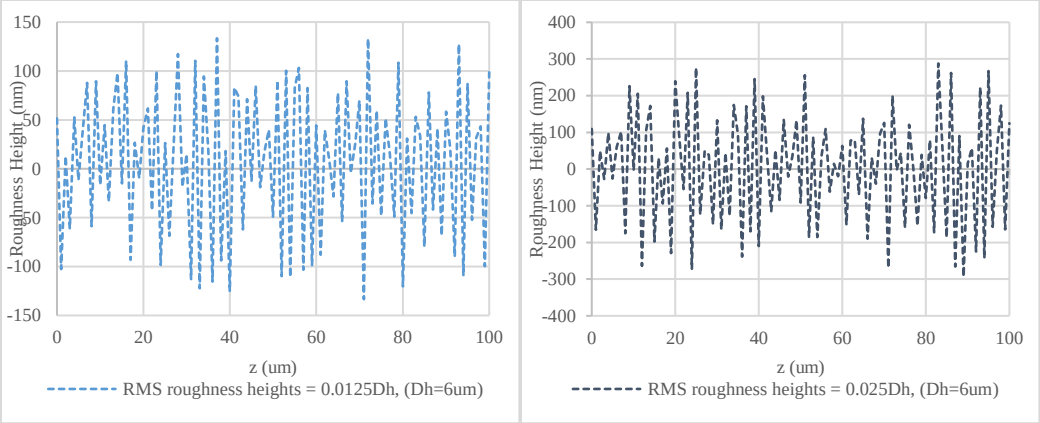


**Figure 39.** Line traces of roughness heights when $D_h$ = 6um

These surface conditions are generated with a probability density functions (pdfs) in Figure 40 and Figure 41.

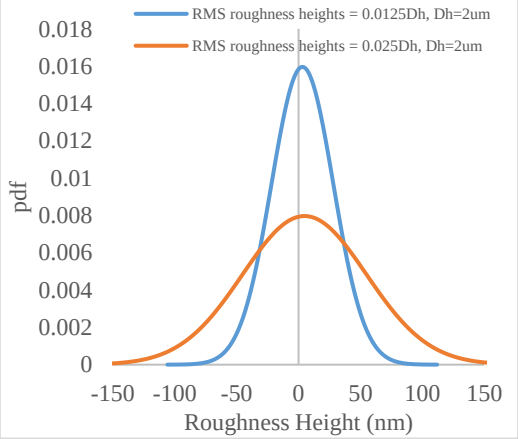


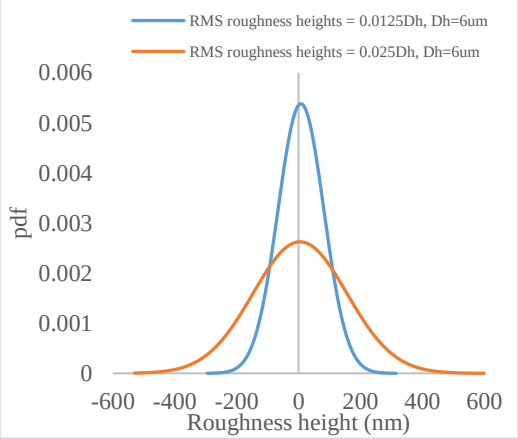


**Figure 40.** Pdfs of the roughness height when $D_h$ = 2um **Figure 41.** Pdfs of the roughness height when $D_h$ = 6um

RMS roughness heights are incorporated with the COMSOL 5.3 Multiphysics, and the following meshing are shown in Figure 42.

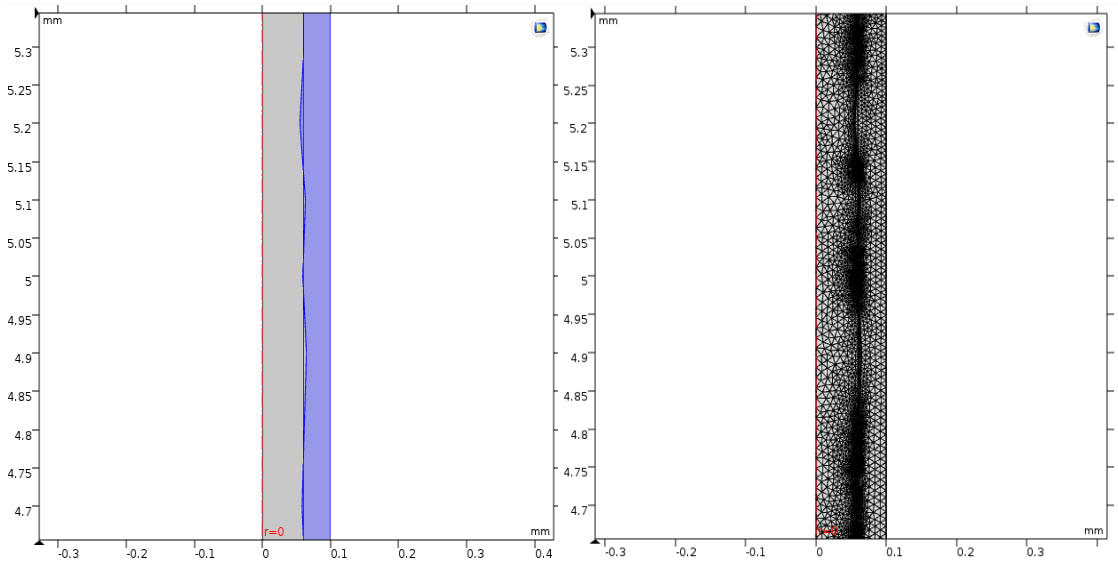


**Figure 42.** Model geometry and the meshing when RMS roughness heights of 2.523um (0.025$D_h$) is introduced

The pressure drop according to the hydraulic diameter is investigated on two RMS roughness heights. Table 19 shows the pressure drop per unit length according to the hydraulic diameter. To see the difference clearly, the subtracted value is used when plot the graph (e.g., Rigid wall – TIMs in the graph shows the 'Pressure drop with rigid wall minus pressure drop with TIMs coating').

**Table 19.** Fixed and control variables when roughness is introduced

| Fixed variable | | | Control variable | |
|---|---|---|---|---|
| **Length (um)** | **Coating thickness (um)** | **Inlet velocity (m/s)** | **Hydraulic diameter (um)** | **Roughness** |
| 100 | 1 | 5 | 2 | Smooth wall |
| | | | 3 | RMS roughness heights = 0.0125Dh |
| | | | 4 | RMS roughness heights = 0.025Dh |

The Figure 43 shows that the TIMs coating saves the pressure drop around 7080.52kPa/m when compared to the rigid wall. As the coating becomes more deformable, the pressure drop along the coating is reduced. This pressure drop reduction can be explained by the drag force. Pressure and shear forces that act on the surface of the object

– here, the inner boundary of the coating – is the drag force. The tangential shear stresses produce the friction drag, and the pressure drop is influenced by the friction drag. The drag force along the channel is small when the deformable coating is applied, which results in the reduction of pressure drop. Figure 43 and Figure 44 is conducted on the RMS roughness heights of $0.0125D_h$ and RMS roughness heights of $0.025D_h$, respectively.

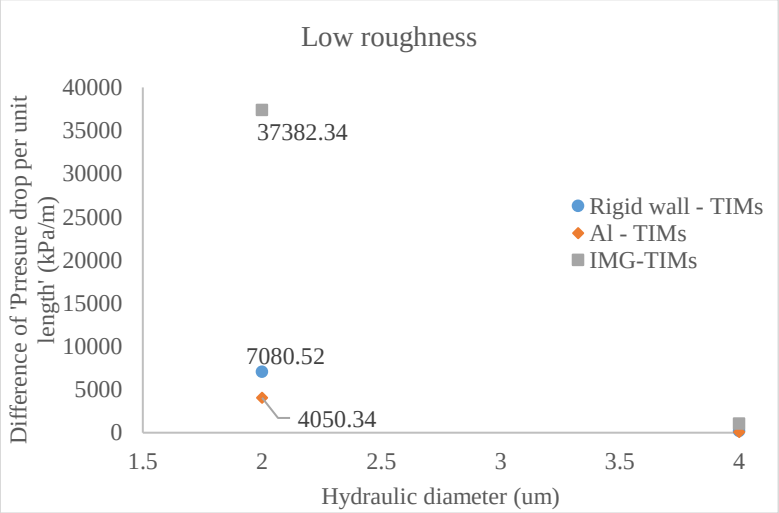


**Figure 43.** Difference of pressure drop per unit length for low roughness (RMS roughness heights = $0.0125\boldsymbol{D_h}$)

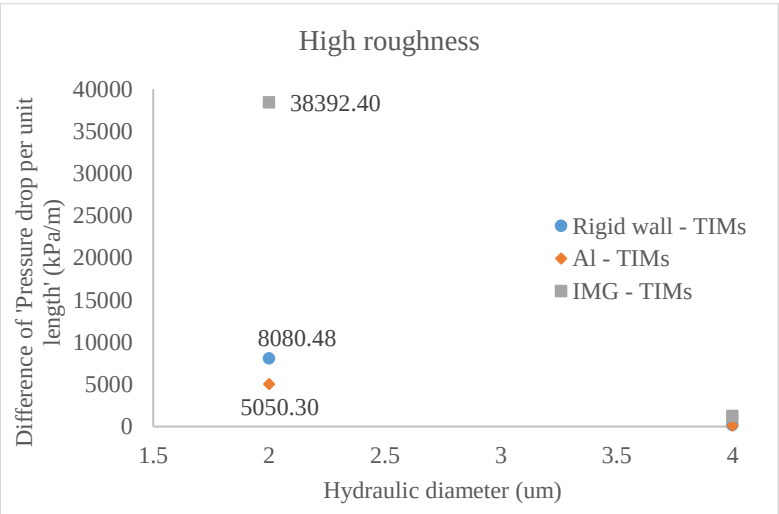


**Figure 44.** Difference of pressure drop per unit length for high roughness (RMS roughness heights = $0.025\boldsymbol{D_h}$)

If the roughness of the channel is introduced, the performance of deformable wall on the reduction of pressure drop is enhanced. High roughness induces more drag forces, which let the fluid suffer high-pressure drop. Figure 45 shows that the drag force becomes large when the roughness increases.

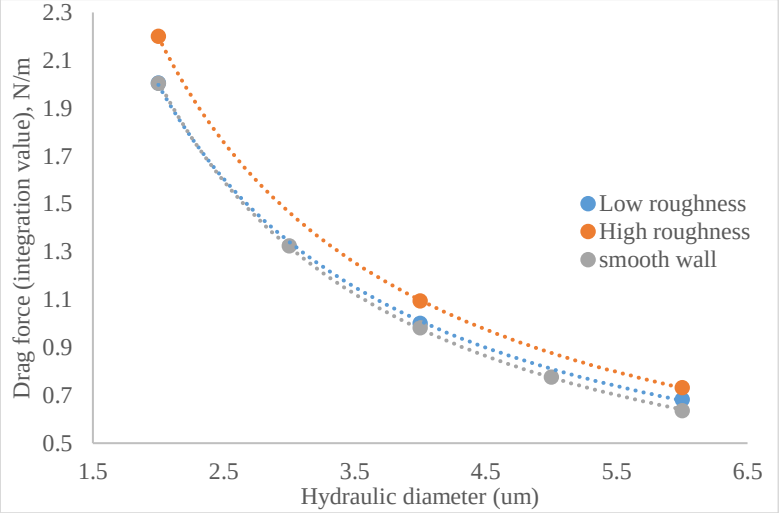


**Figure 45.** Drag force according to the hydraulic diameter for various roughness

In Section 5.2.1, we assume that the pressure drop can be explained by the drag and lift force. If we can decrease these forces by changing the wall properties, we can save the energy loss that fluid suffers when fluid flows through the channel.

The result is not shown in this paper, but the simulation work turns out that the drag and the lift force both decreases when deformable coating applies.

### 5.3 Heat Transfer Observation

It has to be noted that microchannel heat exchanger is preferred due to the high heat transfer achievement. With the deformable wall, heat transfer characteristics in the microchannels are investigated. To investigate the heat transfer in the microchannel, the inward heat flux is applied at the outer boundary of the wall. The heat flux applied to the

outer boundary of the wall is transferred to the fluid. Figure 46, Figure 47, Table 20, Table 21, and Table 22 shows the model setup and the initial condition, respectively. 2D-asymmetric model is used for simulation. The 2D-non-asymmetric model is introduced in Figure 46 and Figure 47 to clarify the model setup and boundary condition.

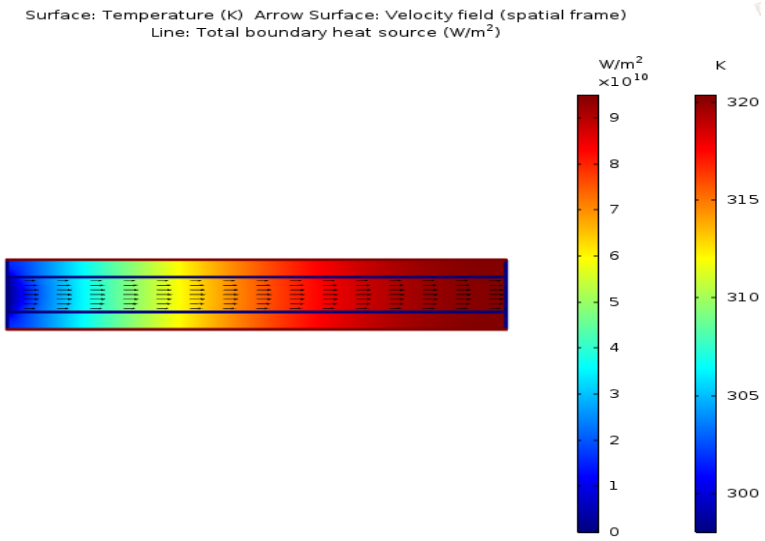


**Figure 46.** Brief illustration of model setup with 2D dimensional model

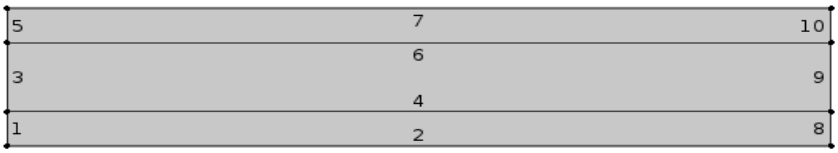


**Figure 47.** Boundary numbering

**Table 20.** Explanation for boundary numbering

| Boundary numbering | Explanation | Notes |
|---|---|---|
| **1, 5, 8, 10** | Coating thickness (Fixed) | - |
| **3** | Fluid inlet | Temperature is fixed to 298K |
| **9** | Fluid outlet | Pressure is fixed to 1bar |
| **4, 6** | Fluid-structure interaction boundary | - |
| **2, 7** | Outer boundary (Fixed) | Heat source |

**Table 21.** Initial condition at wall and fluid domain

| Initial Condition | Temperature (K) |
|---|---|
| **Wall** | 298 |
| **Fluid** | 298 |

**Table 22.** Condition for heat transfer observation

| Condition | Detailed |
|---|---|
| **Outlet pressure** | 1 bar |
| **Inlet velocity profile** | $U_{mean} \times 6 \times (D_h\text{-}r)^2/(D_h)^2$ |
| **Inlet velocity temperature** | 298 K |

The effects of - channel diameter, the length of the channel, the thickness of coating, inlet velocity, and the magnitude of inward heat flux - on heat transfer characteristics are investigated.

We know that there is no pressure drop difference when the wall deformation scale is significantly smaller than the hydraulic diameter ( $\frac{Wall\ deformation}{D_{hydraulic}} \approx 10^{-9}$). Likewise, the difference in heat transfer performance is not detected in this scale according to the types of coating. This is because the wall displacement is so small compared to the hydraulic diameter that wall displacement did not affect the fluid characteristics. Therefore, the author decreases the scale of a channel to investigate the difference of heat transfer performance according to the types of coating.

Since inlet temperature of the fluid is fixed, the outlet temperature of the fluid can be a criterion to determine the heat transfer performance. From Section 5.3.1 to 5.3.5, Outlet temperature ($T_{out}$) and the heat flux magnitude at the boundary of the fluid and deformable coating are observed based on various conditions. Steady-State value is used for analyzation.

### 5.3.1 Effect of Channel Diameter

(Control variable - Hydraulic diameter, Fixed variable - Thickness of coating: 100nm, Channel length: 70um, Inlet velocity: 5m/s, Heat source: 0.95W/mm$^2$).

Figure 48 shows the outlet temperature of the fluid ($T_{out}$) according to the hydraulic diameter at the steady-state condition. It is noticed that $T_{out}$ is increased if the smaller diameter is used. This is the reason why the micro heat exchanger is used; increase the heat transfer per unit volume. Also, it has to be noted that $T_{out}$ is large when the more deformable coating is applied.

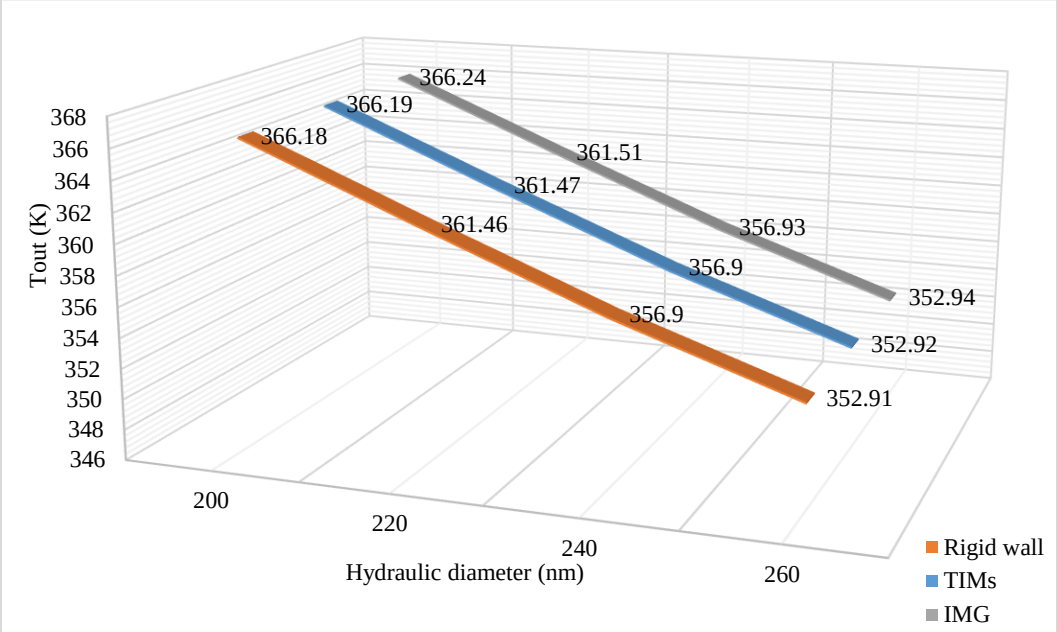


**Figure 48.** Outlet temperature according to hydraulic diameter with different types of wall

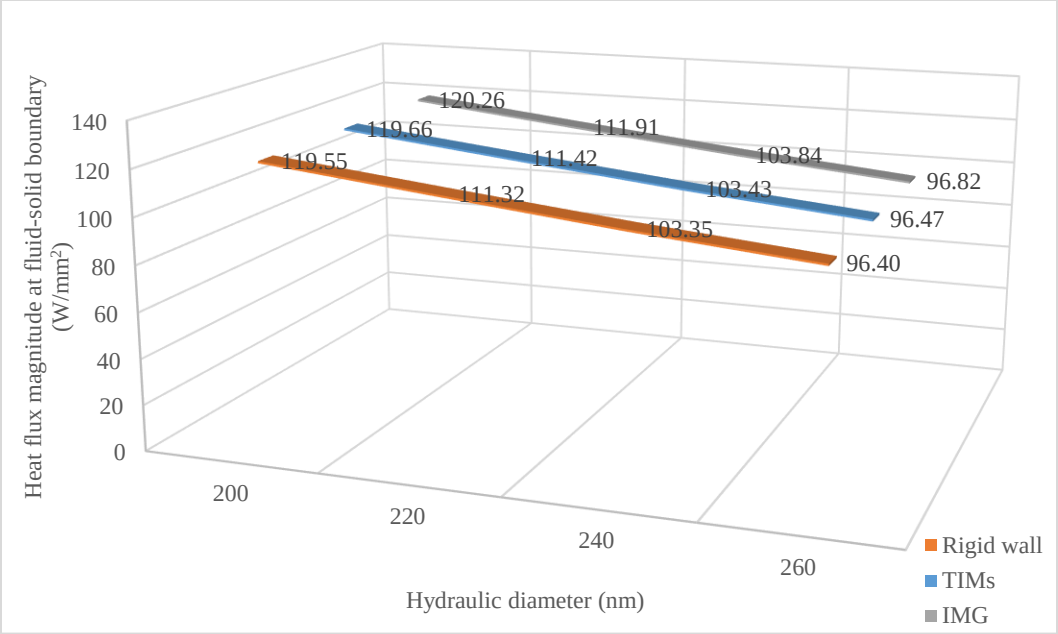


**Figure 49.** Heat flux magnitude at the fluid-solid boundary according to hydraulic diameter with different types of wall

### 5.3.2 Effect of Channel Length

(Control variable - Channel length, Fixed variable - Thickness of coating: 100nm, Channel diameter: 200nm, Inlet velocity: 5m/s, Heat flux from the heat source: 0.95W/mm$^2$)

Figure 50 shows that the $T_{out}$ increases when the channel length of the heat exchanger is long. Longer channel increases the residual time of the fluid along the channel, which makes the fluid absorb more heat from the heat source. This observation also noted that the heat transfer is enhanced when the more deformable coating is applied.

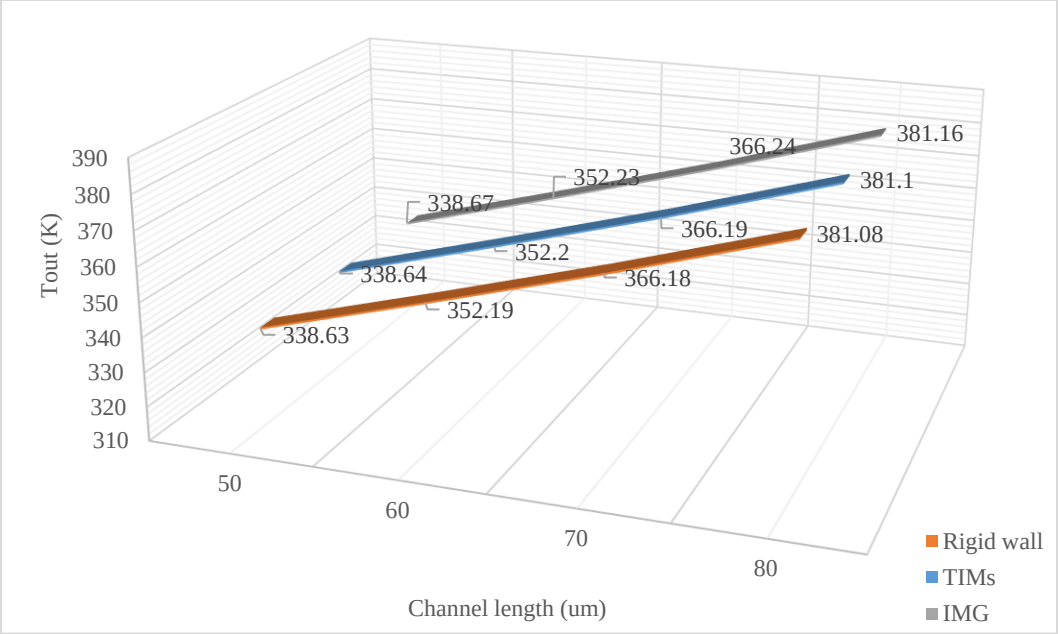


**Figure 50.** Outlet temperature according to channel length with different types of wall

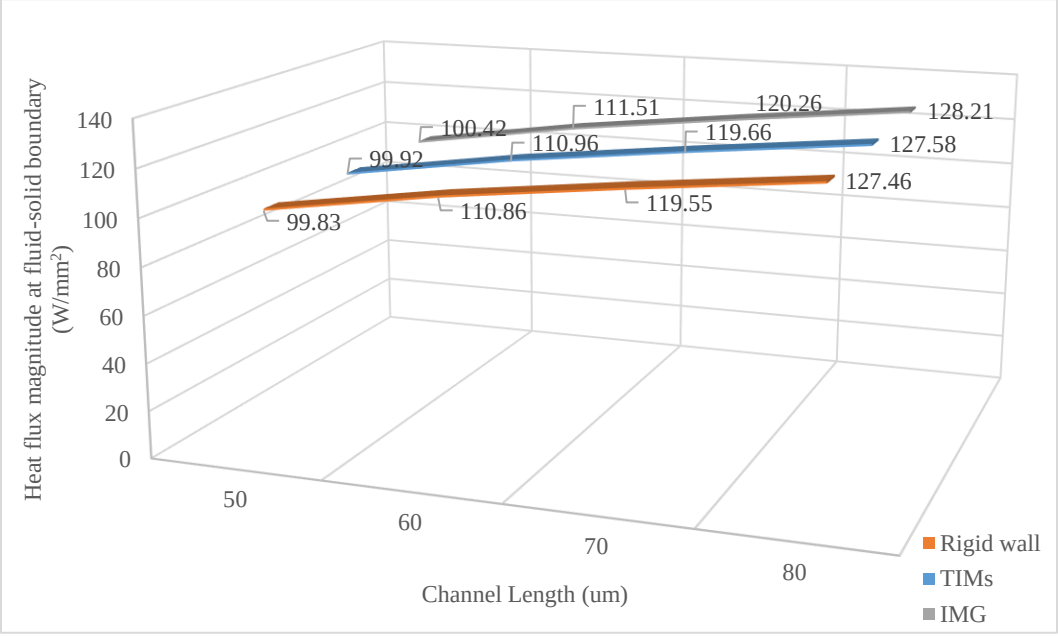


**Figure 51.** Heat flux magnitude at the fluid-solid boundary according to channel length with different types of wall

### 5.3.3 Effect of Thickness of Coating

(Control variable - Thickness of coating, Fixed variable - Channel length: 70um, Channel diameter: 200nm, Inlet velocity: 5m/s, Heat flux from the heat source: 0.95W/mm$^2$)

The heat flux applied to the fluid is reduced when the thickness of coating is increased. Thick coating means more conduction in the solid coating, which takes more time for the heat generated from the heat source to reach to the fluid at the given time. Figure 53 also shows that deformable wall can increase the heat transfer to the fluid.

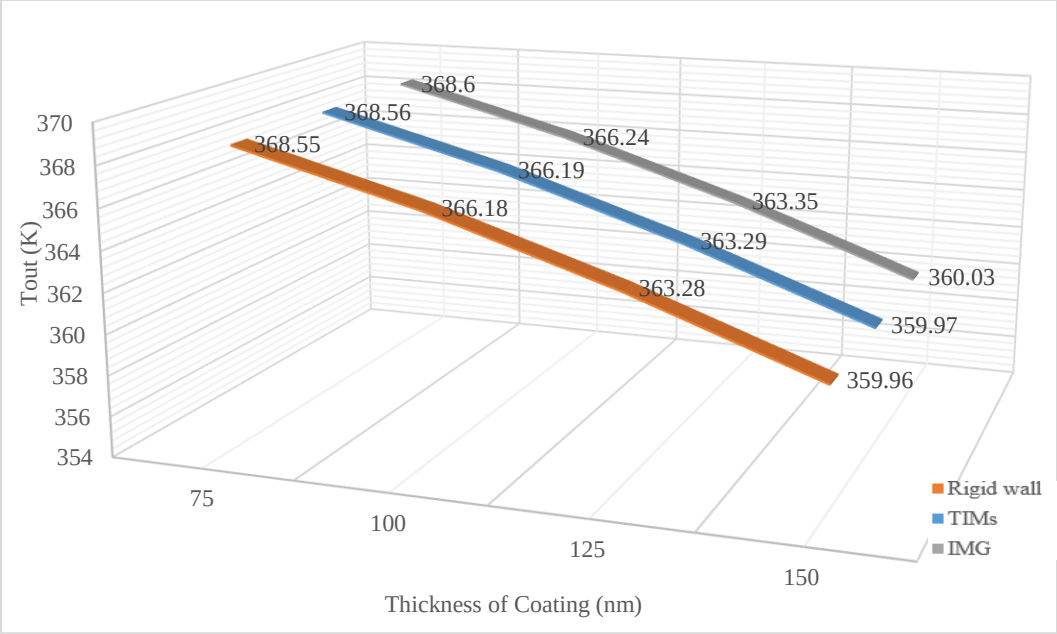


**Figure 52.** Outlet temperature according to thickness of coating with different types of wall

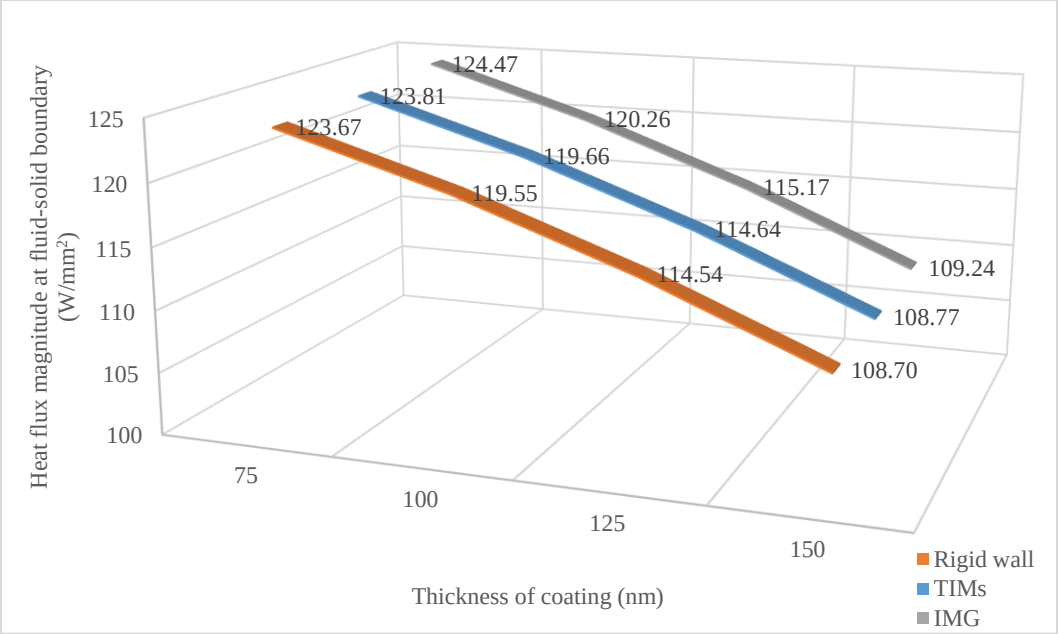


**Figure 53.** Heat flux magnitude at the fluid-solid boundary according to thickness of coating with different types of wall

### 5.3.4 Effect of Inlet Velocity

(Control variable - Inlet velocity, Fixed variable - Channel length: 70um, Channel diameter: 200nm, Thickness of coating: 100nm, Heat flux from the heat source: 0.95W/mm$^2$)

Large inlet velocity reduces the heat exchange time with the heat source, which results in the lower $T_{outlet}$. With the same condition, more deformable wall increase the heat transfer.

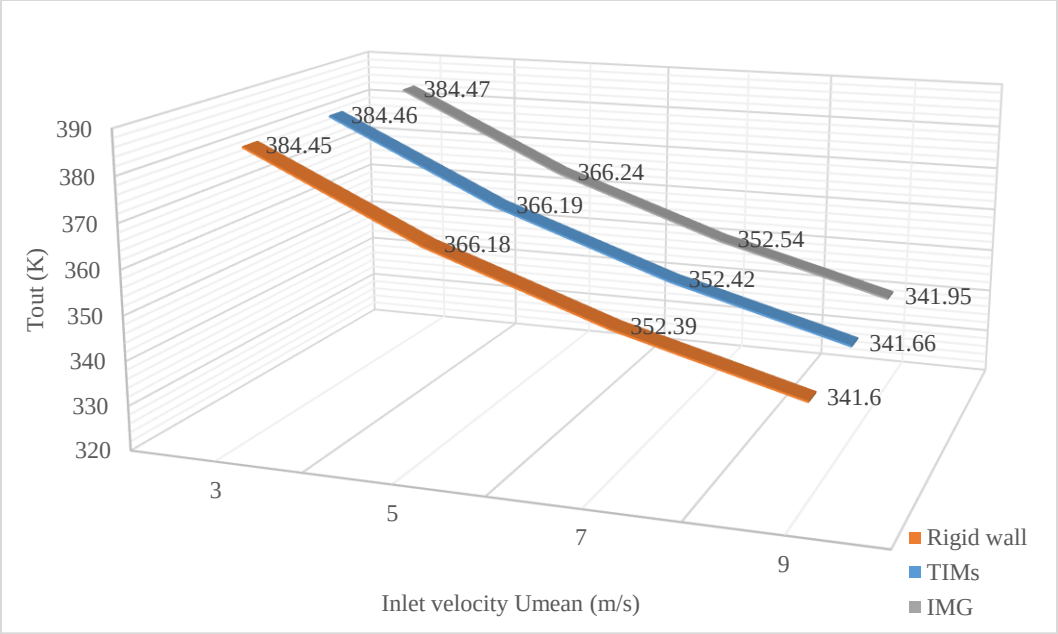


**Figure 54.** Outlet temperature according to inlet velocity with different types of wall

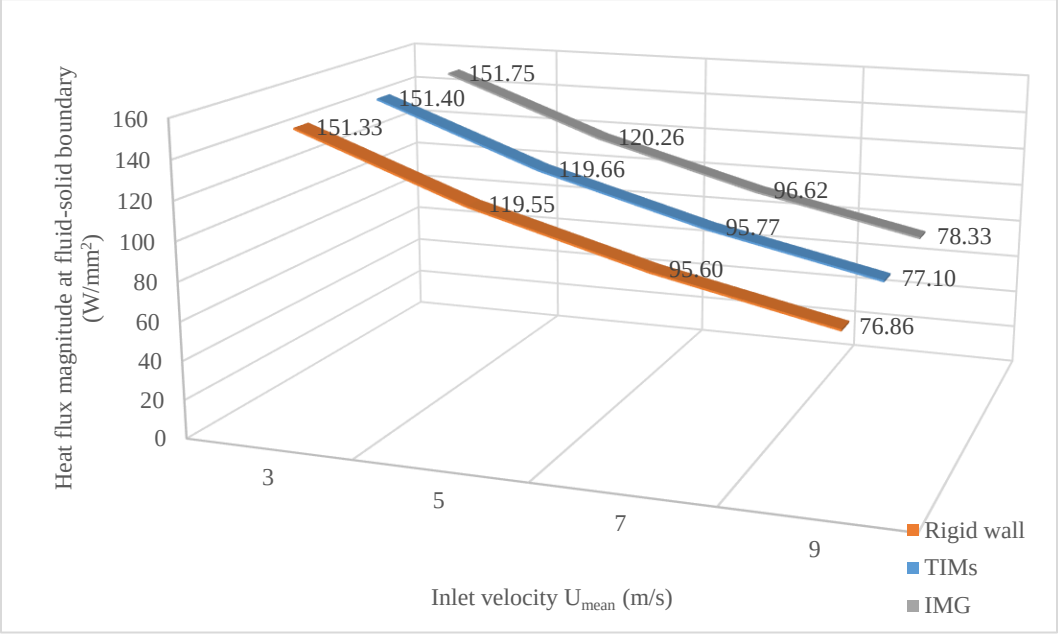


**Figure 55.** Heat flux magnitude at the fluid-solid boundary according to inlet velocity with different types of wall

### 5.3.5 Effect of Magnitude of Heat Flux from the Heat Source

(Control variable - Heat flux from the heat source, Fixed variable - Channel length: 70um, Channel diameter: 200um, Inlet velocity: 5m/s, Thickness of coating: 100nm)

Reasonably, large heat source increases the $T_{out}$. With the investigation of the effect of five variables, it should be noticed that deformable coating can increase the heat transfer.

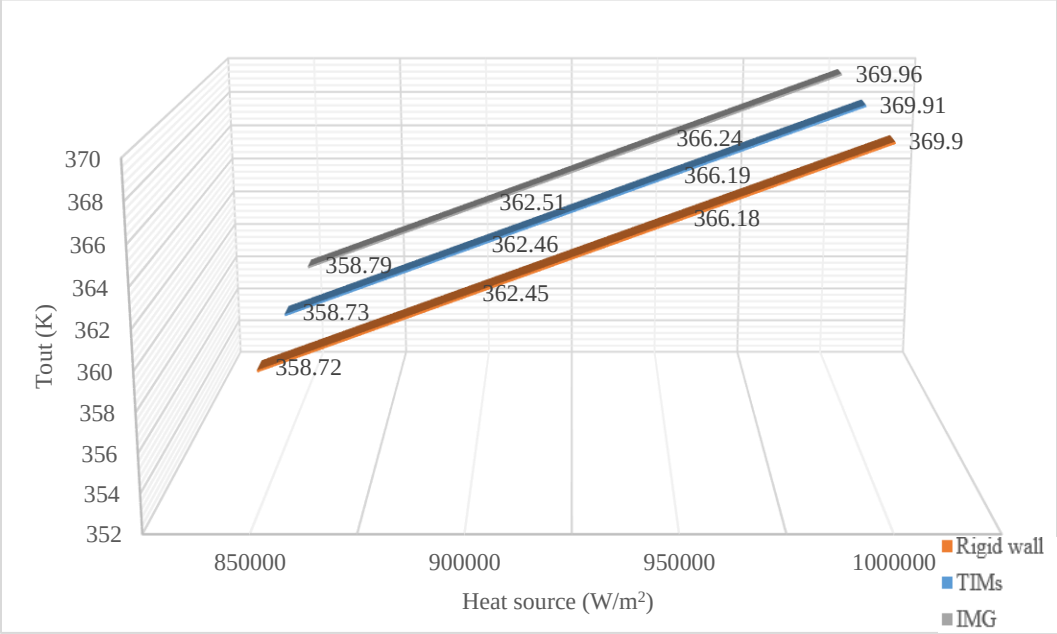


**Figure 56.** Outlet temperature according to heat flux magnitude with different types of wall

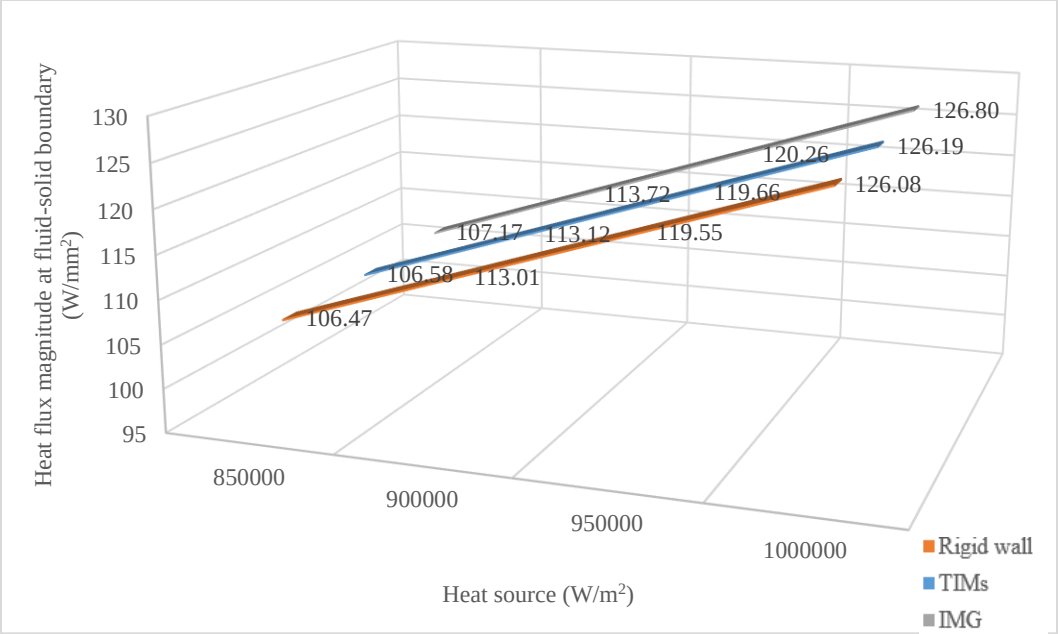


**Figure 57.** Heat flux magnitude at the fluid-solid boundary according to heat flux magnitude with different types of wall

### 5.3.6 Relationship between Heat Transfer and Wall Deformation

The fluid flow deforms the wall, and the deformed wall changes the fluid flow. This deformed wall and the changes of fluid flow affects the heat transfer coefficient. Three components – fluid flow characteristics, deformed wall, heat transfer – are coupled together, affecting each other.

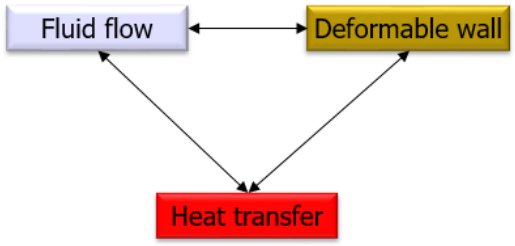


**Figure 58.** Coupled relationship of fluid flow, heat transfer, and deformable wall

Section 5.3.1 to 5.3.5 indicate that the heat transfer performance is enhanced when the wall is more deformable. However, the heat flux at the fluid-solid boundary and the temperature of the fluid is not linear because the channel is deformable. Figure 59 indicates that the temperature of the fluid is not linear through the channel.

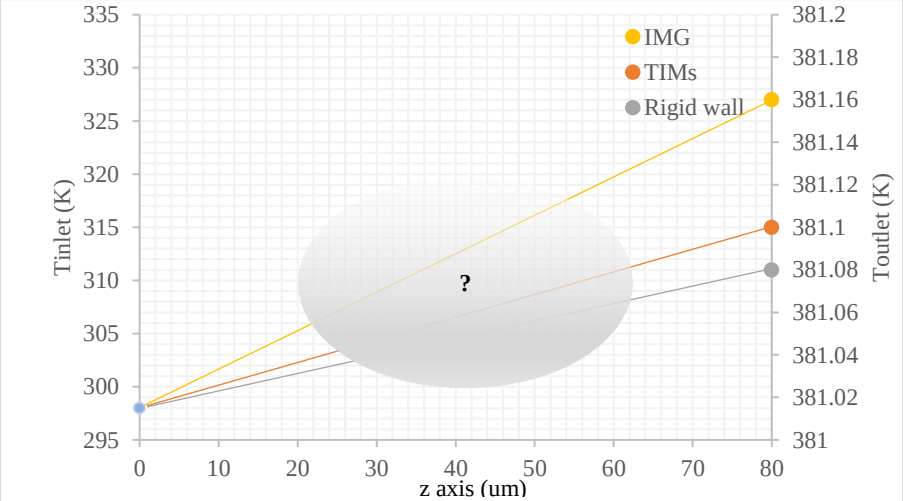


**Figure 59.** Schematic illustration showing the temperature of the wall in the middle

Therefore, it is worth to investigate the wall deformation along the z-axis. To see how deformable wall works under the nanoscale fluid model (that is investigated in the Section 5.3.1-5.3.5), the linear projection method is used for wall deformation and the temperature of the fluid through the channel.

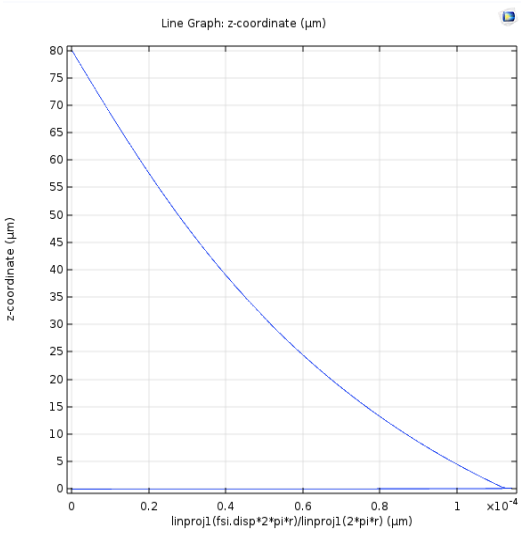


**Figure 60.** Total displacement of the wall along the z-axis at steady-state

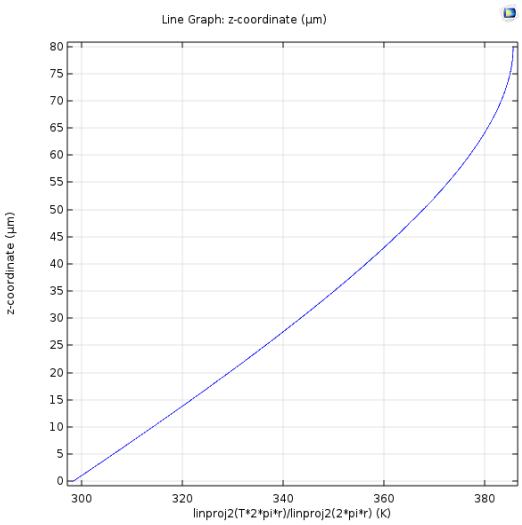


**Figure 61.** Temperature profile of the fluid along the z-axis at steady-state

Figure 60 and Figure 61 is plotted based on the model setup: Channel length: 70um, Channel diameter: 200um, Inlet velocity: 5m/s, Thickness of coating: 100nm, Heat flux from the heat source: 0.95W/mm$^2$. Careful investigation on the graph leads to the conclusion:

1. Change of the wall displacement is high → Change of the temperature of fluid is high
2. Change of the wall displacement is high → Change of the total heat flux magnitude is low

The plot data from COMSOL described in Figure 60 and Figure 61 are exported and plotted together with excel in Figure 62. The slope of each plotted line shows the relationship between the wall displacement and the fluid temperature at the fluid-solid boundary. From the observation, we can know that the 'change' of the temperature of the fluid has a correlation with the 'change' of wall deformation. When we look into the inlet (z-axis ≈ 0 um), the 'change' of wall deformation is high, which leads to the 'large change' of the temperature of the fluid.

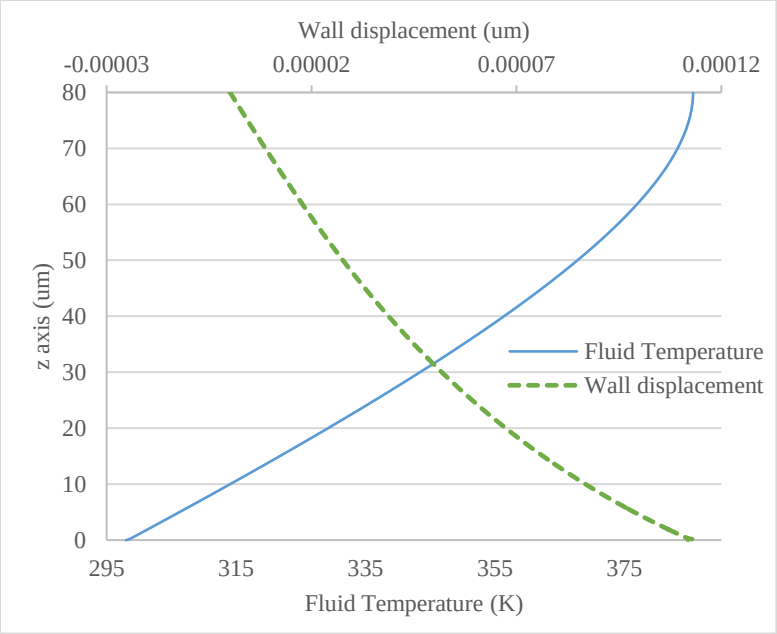


**Figure 62.** Wall displacement and the fluid temperature along the z-axis

This is because large wall deformation at the inlet increases the contact area between the surface and the fluid, and these increased contact areas enhance the heat transfer at the inlet.

The data along the z-axis for each coating is exported from COMSOL and re-plotted in Figure 63 and Figure 64. The graphs use the difference of temperature of the fluid and the wall deformation with the basis of TIMs, respectively (e.g., Temperature of fluid along the z-axis with TIMs coating "minus" Temperature of the fluid along the z-axis with rigid wall). Here, we denote the temperature of the fluid with the TIMs coating, rigid wall, IMG as $T_{fluid\text{-}TIMs}$, $T_{fluid\text{-}rigid}$, $T_{fluid\text{-}IMG}$, respectively. Similarly, the total wall deformation with the TIMs coating, rigid wall, IMG is denoted as $WD_{TIMs}$, $WD_{rigid}$, $WD_{IMG}$, respectively.

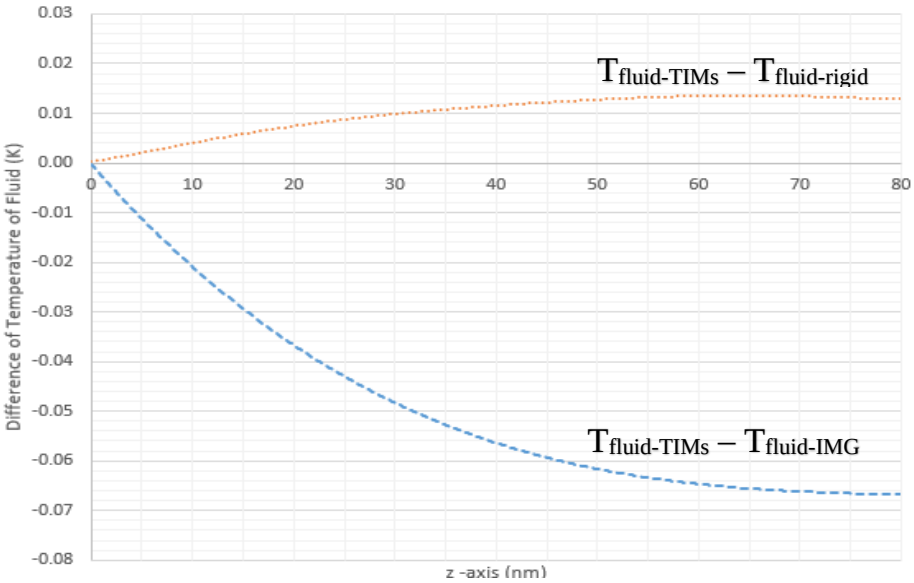


**Figure 63.** Difference of temperature of fluid along the z-axis

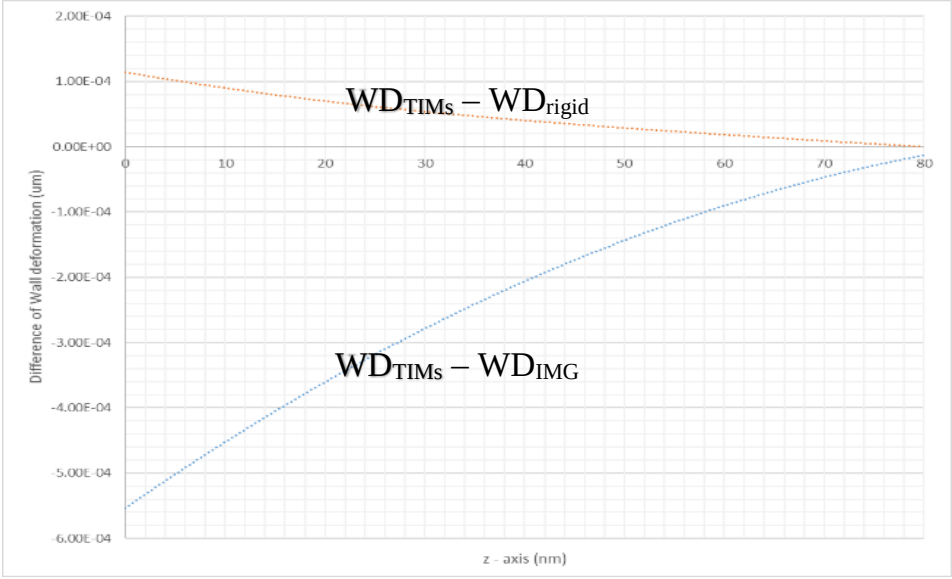


**Figure 64.** Difference of deformation of wall along the z-axis

Figure 63 and Figure 64 show that the ‘rate’ of increase of temperature of the fluid is high when the ‘rate’ of deformation of the wall is large.

### 5.3.7 Heat Loss Measurement

The heat flux applied at the outer boundary of the coating is transferred to the fluid. The energy that is not transferred to the fluid from the heat source is calculated by:

$$Q_{loss} = V \cdot I - \dot{m}(h_0 - h_i) \qquad eq.(27)$$

Where $V \cdot I$ refers to the heat flux from the heat source, $\dot{m}(h_0 - h_i)$ refers to the increase in enthalpy of the fluid. Since outer boundary of the wall is insulated, $Q_{loss}$ is equal to the heat absorbed by the fluid.

The increase in enthalpy of the fluid can be calculated by applying the thermodynamic concepts.

$$\mathrm{dH} = C_p dT + \left[V - T\left(\frac{\partial V}{\partial T}\right)_P\right] dP \qquad eq.(28)$$

This equation can be reduced for liquids:

$$\mathrm{dH} = C_p dT + (1 - \beta T) V dP \qquad eq.(29)$$

Because we assume that the fluid is incompressible,

$$\beta = \frac{1}{V}\left(\frac{\partial V}{\partial T}\right)_P = 0 \qquad eq.(30)$$

The equation 28 reduces to,

$$\Delta\mathrm{H} = C_p \Delta T + V dP \qquad eq.(31)$$

Enthalpy is state-functions, and the integration path is arbitrary. Since $C_p$ is a weak function of T while the V is weak functions of P, arithmetic means are satisfactory for integration. The path chosen is shown in Figure 65.

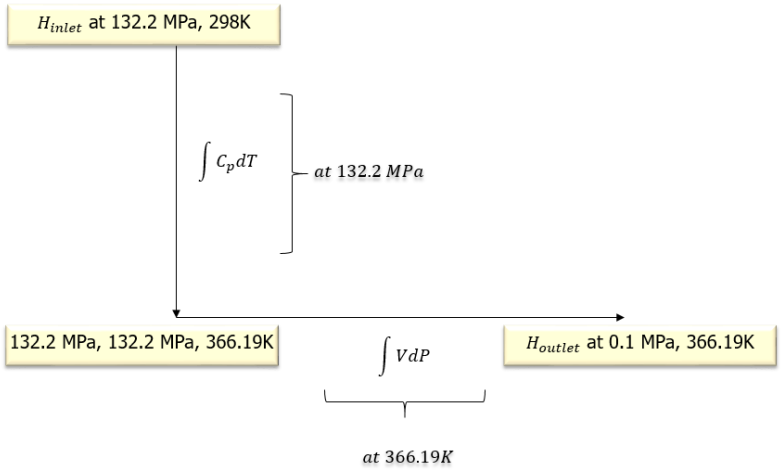


**Figure 65.** Calculation path for enthalpy change between the inlet and the outlet

Figure 65 shows the enthalpy change when the fluid goes inlet with the condition of 132.2 MPa, 298K and comes out at the outlet with 0.1 MPa, 366.19K.

**Table 23.** Data for enthalpy change

| | t/K | P/MPa | $\boldsymbol{C_p/Jkg^{-1}K^{-1}}$ | V/$\boldsymbol{cm^3mol^{-1}}$ |
|---|---|---|---|---|
| $\boldsymbol{H_{inlet}}$ | 298 | 132.2 | 4182.850 | |
| | 298 | 0.1 | - | |
| | 366.19 | 132.2 | 4209.098 | 17.781 |
| $\boldsymbol{H_{outlet}}$ | 366.19 | 0.1 | - | 17.962 |

$$\Delta H = < C_p > \Delta T + < V > dP \qquad eq.(32)$$

For P = 132.2 MPa,

$$< C_p > = \frac{4182.850 + 4209.098}{2} = 4195.97 \text{Jkg}^{-1}\text{K}^{-1}$$

For t = 366.19 K,

$$< \mathrm{V} > = \frac{17.781 + 17.962}{2} = 17.87 \mathrm{cm}^3 \mathrm{mol}^{-1}$$

Therefore, the enthalpy change is,

$$\Delta \mathrm{H} = 4195.97(366.19 - 298) + \frac{17.87(0.1 - 132.2) \times 10^6}{\left(\frac{cm}{0.01m}\right)^3} = 283763 \frac{\mathrm{J}}{\mathrm{kg}}$$

Heat loss is,

$$\mathrm{Q_{loss}} = \mathrm{V} \cdot \mathrm{I} - \dot{\mathrm{m}}(\mathrm{h_0} - \mathrm{h_i}) = 8.357\mathrm{E}^{-05}\ \mathrm{W} - \ 1.57\mathrm{E}^{-10} \frac{\mathrm{kg}}{\mathrm{s}} \times 283763 \frac{\mathrm{J}}{\mathrm{kg}}$$

$$= \ 3.902\mathrm{E}^{-05}\mathrm{W}$$

$V \cdot I$ is calculated by surface area of the heat source×heat flux, and the mass flow rate is observed with boundary probe of COMSOL.

$$\mathrm{Q_{loss}}(\%) = \frac{\text{heat not absorbed by the fluid}}{\text{heat flux generated from the heat source}} = \frac{\mathrm{V} \cdot \mathrm{I} - \dot{\mathrm{m}}(\mathrm{h_0} - \mathrm{h_i})}{\mathrm{V} \cdot \mathrm{I}}$$

$$= \frac{3.902\mathrm{E}^{-05}}{8.357\mathrm{E}^{-05}} \times 100 = 46.7\ (\%)$$

Heat loss data with various conditions is obtained in Figure 67, Figure 68, Figure 69, and Figure 70. The piecewise function for $C_p$ from COMSOL is used for calculation, and isothermal data for V is obtained (E.W. Lemmon et al, 2017).

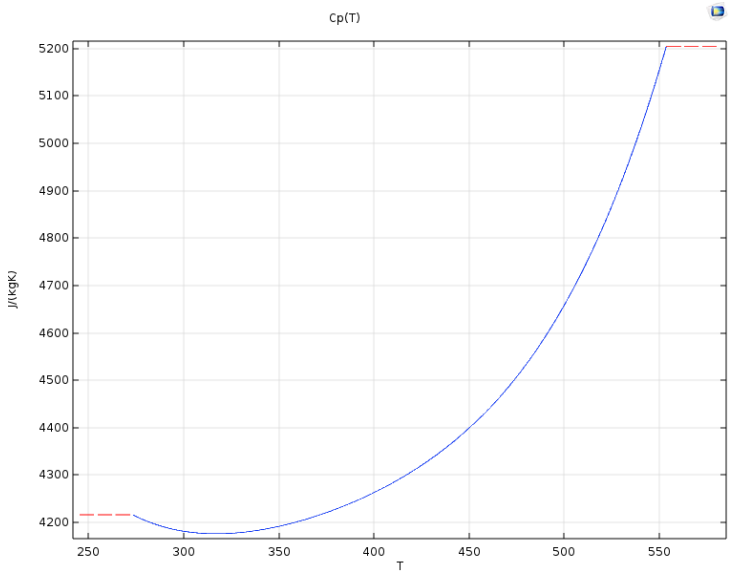


**Figure 66.** Piecewise function for Cp plotted with COMSOL 5.3

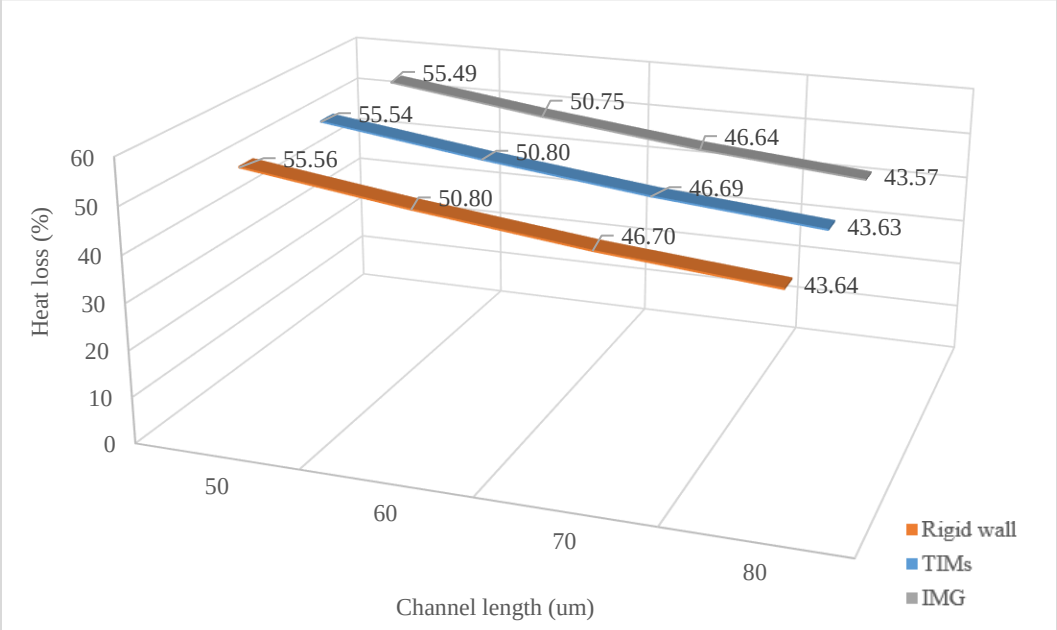


**Figure 67.** Heat loss (%) according to channel length

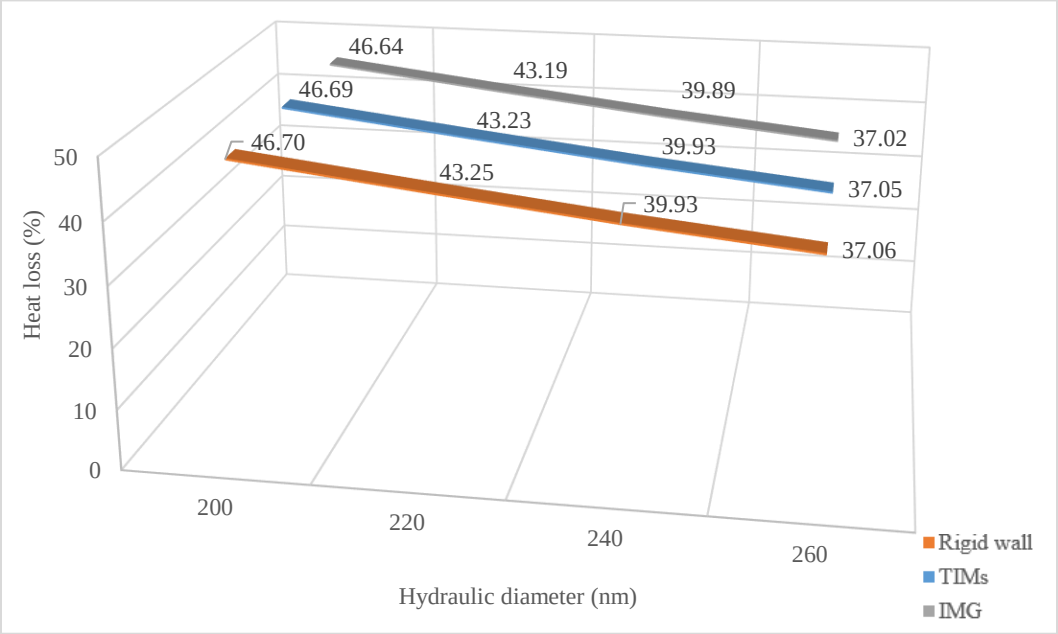


**Figure 68.** Heat loss (%) according to hydraulic diameter

Figure 67 and Figure 68 shows that the heat loss (%) is large (more heat is absorbed by the solid) when the hydraulic diameter and the channel length is small. The ratio of heat absorbed by the fluid to original heat flux is depicted in Figure 69 and Figure 70. As we observed before, deformable wall shows better performance for heat transfer.

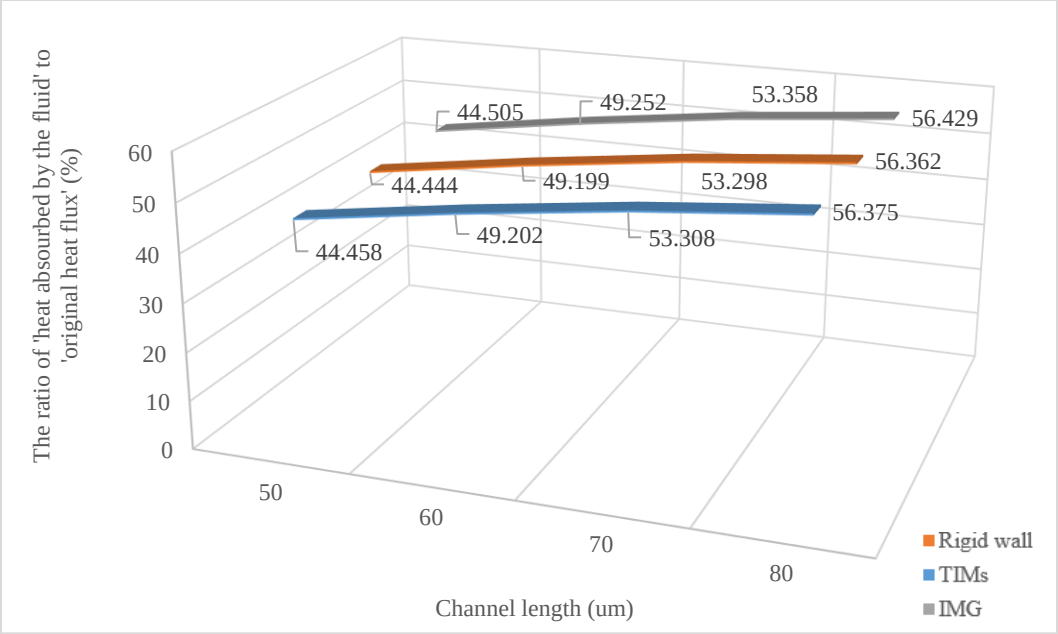


**Figure 69.** Heat absorbed by the fluid (%) according to channel length

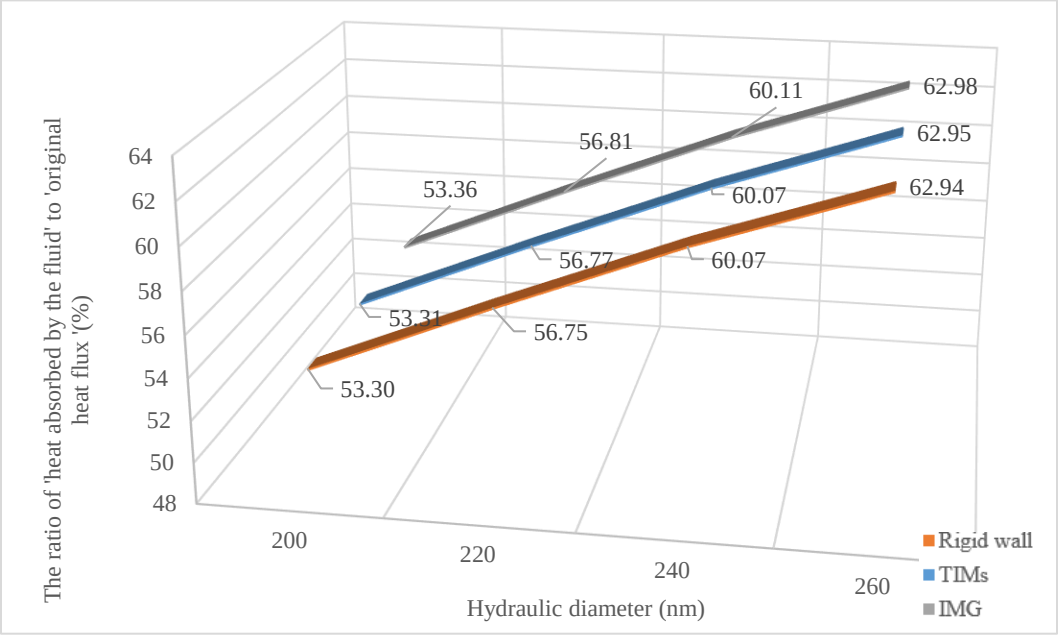


**Figure 70.** Heat absorbed by the fluid (%) according to hydraulic diameter

Figure 71 shows the ratio of heat absorbed by the fluid to original heat flux according to the wall deformation when different Reynolds number is applied.

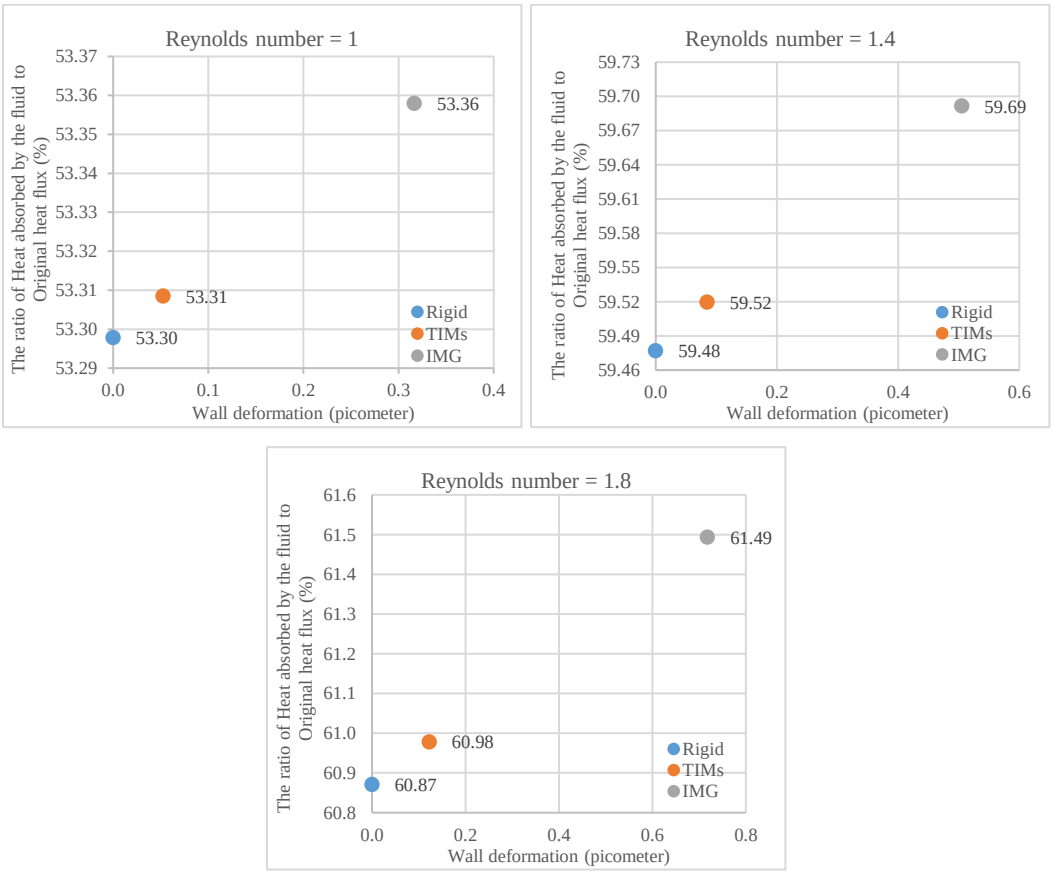


**Figure 71.** Heat absorbed by the fluid (%) with different Reynolds number

Deformable wall increases the wall deformation, increasing the heat absorption by the fluid. It has to be noted that increased surface area for heat transfer enhances the heat transfer rate.

Also, the fluid absorbs more heat with high Reynolds number. Although the high velocity or high Reynolds number reduces the outlet temperature of the fluid as shown in Figure 72 (heat absorbed per unit mass), the high mass flow rate can increase the overall heat transfer (W) from the heat source.

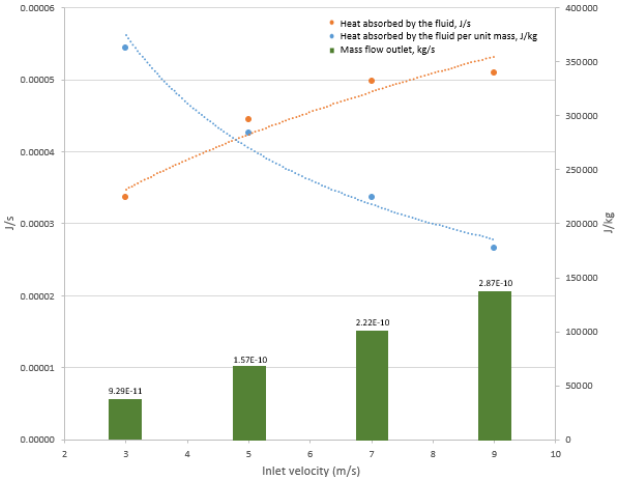


**Figure 72.** The relationship between heat absorbed by the fluid and mass flow outlet

Figure 73 shows the combination of Figure 71. It indicates that the heat absorbed by the fluid increases when the wall deformation and the Reynolds number increases. Since the only difference between the rigid wall, IMG, and the TIMs in this paper is the 'Deformable' performance, we can conclude that the deformable coating can increase the heat transfer.

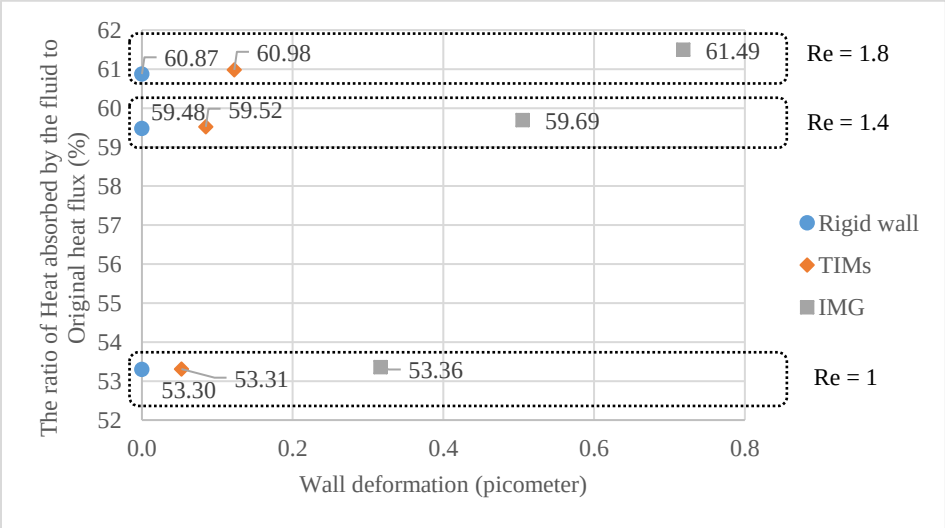


**Figure 73.** Heat absorbed by the fluid (%) with different types of wall and Reynolds number

Figure 74 incorporates the Aluminum to Figure 73 with the same condition (e.g., when Reynolds number is 1.8, heat absorbed by the fluid is 61.40%). The Aluminum shows better performance in heat transfer than other three materials because of different heat transfer properties.

However, it does not indicate that Aluminum shows the better performance on heat transfer because this paper assumes that the outer boundary of the coating is fixed. If the Aluminum is incorporated in large volume, the assumption that only the coating part will move does not reflect the reality. The thicker the Aluminum heat exchanger is, the lower the movement of the Aluminum may happen.

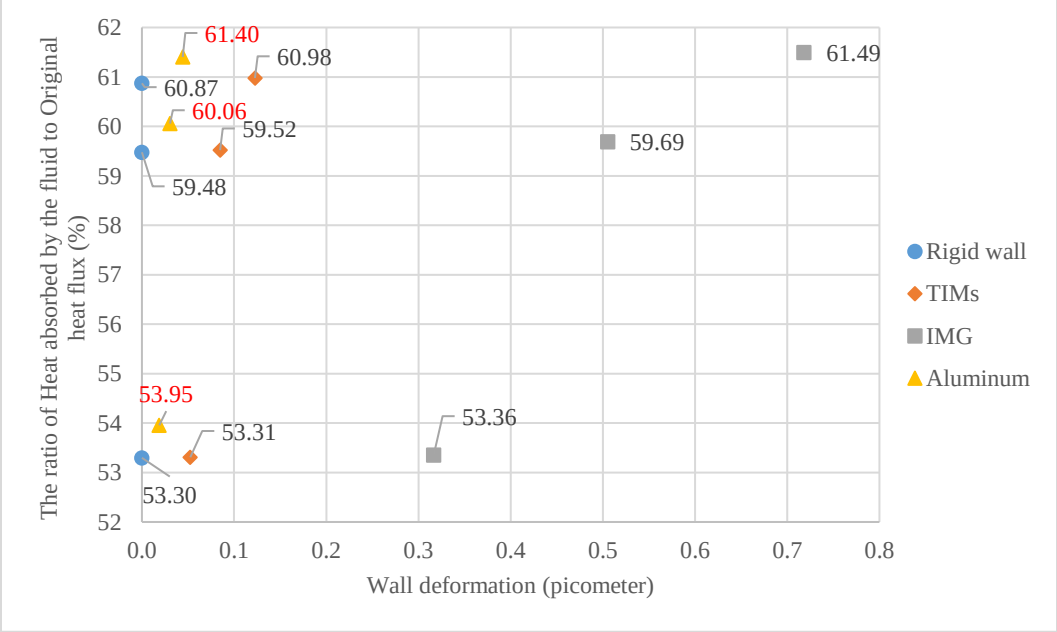


**Figure 74.** Heat absorbed by the fluid (%) with different types of wall and Reynolds number

### 5.3.8 Convective Heat Flux and Temperature of the Wall

Convective heat flux is a flux induced by the temperature difference between the adjacent fluid and the body. Convective heat flux according to the types of wall is

investigated in this paper. Table 24 shows the model dimension discussed for the investigation of the convective heat flux.

**Table 24.** Model dimension used for investigating the convective heat flux

| Model dimension | Value | Unit |
|---|---|---|
| **Channel radius** | 200 | nm |
| **Coating thickness** | 100 | nm |
| **Channel length** | 1 | um |
| **Inlet velocity** | 5 | m/s |
| **Boundary heat source** | $0.95\times10^{6}$ | $W/m^2$ |
| **Reynolds number** | 0.996 | - |

Figure 75 shows the convective heat flux at the fluid-solid boundary along the axial direction. Sudden rise occurs near the inlet, which is the similar trends with the wall deformation. Figure 76 shows the temperature distribution of the wall and the fluid along the axial direction. Since the heat flux is applied at the outer boundary of coating, the wall temperature is higher than the fluid temperature, which makes a temperature gradient from the solid to fluid.

From Figure 60, Figure 61, and Figure 62, we know that the temperature gradient is large when the wall deformation is large.

$$\text{Wall deformation rate} \propto \text{Temperature gradient}$$

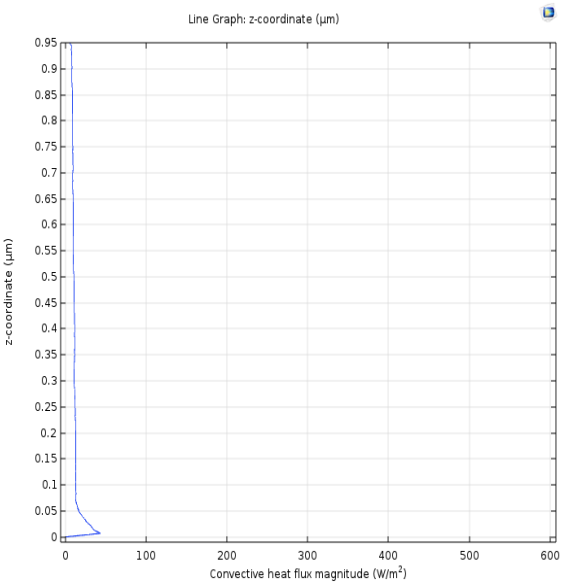


**Figure 75.** Convective heat flux magnitude along the z-axis

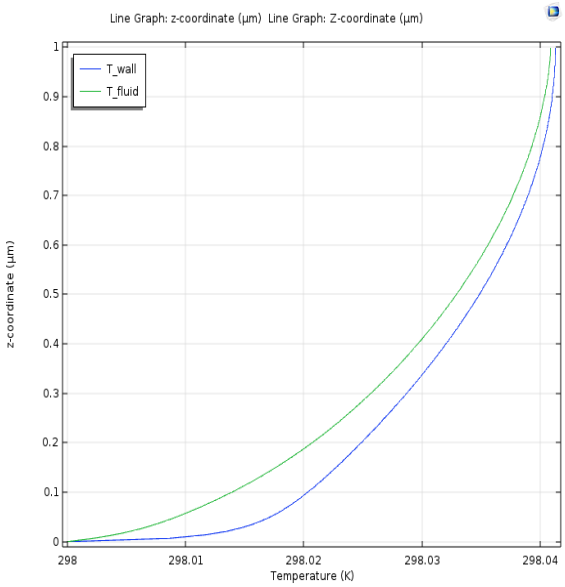


**Figure 76.** Temperature distribution of the fluid and the wall along the z-axis

If the temperature gradient is related to the convective heat flux magnitude, wall deformation is also coupled with the convective heat flux. From the investigation of convective heat flux with different types of coating, the convective heat flux largely varies at the point close to the inlet. In this paper, the point where convective heat flux is maximum is denoted as $z_{maxheatflux}$ (In Figure 75, this point is the 0.006994 µm away from the inlet, which is 7% of the microchannel length), and assumes that the convective heat transfer performance is determined by the convective heat flux at $z_{maxheatflux}$.

Figure 77 and Figure 78 is the magnified graph of Figure 75 and Figure 76 around the point, $z_{maxheatflux}$, respectively. The temperature of the wall changes abruptly at $z_{maxheatflux}$. This is because convective heat flux is maximized when the difference of temperature of the fluid and the wall is maximum. Convective heat flux is described by the following equation:

$$\text{Convective heat flux} = h_c \times (T_w - T_f)$$

Where $h_c$ is the convective heat transfer coefficient, $T_w$ is the temperature of the wall, and $T_f$ is the temperature of the fluid.

However, convective heat transfer coefficient is also a variable depending on the surface temperature and the surface shape. Therefore, it is worth to determine whether convective heat transfer coefficient is also maximized at $z_{maxheatflux}$.

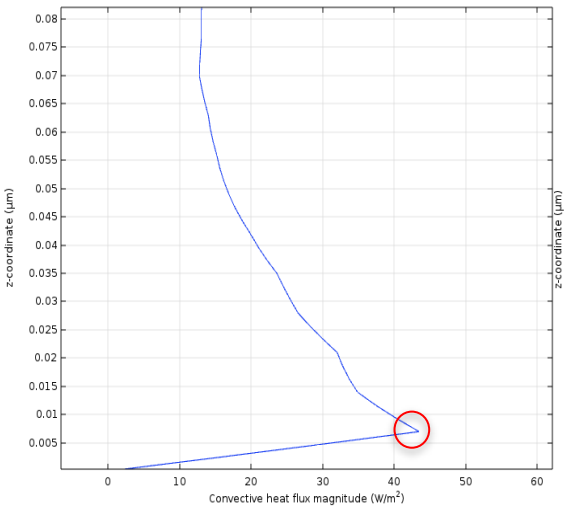


**Figure 77.** Convective heat flux magnitude along the z-axis (Magnified)

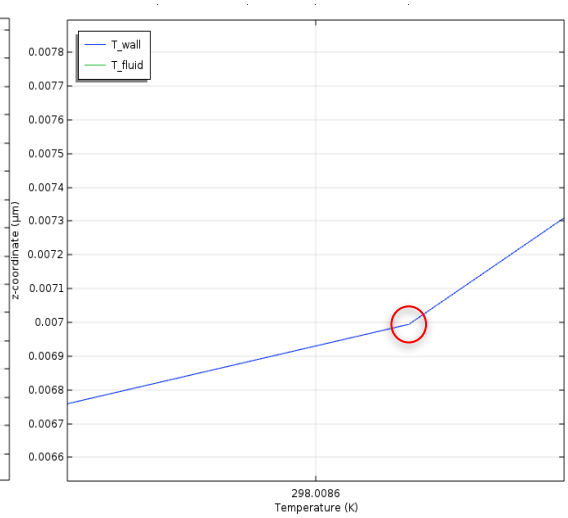


**Figure 78.** Temperature distribution of the fluid and the wall along the z-axis (Magnified)

Local convective heat transfer coefficient and the average heat transfer coefficient is calculated and plotted in Figure 79 and Figure 80. At the legend in Figure 79 and Figure 80, $h_x$ denotes the local convective heat transfer coefficient at $z_{maxheatflux}$, while $h_{avg}$ denotes the average convective heat transfer coefficient over a microchannel. For the average convective heat transfer coefficient, ten points along the pipe length are selected with the same interval, and the average value is obtained. Three aspects need to be discussed with this graph:

1. Convective heat transfer coefficient increases as the $z_{maxheatflux}$ becomes small.
2. Deformable walls increase the convective heat transfer coefficient.

3. Local heat transfer coefficient is larger than the average heat transfer coefficient because of the large heat flux at $z_{maxheatflux}$. That is, the variance of heat flux at $z_{maxheatflux}$ may dominate the overall convective heat transfer performance according to the types of wall, and the convective heat flux at $z_{maxheatflux}$ can be criteria to determine the overall heat transfer performance according to the types of wall.

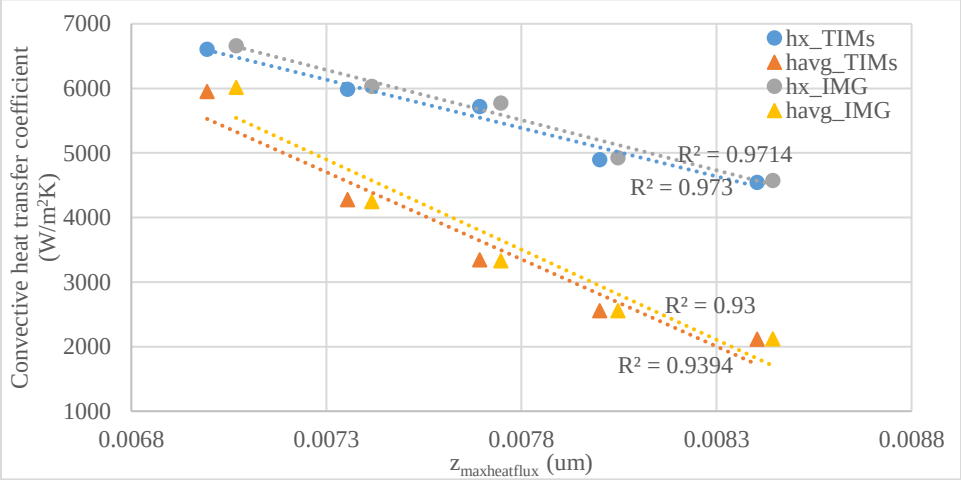


**Figure 79.** Convective heat transfer coefficient according to the dimension of $z_{maxheatflux}$

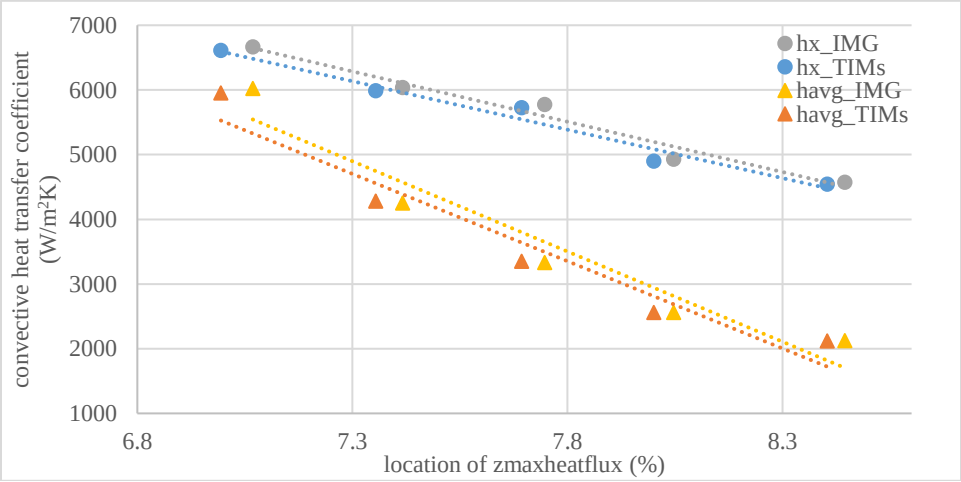


**Figure 80.** Convective heat transfer coefficient according to the location of $z_{maxheatflux}$

Figure 81 shows that small $z_{maxheatflux}$ increase the temperature difference between the wall and the fluid, which enhances the convective heat flux. Figure 82 shows that $z_{maxheatflux}$ decreases as the hydraulic diameter become small. We already know that the convective heat transfer is enhanced when we use smaller channel dimension, by increasing the heat transfer surface area per unit volume. This fact is verified with the introduced variable, $z_{maxheatflux}$, in that low $z_{maxheatflux}$ increases the convective heat transfer.

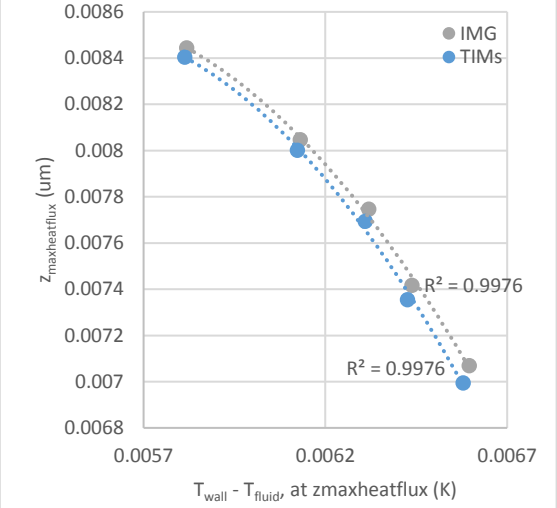


**Figure 81.** $z_{maxheatflux}$ versus $T_{wall}$ - $T_{fluid}$ for IMG and TIMs

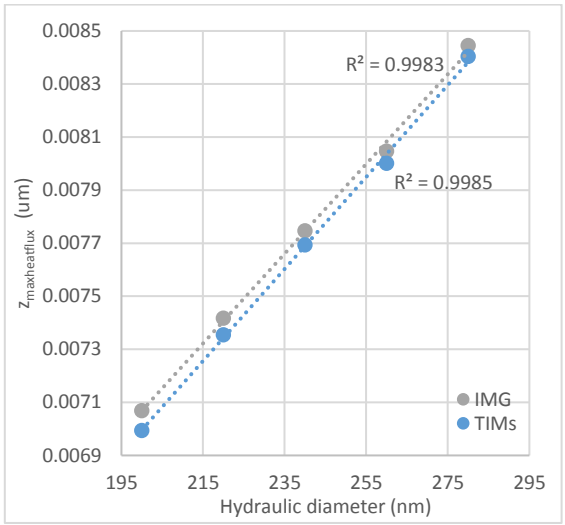


**Figure 82.** $z_{maxheatflux}$ according to hydraulic diameter

Until now, we know that

$$z_{maxheatflux} \propto \frac{1}{Convective\ heat\ flux}$$

Low $z_{maxheatflux}$ increases the convective heat transfer performance, and the amount of wall deformation determines the $z_{maxheatflux}$. Figure 83 shows that the $z_{maxheatflux}$ decreases when the average wall deformation increases.

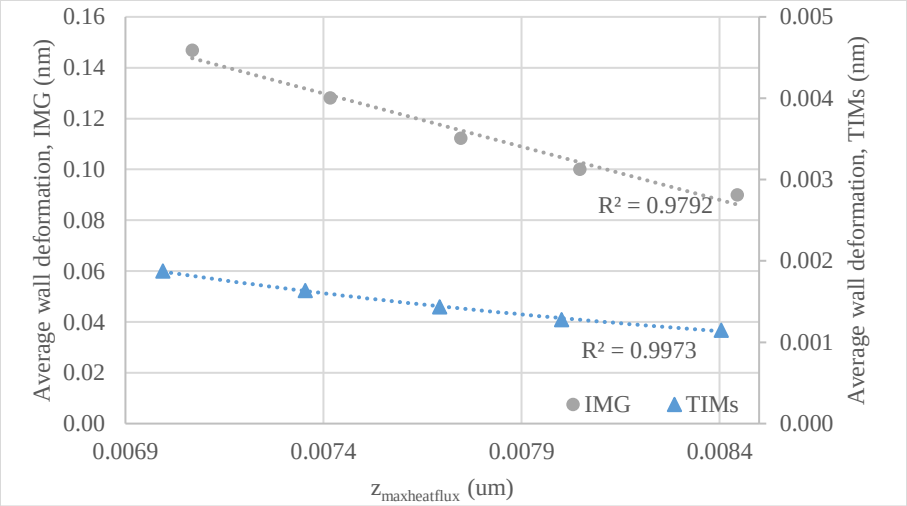


**Figure 83.** Wall deformation according to $z_{maxheatflux}$

### 5.3.9 Convective Heat Flux and Hydraulic Diameter

Nusselt Number (Nu) is often discussed in heat transfer at a boundary within a fluid:

$$Nu = \frac{Convective\ heat\ transfer}{Conductive\ heat\ transfer} = \frac{hL}{k}$$

Where h is the convective heat transfer coefficient, L is the characteristic length, k is the thermal conductivity of the fluid.

For fully developed internal laminar flow, the Nusselt numbers are constant-valued. Therefore, the inverse relationship between the convective heat transfer coefficient and the characteristic length is derived:

$$h \propto \frac{1}{L}$$

A correlation between the convective heat transfer coefficient and the characteristic length L (In circular channel, characteristic length is the hydraulic diameter) can be obtained for different types of coating. Figure 84 and Figure 85 show the local

convective heat transfer coefficient according to the hydraulic diameter for various types of coating. They show that deformable wall has large local convective heat transfer coefficient, satisfying the inverse relationship between the convective heat transfer coefficient and the characteristic length.

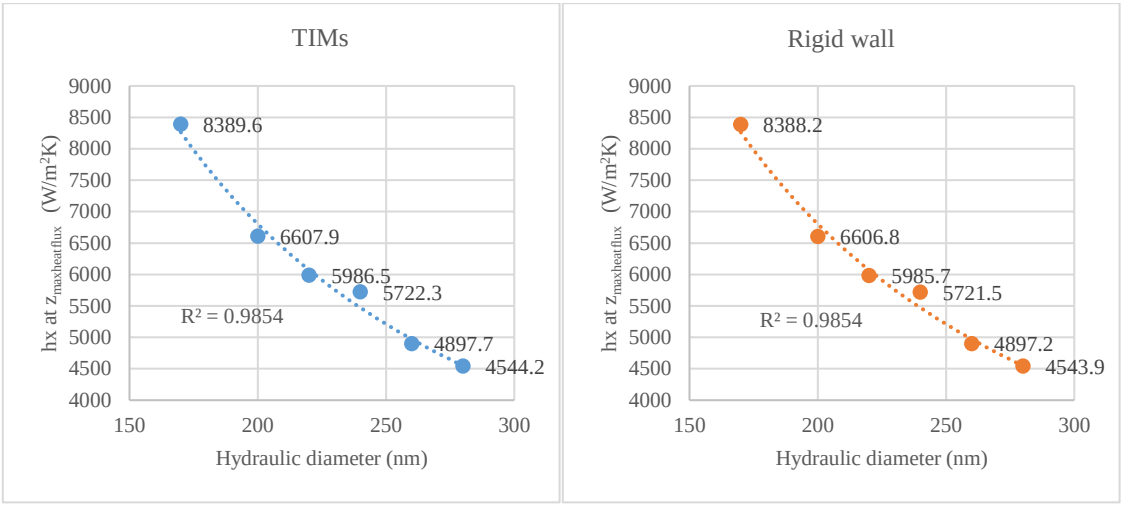


**Figure 84.** The relationship between $h_x$ at $z_{maxheatflux}$ according to hydraulic diameter for TIMs and Rigid wall

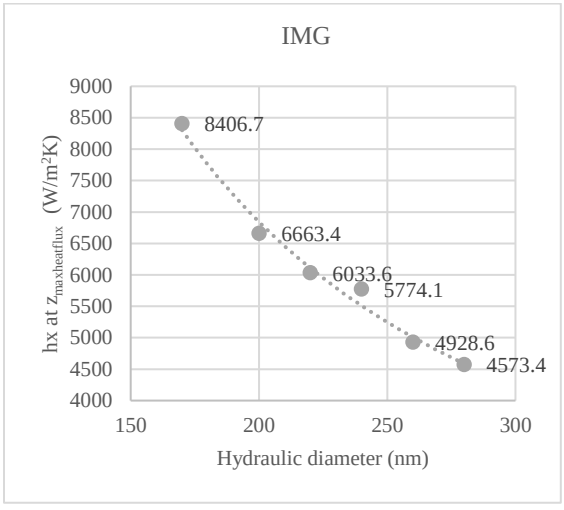


**Figure 85.** The relationship between $h_x$ at $z_{maxheatflux}$ according to hydraulic diameter for IMG

$z_{maxheatflux}$ is a location that makes a difference in heat transfer performance according to the types of coating. Based on what we investigated, we can summarize the trends of $z_{maxheatflux}$.

1. $z_{maxheatflux}$ is the location of the fluid-wall boundary where the convective heat flux is maximum; this value is related to the wall deformation and heat transfer performance.
2. $z_{maxheatflux}$ is inverse proportional to the convective heat transfer coefficient.
3. More wall deformation decreases the $z_{maxheatflux}$.
4. Deformable wall can increase the convective heat transfer.

# 6. SUMMARY AND CONCLUSIONS

## 6.1 Summary

Pressure drop and heat transfer performance of a circular microchannel with the deformable coating are investigated when the fully developed laminar flow is introduced. The investigation of pressure drop and heat transfer performance is conducted by changing the hydraulic diameter, inlet velocity, channel length, and the thickness of the coating. The shape of deformable coating with the various fluid condition is introduced, and the computed data proves that the deformed shape of the coating reduces the pressure drop along the channel and increases the heat transfer performance by increasing the surface area.

• With simulation, TIMs shows potential to reduce the pressure drop and increase the heat transfer with a scale of $\frac{Wall\ deformation}{D_{hydraulic}} \approx 10^{-5}$.

• Deformable properties can increase the heat transfer by changing the shape of the wall.

• TIMs, with high thermal conductivity and deformable wall, is regarded as promising materials to be applied in novel microchannel heat exchanger.

## 6.2 Conclusions

In our lives, heat exchanger operations are significantly involved in extensive fields ranged from micro level high-tech applications to the large-scale industrial plants. However, the current heat exchanger has been suffering from four fundamental problems: pressure drop, clogging, corrosion, and fouling. These problems not only cause significant production loss and increased maintenance costs in large-scale operations but also hinder the transition from prototype to the product in many high-tech applications. Moreover, a rapid development of micro driven devices calls for further studies and experiments to improve high-performance micro heat exchanger operations. With the synergistic combination of highly thermally conductive and mechanically compliant properties of

hybrid nanocomposite materials, TIMs showed the potential to improve the performance of heat exchanger regarding pressure drop and heat transfer.

# 7. FUTURE WORK

This research focused on the function of deformable walls on the microchannel heat exchanger. However, the relationship between the deformable walls, fluid flows, and the performance of the micro heat exchanger is not clearly given according to the dimensions of the micro heat exchanger (e.g., Elastic modulus and Poisson's ratio of the deformable walls, fluid characteristics, hydraulic diameter and the length of the micro heat exchanger). Therefore, future work is needed to expand our understanding of the relationship between the deformable walls and the fluid flows for potential applications of deformable coatings such as high-tech micro fluidic devices. Also, future work should be continued to determine whether employing TIMs coatings to a micro heat exchanger is cost effective. If not, it is worth investigating the turning point that the deformable walls can create a profit, and the properties of deformable walls at that point. Following lists include the potential future work that needs to be conducted:

• This paper assumes TIMs as a linear elastic material. Therefore, yield strength should be discussed in the case of the non-reversible deformation. Also, further investigation of the relationship between the Elastic modulus, Poisson's ratio, and the performance of deformable walls should be conducted to give a clear view of the function of deformable walls.

• Since the transition from laminar to turbulent occurs around $Re \approx 600$ in microchannels, which is relatively smaller than the conventional channels, a response of deformable walls should be examined in the condition of turbulent flow.

• Study of deformable walls to various inlet flow (e.g., pulsed flow) is needed for better understanding of deformable coating.

• A quantitative approach for heat transfer enhancement with deformable coatings regarding convective and conductive heat transfer is needed.

• The relationship between the deformable wall (Elastic modulus of the wall) and the fluid flow should be investigated to determine the optimal geometric design of deformable coating.

• Detailed experimental design for incorporating deformable coatings to microchannel heat exchanger should be discussed to determine its industrial application.

# REFERENCES


Bier, W., Keller, W., Linder, G., D, S., Schubert, K., & Martin, H. (1993). Gas to Gas Heat Transfer in Micro Heat Exchangers. *Chemical Engineering and Processing, 32*, 33-43.

Bier, W., Keller, W., Linder, G., Seidel, D., & Schubert, K. (1990). Manufacturing and Testing of Compact Micro Heat-Exchanger with High Volumetric Heat Transfer Coefficients. *Microstructure, Sensor and Actuators, ASME, DSC-19*, 189-197.

Champagne, P. R., & Bergles, A. E. (2001). Development and Testing of a Novel, Variable-Roughness Technique to Enhance, On Demand, Heat Transfer in a Single-Phase Heat Exchanger. *8*(5), 341-352. doi:10.1615/JEnhHeatTransf.v8.i5.50

Dini, J. W., & Snyder, D. D. (2010). *Electrodeposition of Copper, in Modern Electroplating* (M. Schlesinger & M. Paunovic Eds. Fifth ed.). Hoboken, NJ, USA: John Wiley & Sons, Inc.

E.W. Lemmon, M. O. M. a. D. G. F., "Thermophysical Properties of Fluid Systems" in NIST Chemistry WebBook, NIST Standard Reference Database Number 69, Eds. P.J. Linstrom and W.G. Mallard, National Institute of Standards and Technology, Gaithersburg MD, 20899, doi:10.18434/T4D303, (retrieved June 8, 2017).

Elabbasi, N., & Segui, J. (2014). Fluid-Structure Interaction Using COMSOL Multiphysics: Veryst Engineering, COMSOL Multiphysics.

Fan, Y., & Luo, L. (2008). Recent Applications of Advances in Microchannel Heat Exchangers and Multi-Scale Design Optimization. *Heat Transfer Engineering, 29:5*, 461-474. doi:10.1080/01457630701850968

Gui, F., & Scaringe, R. P. (1995). *Enhanced heat transfer in the entrance region of microchannels*: American Society of Mechanical Engineers, New York, NY (United States).

Hirt, C. W., Amsden, A. A., & Cook, J. L. (1974). An arbitrary Lagrangian-Eulerian computing method for all flow speeds. *Journal of Computational Physics, 14*(3), 227-253. doi:http://dx.doi.org/10.1016/0021-9991(74)90051-5

Jiang, P.-X., Fan, M.-H., Si, G.-S., & Ren, Z.-P. (2001). Thermal–hydraulic performance of small scale micro-channel and porous-media heat-exchangers. *International*

*Journal of Heat and Mass Transfer, 44*(5), 1039-1051. doi:http://dx.doi.org/10.1016/S0017-9310(00)00169-1

Kandlikar, S. G., Joshi, S., & Tian, S. (2003). Effect of Surface Roughness on Heat Transfer and Fluid Flow Characteristics at Low Reynolds Numbers in Small Diameter Tubes. *Heat Transfer Engineering, 24*(3), 4-16. doi:10.1080/01457630304069

Lewinsohn, C. (2015). High-efficiency, ceramic microchannel heat exchangers. *American Ceramic Society Bulletin, 94, No. 5*.

Mehendale, S. S., Jacobi, A. M., & Shah, R. K. (2000). Fluid flow and heat transfer at micro- and meso-scales with application to heat exchanger design. *Applied Mechanics Reviews, 53(7),* 175-193.

Morini, G. L. (2004). Single-phase convective heat transfer in microchannels: a review of experimental results. *International Journal of Thermal Sciences, 43*(7), 631-651. doi:10.1016/j.ijthermalsci.2004.01.003

Ploof, L. (2008). Electroless nickel composite coatings. *Adv. Mater. Process, 166*, 36-38.

Prasher, R. (2006). Thermal Interface Materials: Historical Perspective, Status, and Future Directions. *Proceedings of the IEEE, 94*(8), 1571-1586. doi:10.1109/jproc.2006.879796

Prasher, R. S. (2001). Surface Chemistry and Characteristics Based Model for the Thermal Contact Resistance of Fluidic Interstitial Thermal Interface Materials. *Journal of Heat Transfer, 123*(5), 969-975. doi:10.1115/1.1388301

Prasher, R. S., Shipley, J., Prstic, S., Koning, P., & Wang, J.-l. (2003). Thermal Resistance of Particle Laden Polymeric Thermal Interface Materials. *Journal of Heat Transfer, 125*(6), 1170-1177. doi:10.1115/1.1621893

Shah, R. K. (1991). Compact Heat Exchanger Technology and Applications, in Heat Exchanger Engineering, Volume 2: Compact Heat Exchangers: Techniques of Size Reduction, eds. E. A. Foumeny and P. J. Heggs. (Ellis Horwood Limited, London), 1-23.

Steinke, M. E., & Kandlikar, S. G. (2004). Single-Phase Heat Transfer Enhancement Techniques in Microchannel and Minichannel Flows. (41642), 141-148. doi:10.1115/ICMM2004-2328

Sturgis, J. C., & Mudawar, I. (1999). Single-phase heat transfer enhancement in a curved, rectangular channel subjected to concave heating. *International Journal of Heat and Mass Transfer, 42*(7), 1255-1272. doi:http://dx.doi.org/10.1016/S0017-9310(98)00232-4

Tao, W. Q., He, Y. L., Wang, Q. W., Qu, Z. G., & Song, F. Q. (2002). A unified analysis on enhancing single phase convective heat transfer with field synergy principle. *International Journal of Heat and Mass Transfer, 45*(24), 4871-4879. doi:http://dx.doi.org/10.1016/S0017-9310(02)00173-4

Yang, C.-Y., Yeh, C.-T., Liu, W.-C., & Yang, B.-C. (2007). Advanced Micro-Heat Exchangers for High Heat Flux. *Heat Transfer Engineering, 28*(8-9), 788-794. doi:10.1080/01457630701328676

Yegin, C., Nagabandi, N., Feng, X., King, C., Catalano, M., Oh, J. K., . . . Akbulut, M. (2017). Metal–Organic–Inorganic Nanocomposite Thermal Interface Materials with Ultralow Thermal Resistances. *ACS Applied Materials & Interfaces, 9*(11), 10120-10127. doi:10.1021/acsami.7b00093

Supplemental Sources

James R. Welty, Charles E. Wicks, Robert E. Wilson, Gregory L. Rorrer. (2008). *Fundamentals of Momentum, Heat, and Mass Transfer*. John Wiley & Sons, Inc. *Fifth Edition*

J.M. Smith, H. C. Van Ness, M. M. Abbott. (2005). *Introduction to Chemical Engineering Thermodynamics*. Mcgraw-Hill international edition. *Seventh Edition*

Noel de Nevers. (2005). *Fluid Mechanics for Chemical Engineers*. Mcgrawhill international edition. *Third Edition*

R. Byron Bird, Warren E. Stewart, Edwin N. Lightfoot. (2007). *Transport Phenomena*. John Wiley & Sons, Inc. *Revised Second Edition*